Aristotle University of Thessaloniki
School of Geology
Department of Geophysics

Study of the effect of temperature changes to the inversion results of electrical resistivity tomography data.

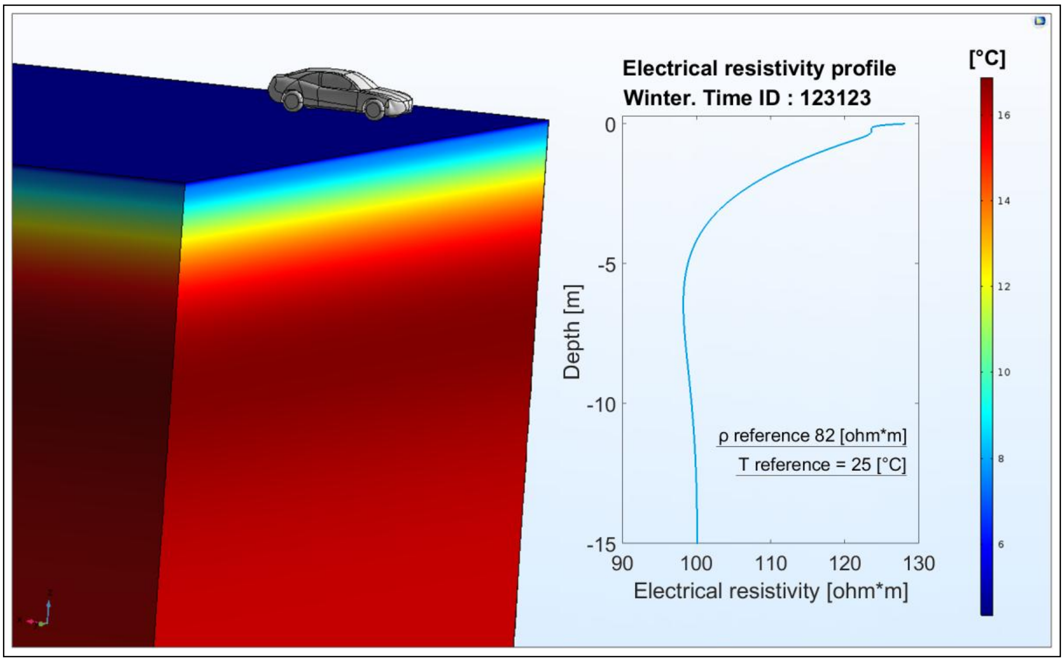

Polydoropoulos D. Konstantinos

Master Thesis

Postgraduate Program of the School of Geology in
"Applied and Environmental Geology"
Specialization: Applied Geophysics

April 2019

POLYDOROPOULOS KONSTANTINOS

GEOLOGIST

Study of the effect of temperature changes to the inversion results of electrical resistivity tomography data.

Submitted to the School of Geology of Aristotle University of Thessaloniki within the postgraduate program “Applied and Environmental Geology” in specialization “Applied Geophysics”

Advisory Committee

Professor Panagiotis Tsourlos (Supervisor)

Associate Professor George Vargemezis (Advisory Committee member)

Professor Gregory Tsokas (Advisory Committee member)

Study of the effect of temperature changes to the inversion results of electrical resistivity tomography data.

Contents

Abstract

The electrical resistivity tomography (ERT) and the relationship between electrical resistivity and temperature are widely used in applications such as the detection of the subsurface temperature anomalies and the conversion of temperature effected subsurface geoelectrical properties to a reference temperature. In the present study, the conversion of the inverted ERT sections to a reference temperature is investigated. We study the case of the influence of the diurnal and seasonal temperature oscillations on the ground to the subsurface earth resistivities. We adopt a conversion ("correction") method for the surface temperature effect which is relied on a) the calculation of the subsurface temperature profile and b) on applying empirical electrical resistivity-temperature conversion models to correct the inverted resistivities. To study the phenomenon and to validate the correction approach we performed extensive synthetic data tests using temperature "contaminated" geoelectrical models which are assumed to have either homogeneous or inhomogeneous thermal properties. The synthetic "contaminated" geoelectrical data were inverted using standard processing tools and the results were subjected to temperature correction i.e. conversion to a reference temperature using the scheme developed in this work. The synthetic data tests calculated using typical Mediterranean temperature oscillations and typical thermal properties suggest that the diurnal oscillation effects the resistivities significantly (i.e. >3% change) up to a depth of 0.3m below the ground while the seasonal (annual) oscillation is significant up to a depth of approximately 10m. Note that these depths vary with different climate conditions and thermal properties. In the ERT measurement context the inversion results produced by ERT data-sets collected with inter-electrode sapcing of 7m or less, need to be considered for seasonal temperature effect if of course this is necessary for the study of the geoelectrical property variations (i.e. time-lapse ERT studies). Respectively data produced by arrays with spacing less than 1m need to considered for the correction of the diurnal temperature effect. In order to correct the seasonal oscillating resistivity horizons, we should utilize correction temperature profile which takes into account both the annual and the diurnal oscillation events. The correction approach we adopted assumes thermally homogeneous media. It performed well in all tested cases since it produced improved results even for thermally inhomogeneous synthetic models.

Περίληψη

Οι ηλεκτρικές τομογραφίες (ERT) και η σχέση μεταξύ της ηλεκτρικής αντίστασης και της θερμοκρασίας χρησιμοποιούνται ευρέως σε εφαρμογές όπως ο εντοπισμός των θερμοκρασιών ανωμαλιών του υποβάθρου και η αναγωγή των θερμοκρασιακά επηρεασμένων ηλεκτρικών ιδιοτήτων του υπεδάφους σε μια θερμοκρασία αναφοράς. Στην παρούσα μελέτη, ερευνάται η αναγωγή των αποτελεσμάτων της αντιστροφής δεδομένων ηλεκτρικής τομογραφίας σε μια θερμοκρασία αναφοράς. Μελετήθηκε η περίπτωση της επίδρασης της ημερήσιας και της εποχικής μεταβολής της θερμοκρασίας της επιφάνειας του εδάφους στις ηλεκτρικές αντιστάσεις των σχηματισμών του υπεδάφους. Επίσης υιοθετήθηκε μια μέθοδος αναγωγής (διόρθωσης) των αποτελεσμάτων της αντιστροφής των ηλεκτρικών τομογραφιών, που έχουν επηρεαστεί από την επιφανειακή μεταβολή της θερμοκρασίας, η οποία βασίζεται: α) στον υπολογισμό του θερμοκρασιακού προφίλ των υπεδάφειων σχηματισμών και β) στην εφαρμογή εμπειρικών σχέσεων αναγωγής της ηλεκτρικής αντίστασης και της θερμοκρασίας. Για την αξιολόγηση του φαινομένου και της μεθοδολογίας της διόρθωσης, πραγματοποιήθηκαν εκτεταμένες δοκιμές με συνθετικά δεδομένα, χρησιμοποιώντας θερμοκρασιακά επηρεασμένα ηλεκτρικά μοντέλα τα οποία έχουν είτε ομογενής είτε ανομοιογενείς θερμικές ιδιότητες. Τα συνθετικά γεωηλεκτρικά δεδομένα υπέστησαν αντιστροφή χρησιμοποιώντας τυποποιημένα εργαλεία επεξεργασίας και κατόπιν υποβλήθηκαν σε διόρθωση θερμοκρασίας δηλαδή αναγωγή της ηλεκτρικής αντίστασης σε θερμοκρασία αναφοράς χρησιμοποιώντας ένα λογισμικό που αναπτύχθηκε σε αυτή την εργασία. Οι δοκιμές με τα συνθετικά δεδομένα που θεωρήθηκε ότι επηρεάστηκαν από μια τυπική (μεσογειακής) θερμοκρασιακή μεταβολή για μέσα με τυπικές θερμικές ιδιότητες, φανερώνουν ότι η ημερήσια μεταβολή επηρεάζει ισχυρά της αντιστάσεις (π.χ μεταβολή >3%) μέχρι το βάθος των 0.3m από την επιφάνεια του εδάφους, ενώ η αντίστοιχη εποχική (ετήσια) μεταβολή επιδρά ισχυρά μέχρι περίπου τα 10m βάθος. Σημειώνεται ότι αυτά τα βάθη ποικίλλουν ανάλογα με τις διαφορετικές κλιματικές συνθήκες και τις ποικίλες θερμικές ιδιότητες των σχηματισμών του υπεδάφους. Στο πλαίσιο των μετρήσεων ηλεκτρικής τομογραφίας η επίδραση της εποχιακής μεταβολής της θερμοκρασίας θα πρέπει να λαμβάνεται υπόψη σε αποτελέσματα αντιστροφής που προέρχονται από διατάξεις ηλεκτροδίων όπου τα ηλεκτρόδια απέχουν μεταξύ τους τουλάχιστο 7m ή λιγότερο, στις περιπτώσεις βέβαια που ενδιαφερόμαστε για τη μελέτη της

διαχρονικής μεταβολής της αντίστασης . Αντίστοιχα, η διόρθωση της ημερήσιας θερμοκρασιακής μεταβολής χρειάζεται να ληφθεί υπόψη σε δεδομένα που παράγονται από διατάξεις ηλεκτροδίων με απόσταση μικρότερη από 1m. Για τη διόρθωση των εποχικά μεταβαλλόμενων αντιστάσεων χρειάζεται να χρησιμοποιηθούν θερμοκρασιακά προφίλ διόρθωσης που λαμβάνουν υπόψη τόσο την ετήσια όσο και την ημερήσια μεταβολή. Η προσέγγιση διόρθωσης που υιοθετήθηκε στην παρούσα εργασία προϋποθέτει θερμικά ομογενείς σχηματισμούς και έχει ικανοποιητική επίδοση σε όλες τις δοκιμές που εκτελέσαμε, καθώς παρήγαγε βελτιωμένα αποτελέσματα ακόμη και στις περιπτώσεις συνθετικών μοντέλων με μεγάλο βαθμό θερμικής ανομοιογένειας.

Acknowledgements

I would like firstly to express my gratitude to my supervisor Professor Panagiotis Tsourlos for the thesis assignment and for being always by my side in this long journey, answering my questions, guiding and support me. Also I would like to thank Associate Professor George Vargemezis and Professor Gregory Tsokas which offered me their support, knowledge and inspiration as well as field experience. I would like to thank Dr. Sum Gyu Park for the conversations and his company at the breaks, too. I need to acknowledge the valuable help of Marios Karaoulis during the first steps especially for introducing me into COMSOL. Also I would like to thank Professsor Evangelia Tsoukala and Professor Nikolao Fragki for their valuable conversations and their help. After completing the postgraduate course, I feel very lucky for having the chance to be a student in the Departmnet of Geophysics of AUTH and for enjoying the support that it provides to their students.

My fellow master students Dimitris Angelis, Nikos Chatzis, Ioannis Grendas, Dimitris Oikonomou and Aris Nivorlis are praiseworthy and I would like to thank them for the nice cooperation we had during our Master's course.

Last but not least, I would like to thank my family for the support and love over all these years of my studies and I would like to dedicate this work to them.

1. Introduction

Temperature, as an intrinsic property that describes partially the internal energy of matter, coexists in equilibrium with the other physical properties. Change in temperature will lead to changes in the other physical properties and particularly in electrical resistivity, which is also an intrinsic property.

Geophysical techniques like electrical resistivity tomography (ERT), image the subsurface electrical resistivity at depths that are effected by temperature changes either due to the earth's interior processes or due to atmospheric processes, and as a result, the produced subsurface geoelectrical structure is influenced by the temperature effect.

The temperature effect imposed to the electrical resistivity of the formations, can be either enlightening for the interpretation process, as it happens in cases of geothermal fields, or can be misleading in cases related to geoelectrical monitoring of various processes. Extensive research has been conducted aiming to the definition of the relationship between the electrical resistivity and the temperature (Allison et al. 1954, Keller and Frischknecht 1966, Sheets & Hendrickx 1995, Rhoades et al. 1999, Besson et al. 2008, Corwin & Lesch 2005, Hayley et al. 2007, Ma et al. 2011). These works provided conversion functions that correlate the temperature and the electrical conductivity and thus allowed the characterization or the removal of temperature effect from the produced electrical resistivity of the subsurface formations.

A wide range of applications, ranging from geothermal fields to permafrost terrains and near subsurface investigations, use temperature - electrical resistivity conversion functions to support the interpretation process.

From an energy point of view, deep and shallow geothermal systems are used widely in order to substitute the energy obtained from other costly and non eco-friendly energy sources. For this purpose, experimental approaches have been conducted targeting the transition and tracing of heat with resistivity methods (Firmbach et al. 2013). Also, there are advanced techniques that use the electrical resistivity methods in order to monitor the temperature's changes in low enthalpy geothermal systems (Hermans et al. 2014) as well as in high enthalpy geothermal systems (Kummerow & Raab 2015a, 2015b).

From an environmental point of view, long period earth atmospheric temperature changes are imprinted on permafrost areas that act as a global sensitive thermometer. Lewis & Dethier (2013) and You et al. (2013) used geophysical techniques and temperature - resistivity correlations to track the presence and the evolution of permafrost through time and investigate the phenomenon of global warming and climate change.

From a geotechnical aspect, landslides, is a phenomenon that has disastrous consequences on the technical constructions and also threatens human life. Many researchers are studying landslides that take place close to the surface, in a thermal layer where temperatures shift over due to diurnal and seasonal temperature cycles reflecting the surface temperature oscillations (Krautblatter & Hauck (2007), Chambers 2009, Gance et al. 2016, Merrill, 2018).

In the same near subsurface thermal layer, where the surface temperature oscillation forms the resistivity profiles, the water content as well as the moisture content have been investigated for both geotechnical reasons (Brunet et al. 2010 , Chambers et al. 2014, Gunn et al. 2015) and agricultural purposes (Michot et al. 2003, Corwin & Lesch, 2005, Brillante et al. 2015). Cases of salt-affected soil (Hayley et al. 2009) as well as leaks in waste landfill covers (Genelle et al. 2012) has been implemented including the removal of temperature effect.

Focusing in the surface temperature effected thermal layer, from the literature review there are two basic methods in literature for the conversion of the surface temperature effected subsurface resistivities to a reference temperature. These two methods are, a direct method with in situ subsurface measurements of the subsurface temperature profile by inserting temperature sensors into the ground (Genelle et al., 2012) and an indirect method (Brunet et al., 2010; Chambers et al. ,2014; Gunn et al., 2015; Merritt et al. 2018) that calculates the subsurface temperature profile indirectly by taking into account only the surface temperature reccords. Both methods use the subsurface temperature profile combined with a conversion model of “temperature and electrical resistivity” to correct the temperature effected resistivities of the inverted ERT model. Hayley et al., 2010, propose a different correction algorithm that apply a “temperature correction” to the measured apparent resistivity data of ERT with the use of the temperature profile and by applying forward geoelectrical modelling (Hayley et al 2010).

In the present thesis, the indirect method for the acquisition of the temperature profile and the correction of the temperature effected ERTs was studied. The study is based on the literature review as well as on forward and inverse models for a typical range of rock formation properties. Also, a surface temperature correction algorithm was developed for the temperature effected inversion results of the ERT method. The correction algorithm was designed for the entire range of the temperature effected depths of a homogeneous formation, where no mass movement or phase change take place, and was evaluated on homogeneous and inhomogeneous forward models.

The methodology followed for this approach has the following steps:

1. Literature review of the temperature and electrical resistivity conversion models. Evaluation of these models and selection of the one that best fit the needs of this study. Review on the analytical solutions of the diffusion differential equation.
2. Algorithmic development that imports the surface temperature effect into the forward electrical resistivity models.
3. Evaluation of the ERT efficiency to detect the surface temperature effect in time and depth, based on the temperature effected forward models.
4. Algorithmic development for the correction of the surface temperature effect ERTs.
5. Application of the correction method on a set of forward models.

Thesis structure

The basic principles of this thesis are presented in chapter 2. Firstly, the surface and subsurface environment where the temperature effect take place due to surface temperature variations, is presented. Secondly, the heat transfer mechanism that provides the temperature profile of near subsurface and is used for the effect and the correction of the models, is described. Thirdly, the conversion models of temperature and electrical resistivity that are presented in literature, are presented and commented. Finally, the electrical resistivity tomography (ERT) method for which the temperature correction algorithm was created, is presented.

In chapter 3, the methodology for the correction of temperature effected ERTs is described. To start with, the heat and electrical properties that determine the under correction formation are discussed. Afterwards, the acquisition of the surface temperature properties and the calculation of the subsurface temperature profiles, are described. Then, the use of the calculated temperature profile, combined with an electrical resistivity - temperature conversion model, for the correction of the temperature effect, is presented. Finally the logistics for the correction, applied on a graphical user interface created for the correction of surface temperature effected ERTs, are presented.

In chapter 4 the methodology followed for the validation of the correction approach with the use of forward and inverse homogenous and inhomogeneous models, is provided. The results of the validation process are shown in chapter 5. Initially, the temperature and resistivity range in space and time for some typical rock formations, is established. Then the calculated resistivity ranges, that set the range of the applicable arrays and resolutions for the ERT method which can be corrected, are presented. Then the correction method is validated up to the diurnal and the annual perturbation depths using forward and inverse models. Finally in chapter 6 the conclusions are summarized in chapter 0.

2. Basic principles

In this chapter, the temperature changes on the surface of the earth, due to a Mediterranean climate, and its impact to the subsurface, are described. For this purpose, the transition of heat into the soil and its relationship with the electrical resistivity, are featured. Also, the methodology of the electrical resistivity tomography (ERT) is explained, as it will be used for the application of the temperature correction and the conversion of the temperature effected electrical resistivity tomographies to a reference temperature (25 °C for this study*).*

2.1 Surface and subsurface environment

Starting from the surface temperature conditions of earth, the temperature is oscillating due to earth's orbital movement and varies due to atmospheric processes like wind and cloud cover, as well as other factors like altitude, longitude and vegetation canopy. In order to model the temperature profile inside the subsurface, the surface temperature oscillation history of an annual cycle is needed. A simplified method, for the expression of the complex temperature variations that can be recorded over an annual cycle, is implemented with the use of the mean annual surface temperature and the amplitudes of the temperature oscillations during the annual cycle (Hillel 2004). Equation (2-1) represents the simplified form where only the mean seasonal amplitude is used. gsfsagagafdsa

$$T(0,t) = T_m + T_{msa} * \sin(\omega_a * t + \varphi_a) \qquad (2\text{-}1)$$

Where

$T(t,0)$ is the temperature at the selected time of the year on the surface

t is the selected time of the year

T_m is the mean annual temperature

T_{msa} is the mean amplitude of seasonal (annual) temperature oscillation

ω_a is the annual radial frequency

φ_a is the phase change of annual temperature oscillation

The temperature effect caused by the surface temperature oscillation, takes place at the near-subsurface layer, where the solid parts of the formations can be either solid rock or soil. A classification of soil subsurface layers, according to Hillel (2004), starts with the regolith, which is the part of the earth's subsurface that is overlying the consolidated bedrock and consists of a set of parallel horizons called O,A,B,C. The graph in Figure 2-1 shows a conceptual representation of these horizons. The main constituents that can be found in these layers are the solid phase (including organic matter), liquid phase like water solutions and gaseous phase like atmospheric air.

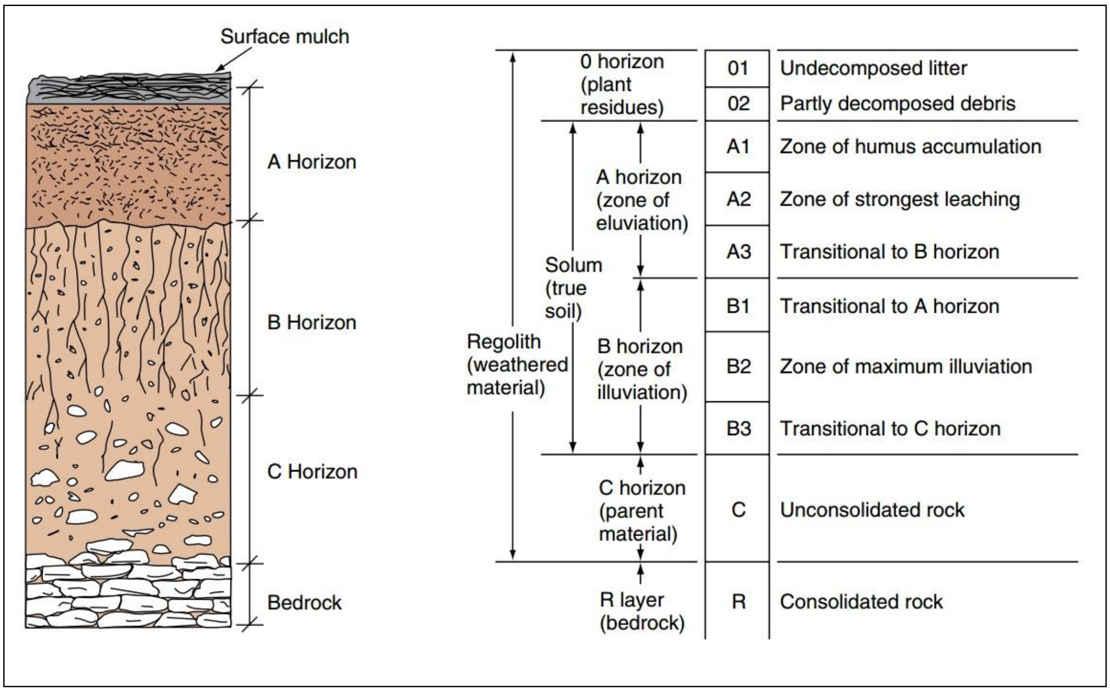

Figure 2-1 Soil Horizons (figure from Hillel (2004) Figures 1.1, 1.2, p. 9).

"O" horizon consists of organic residues while "A" is the horizon where minerals and organic matter coexist and the main biological activity occurs. "O" and "A" horizons are considered to be the topsoil layer. The boundary of top soil with "B" horizon, where the subsoil starts, is found at depths close to 0.4 m for pedologists. Bayowa & Olayiwola (2015) categorized topsoil based on corrosivity and competence related to vertical electrical resistivity measurements within an area of 0.4 km^2 , and correlated top soil thickness with a range of 0.2 and 2 m depth. In this study the top soil thickness is determined by the perturbation depth of the diurnal surface temperature oscillation that reaches depths close to 0.3 m .

The intermediate places of solid constituents across the vertical axis of the stratigraphic tomography, is filled with air and water, where the variation of the amount of water with the depth, separates 2 zones, the vadose/dry and the saturated zone (Figure 2-2.) The vadose zone extends from the surface of earth to the depth of the regional groundwater table where the saturated zone stars. Vadose zone also includes the transient zone, where capillary forces occur. The thickness of the vadose zone may be less than 1 m or can extend to hundreds of meters or more, depending on the depth of the water table (Holden & Fierer, 2003)

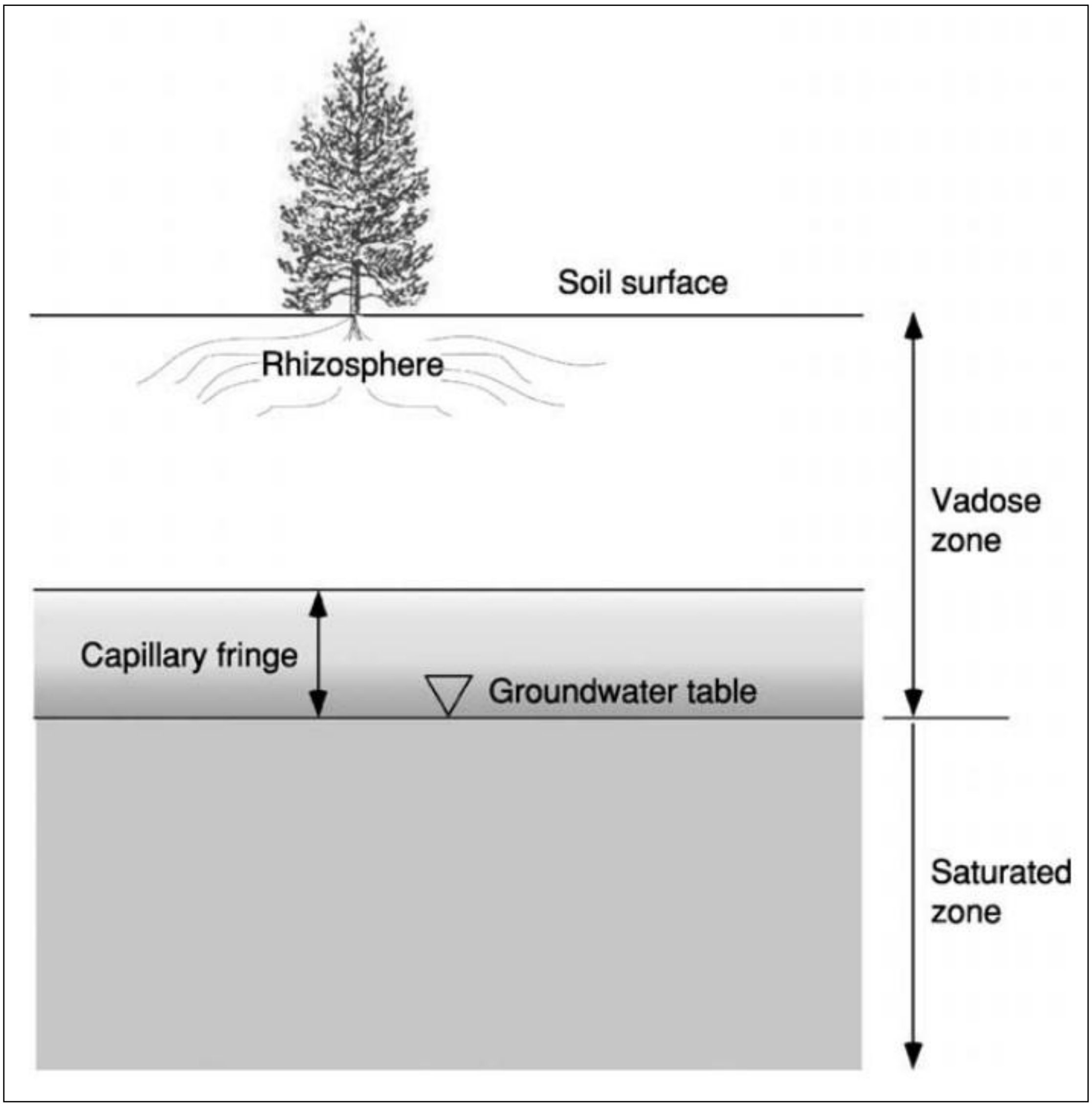

Figure 2-2 Subsurface zones divided by their water content
(figure from Holden & Fierer, (2003) Figures 1, p. 217).

2.2 Energy, temperature and heat transfer

In physics, energy with SI unit joules designated as "j", is a property of the matter that can be transferred between objects, and converted into a variety of forms like potential and kinetic energy. The internal energy of a system is determined inter alia by the internal potential and the internal kinetic energy of atoms and molecules in the microscopic scale, excluding the macroscopic kinetic and the potential energy of the system as a whole due to external force fields.

The internal kinetic energy possessed by atoms and molecules is in the form of translational, rotational, and vibrational motions. The temperature is a measure of the average translational kinetic energy of atoms and molecules in a system. The change of mercury volume inside a thermometer and the changes of the electric resistivity of soil, are examples where change of internal energy becomes measurable.

In thermodynamics, which is the science of the flow of heat, heat transfer is the process of energy transition from a high temperature object to a lower temperature object. There are three modes of heat transfer, the conduction, the convection and the radiation.

- **Conduction** is the mode of energy transfer, where the internal kinetic energy, possessed by atoms and molecules, is transferred to neighbour particles by means of collisions between them and exchange of kinetic energy.
- **Convection** is the mode of energy transfer, where the energy is carried by particles (fluids) inside an isolated system, so as the system achieves energy equilibrium across its boundaries. Besides natural convection, forced convection takes place in cases of heat pumps.
- **Radiation** is the mode of energy transfer, where the energy with the form of electromagnetic waves is emitted by bodies with temperatures higher than $0\ k$, absorbed by other bodies, which as a result of the absorption increases their temperature.

Conduction is the only mechanism that is considered in this work, as the heat transfer at the study area occurs primarily by conduction and only secondary by radiation and convection (Robertson 1988, Martin 2004). Thermal diffusivity “D” with SI unit m^2/s is the only heat variable needed for this approach. Nevertheless, heat capacity and thermal conductivity, that are commonly used properties related to the thermal diffusivity, will be also presented below.

Heat Capacity

Heat capacity is a property that describes the ability of a material to store energy in the form of internal energy, without phase change. Adding heat in a closed system, results into the raise of the internal energy of the system, which is measured by the change of its temperature. For the same amount of heat energy added into two closed systems with the same initial temperature but different heat capacities, the system with higher heat capacity (e.x. water) will present a smaller temperature raise than the system with lower heat capacity (e.x. minerals).

There are two derived quantities that specify the heat capacity as an **intensive (or intrinsic) property** of a substance (despite the size of the sample). These are:

- **Molar heat capacity C** (heat capacity per unit mol)
  is the heat capacity per **mole** of a pure substance. Molar heat capacity is often designated as **CP**, to denote heat capacity under constant pressure conditions, as well as **CV**, to denote heat capacity under constant volume conditions. Unit of molar heat capacity is J/(K * mol)

- **Specific heat capacity c** (heat capacity per unit mass)
  often simply called specific heat, is the heat capacity per unit **mass** of a pure substance. This is designated as **cP** (constant pressure conditions) and as **cV** (constant volume conditions). Unit of specific heat capacity is J/(K * Kg) .

Heat Capacity, as an **extensive (or extrinsic) property** that depends on the size of the sample, is called volumetric heat capacity.

- **Volumetric heat capacity VHC** (heat capacity per unit volume)
  is the heat required to raise the temperature of a volume unit by 1°C. Volumetric heat capacity VHC is equal to the product of specific heat capacity **cP** and density $\boldsymbol{\rho_d}$ Kg/m^3 of the unit volume sample. Subscript $_d$ of density is used to distinguish the density $\boldsymbol{\rho_d}$ from the electrical resistance $\boldsymbol{\rho}$. Unit of VHC is $J/(K * m^3)$.

$$VHC = cP * \rho_d \tag{2-2}$$

A soil consists of solid, liquid and gas phases and their properties (Table 2-1) are used to set a bulk value of heat capacity. For a homogeneous material, like soil that consists of a number of different components, the total VHC can be calculated by the sum of products of each VHC with its volume fraction f (de Vries 1975a), equation (2-3).

$$VHC_{total} = \sum(f_s * VHC_s + f_l * VHC_l + f_g * VHC_g) \qquad (2\text{-}3)$$

The subscript “s” denotes solid phase, “l” denotes liquid phase and “g” denotes gas phase.

Constituent	Density ρ (kg/m³)	Heat capacity C (J/m³ K)
Quartz	2.66×10^3	2.0×10^6
Other minerals (average)	2.65×10^3	2.0×10^6
Organic matter	1.3×10^3	2.5×10^6
Water (liquid)	1.0×10^3	4.2×10^6
Ice	0.92×10^3	1.9×10^6
Air	1.25	1.25×10^3

Table 2-1 Densities and volumetric heat capacities of soil constituents (at 10 °C) and of Ice (at 0 °C) (table modified from Hillel (2004) table 12.1, p. 220).

Thermal conductivity

Thermal conductivity “k” refers to the efficiency of the matter to conduct heat and defines the amount of the internal energy that will be transferred in a unit time, through a unit distance of substance under a unit temperature difference, with SI unit watts per meter Kelvin W/(K*m) . Similar methods to De Vries, D. A. (1975a) and Tian et al (2016) determine soil’s thermal conductivity as a bulk property derived from the properties of different types and phases that coexist in the formation, while other approaches, like the curve fitting schemes between electrical and thermal conductivity, have been also proposed (Wang et al. 2017a). Table 2-2 depicts the thermal conductivity of different constituents and phases.

Constituent	mcal/cm sec K	(W/m K)
Quartz	21	8.8
Other minerals (average)	7	2.9
Organic matter	0.6	0.25
Water (liquid)	1.37	0.57
Ice	5.2	2.2
Air	0.06	0.025

Table 2-2 Thermal Conductivity of Soil Constituents (at 10°C) and of Ice (at 0°C) (table from Hillel (2004), table 12.2, p. 222).

Thermal Diffusivity

Thermal diffusivity D, is the ratio of thermal conductivity k, and the heat capacity per unit volume VHC. Thermal diffusivity determines the temperature response of a soil to thermal perturbations (Martin, 2004). SI unit of thermal diffusivity is m^2/s .

$$D = \frac{k}{\rho_d * cP} = \frac{k}{VHC} \tag{2-4}$$

Heat transfer

Fourier's law for heat conduction states that whenever a temperature gradient exists in a medium, instantaneously a heat J flow is established. In one dimension form (soil's depth dimension z m) and for a homogeneous and isotropic material, the heat flux density "q_h" that is the rate of heat transfer per unit area with SI unit W/m^2 , and is expressed with eq. (2-5), where k is thermal conductivity and T is the temperature.

$$q_h = -k * \frac{\partial T}{\partial z} \tag{2-5}$$

Aiming to the formation of an expression that will describe the temperature variation in one homogeneous spatial dimension during an annual cycle, due to heat transition caused by the surface temperature oscillations, the diffusion equation is used eq. (2-6), where "cP" is the heat capacity per unit mass and "ρ_d" is mass density. Q represents any external energy sources or sinks with SI unit W/m^3 .

$$cP(z) * \rho_d(z) * \frac{\partial T}{\partial t} = -\frac{\partial q_h}{\partial z} + Q(z,t) \tag{2-6}$$

In the absence of any sink or source of heat and assuming that the bulk heat properties of the formation are constant, the combination of (2-5) and (2-6) forms the linear homogeneous parabolic partial differential equation, that solves the time depended heat distribution in one spacial dimension.

$$\frac{\partial T}{\partial t} = D * \frac{\partial^2 T}{\partial z^2} \tag{2-7}$$

The exact analytical solution of equation (2-7) with

Initial condition $T\ (z,0) = T_m$

Boundary conditions $T\ (0,t) = T_m + T_{maa} * \sin(\omega_a * t + \varphi_a)$

$$\lim_{L \to +\infty} T\ (L,t) = Tm$$

where:

$T(t,0)$	is the temperature at the selected time of the year on the surface
t	is the selected time of the year
T_m	is the mean temperature of the year
T_{msa}	is the mean amplitude of seasonal temperature oscillation
ω_a	is the annual radial frequency
φ_a	is the phase change of annual temperature oscillation
L	is the maximum depth

is forming to eq. (2-8) (Hillel 2004, Fu & Leventhal, 2011).

$$T(z,t) = T_m + \frac{T_{maa}}{e^{\left(\frac{z}{d_a}\right)}} * \left[\sin\left(\omega_a * t + \varphi_a - \frac{z}{d_a}\right)\right] \tag{2-8}$$

Where

z	is the selected depth ($z \geq 0$)
d_a	is the damping depth of annual temperature oscillation

Damping depth d_a describes the depth where the temperature is equal to the 1/e (1/2.718=0.37) of the seasonal amplitude of surface temperature oscillation. SI unit of damping depth is m. Calculation of damping depth uses thermal diffusivity and the angular frequency of surface temperature oscillation eq. (2-9).

$$d = \sqrt{\frac{2 * D}{\omega}} \qquad (2\text{-}9)$$

Equation (2-8), presents the solution result for a Dirichlet boundary condition that describes only the seasonal temperature oscillation. Using the term harmonics, in order to distinguish the multiple simultaneous events (seasonal temperature oscillation event, diurnal temperature oscillation event, etc.) that take place and shape the actual surface temperature oscillation, equation (2-8) can be rewritten and used as the sum of these harmonics (Kusuda & Achenbach 1965, Hillel, 2004).

2.3 Conversion models of electric resistivity and temperature

Thermal migration in the upper layers of the subsurface of the earth due to atmospheric temperature variations, is a time-dependent physical phenomenon that has an impact on the internal energy of subsurface materials. As a result, the electrical properties of underground formations are changing through time.

Electrical resistivity or specific electrical resistance "ρ" also denoted as "rho" is an intensive property of matter that quantifies the ability of a substance to set in motion its electric charges, under the application of an electric field. The SI unit of electrical resistivity is the ohm*meter, Ω*m (commonly used ohm-m). Inversed electric resistivity is the specific conductance or electric conductivity "σ" and has SI unit Siemens/meter S/m.

The influence of temperature °C on electrical resistivity ohm-m, both for a liquid and for a solid medium, is well established: "A temperature increase results in an electrical resistivity decrease" (Wells 1990, Besson et al. 2008). As far as solutions are concerned, small changes of temperature (no phase change), act on electrolytes of water, and affect the resistivity. An increase in temperature decreases the viscosity of the electrolyte and as a result the electric resistivity decreases (Papazaxos 1996).

The basic principle of a conversion model of temperature and electrical resistivity, is the conversion of the electrical resistivity "ρ_{Tref}" at a given reference temperature "T_{ref}", into a new value "ρ_{Tm}" measured at a temperature "T_m", based on a temperature conversion factor "f_T", according to equation (2-10), (Allison et al. 1954).

$$\frac{\rho_{Tm}}{\rho_{Tref}} = f\,(T) \qquad (2\text{-}10)$$

Ma, et al. (2011) evaluated the based on liquid fluid conversion models existing in the literature, comparing the residuals between conversion factors $f\,(T)$ of literature conversion models and the experimental conversion factors $f\,(T)$ of Allison et al. (1954), and classified them based on their mathematical expression into Ratio eq.(2-12), Exponential eq. (2-11), Polynomial eq. (2-13) and Power function model (2-14), (Table 2-3), and suggest that practitioners should use either the exponential model corrected and presented by Corwin & Lesch (2005) or the ratio model.

The ratio model has been tested and used by many researchers for different values of temperature coefficient of resistance δ (also used the "α" letter) and a wide range of reference temperatures. Keller and Frischknecht (1966) suggest as reference temperature 18 °C and δ = 0.025 °C . Ma et al. (2010) states that the ratio model, with reference temperature 25 °C and δ=0.0191, has trustworthy results about the temperature effect in the range between 3 and 47 °C.

The exponential model (the corrected Sheets & Hendrickx (1995) model by Corwin & Lesch (2005)) performs the best, and is designed for reference temperature at 25 °C and temperature effect range between 3 and 47 °C (Ma, et al. 2011).

Rhoades et al. (1999) model (Polynomial model), was also designed for reference temperature 25 °C only and temperature range between 15 and 35 °C.

Conversion models / Application temperature range	**References**	**Equations**	**Equations Number**
1) Exponential model 3 - 47 °C	Corrected Sheets & Hendrickx (1995) from Corwin & Lesch (2005)	$\frac{\rho_{Tm}}{\rho_{25}} = 0.4470 + 1.4034 * e^{-T_m/26.815}$	(2-11)
2) Ratio Model 3 - 47 °C	Keller and Frischknecht (1966)	$\frac{\rho_{Tm}}{\rho_{ref}} = \frac{1}{1+\delta(T_m - T_{ref})}$; $\delta = 0.0191\ or\ 0.025\ \,°\mathrm{C}^{-1}$	(2-12)
3) Polynomial model 15 - 35 °C	Rhoades et al. (1999)	$\frac{\rho_{Tm}}{\rho_{25}} = 1 \quad - 0.020346 * (T_m - 25)$ $+ 0.0003822 * (T_m - 25)^2$ $+ 0.00000555 * (T_m - 25)^3$	(2-13)
4) Power function model 5 - 20 °C	Besson et al. (2008)	$\frac{\rho_{Tm}}{\rho_{T_{ref}}} = \left(\frac{T_{ref}}{T_m}\right)^{0.3}$	(2-14)

Table 2-3 Literature's conversion models of electrical resistivity and temperature.

We used the proposed models to perform some test runs. Figure 2-3 shows the performance of liquid fluid based models for a range or temperatures between 3 and 47 °C, reference resistivities 100 ohm-m and reference temperature 25 °C. Ratio model is represented with δ values as 0.0191 and 0.025.

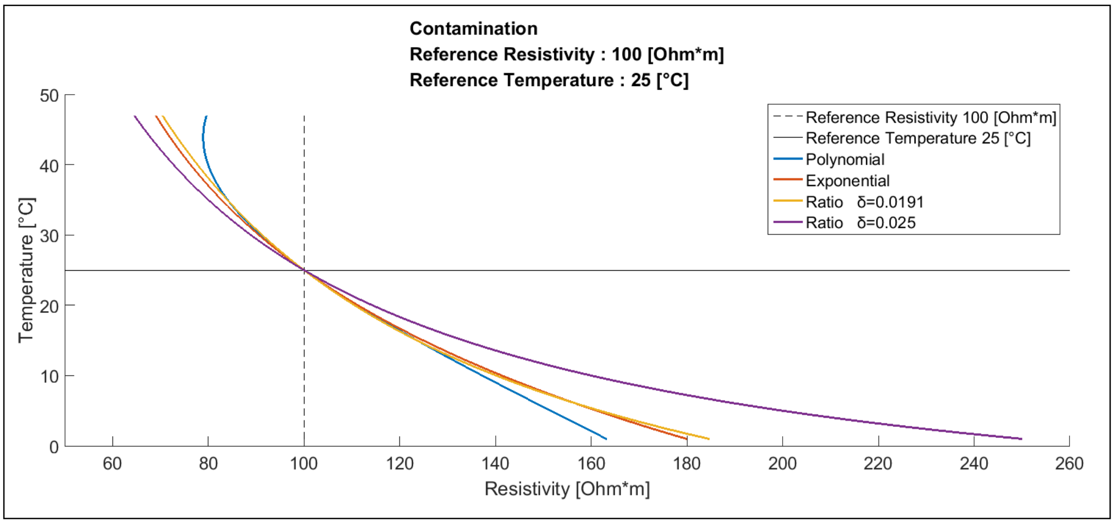

Figure 2-3 Empirical conversion models of electrical resistivity and temperature, applied on 100 ohm-m reference electrical resistivity at 25 °C reference temperature.

It is clear that the removal of water content from a porous formation reduces the heat capacity of the formation and as a result for the same heat addition, the resistivity amplitudes from the 25 °C reference resistivity value should be increased, as represented by the ratio model with δ=0.025 in Figure 2-3.

Considering a non saturated formation, Besson et al. (2008) suggest that the models based on solutions or soil solution extracts (Ratio, exponential and polynomial) are reliable for the correction, when the volumetric soil water content tends to saturation, and presents a power function model, determined by regression analysis on experimental data from undisturbed soil samples with various water and clay content.

This particular model was designed only for a range of temperatures between 5 and 20 °C. For this model, the reference temperature is also variable as it is in the ratio model. Comparing the ratio and the power function model for T_{ref} = 16 °C in a temperature effect range of 5 to 20 °C, Figure 2-4 shows better correlation when the ratio model has value δ = 0.025, which is a value usually used in the literature.

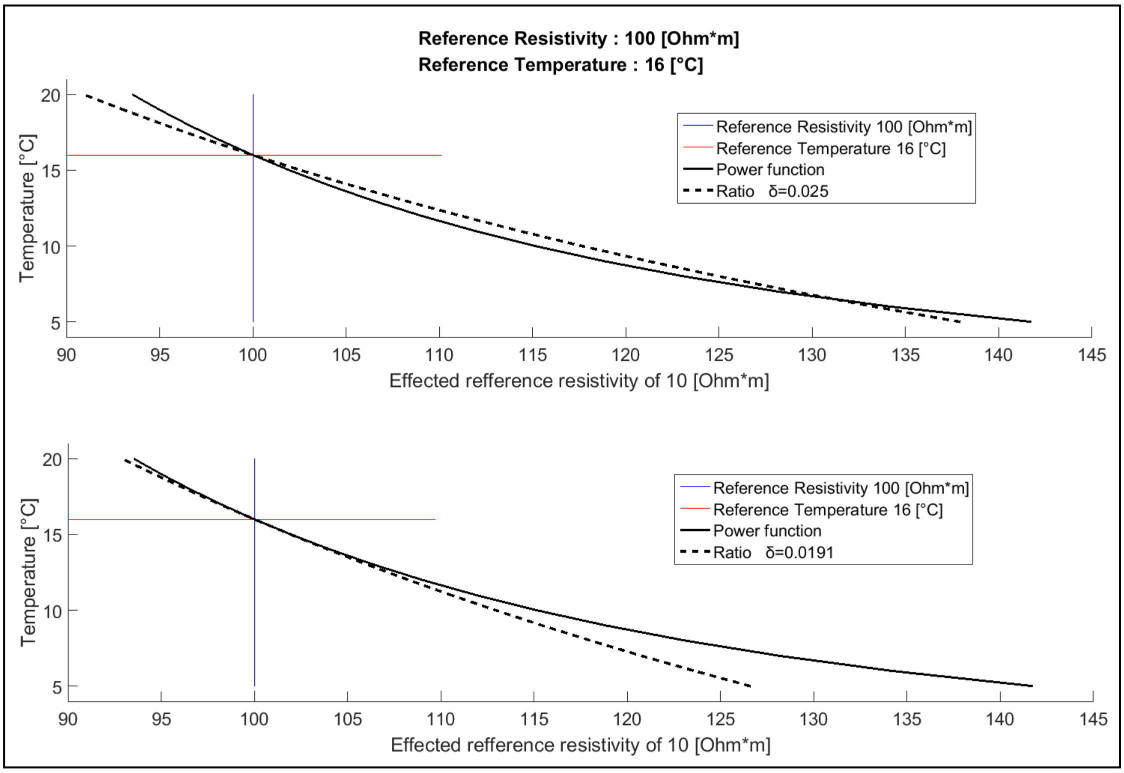

Figure 2-4 Power function conversion model (derived from unsaturated soil samples) in comparison with the two different values for the "temperature coefficient of resistance" of the ratio conversion model.

Concluding, in the case of water saturated formations, it is preferable to use the solution based conversion models that are 1) the exponential model and 2) the ratio model with temperature coefficient of resistance δ=0.0191. For non saturated porous formations the non fluid based models, either the Besson et al. 2008 or the Keller and Frischknecht. 1966 model (with temperature coefficient of resistance δ=0.025 $°C^{-1}$) perform well in the range of 5-25 °C, and should be tested for the rest of the temperature range of an annual surface temperature cycle.

The temperature range of a temperate zone that will be encountered on this study is between 2.3 and 31.8 °C allowing the use of exponential or the ratio conversion models only. Despite that the ratio conversion model provides more flexibility with the variable factor δ and the variable reference temperature T_{ref}, the exponential model will be used in this work for temperature effect of the forward models as well as, for the correction of the inversion results of the temperature effected electrical resistivity tomography (ERT). This is because data used are mostly synthetic so no requirement for a detailed temperature conversion model exists.

2.4 Diurnal and seasonal effected resistivity horizons

Considering a homogeneous medium under a steady state temperature gradient as presented in Figure 2-5 A, with temperatures T1<T2, the intermediate horizons can be characterised by their temperature and their corresponding electrical resistivity values. The same conceptual temperature and electrical resistivity horizons can be applied in the interior of a homogeneous earth, due to the temperature difference between the centre and the surface (Figure 2-5 B). The close to surface resistivity horizons (Figure 2-5 C) are also influenced by the surface temperature oscillation and this horizons can be divided into seasonally and diurnally oscillating resistivity horizons, that are temperature effected by the corresponding surface temperature oscillation events. Figure 2-6 shows the resistivity horizons for a 24 hour period, where the diurnal surface temperature oscillation, perturbates up to -1 m into the subsurface, and as a result the resistivity horizons follow this oscillation. This work is focused both on the diurnally oscillating resistivity horizons as well as on the seasonally (also called annually) oscillating resistivity horizons.

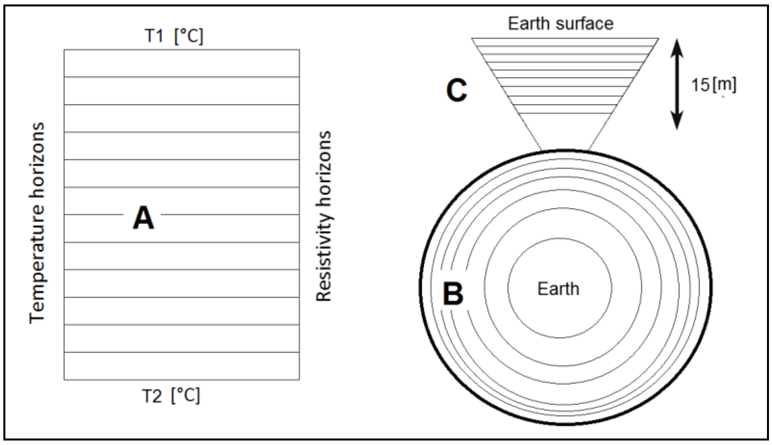

Figure 2-5 Conceptual representation of temperature and resistivity profiles for a homogenous medium across its top and bottom/center temperature boundaries.

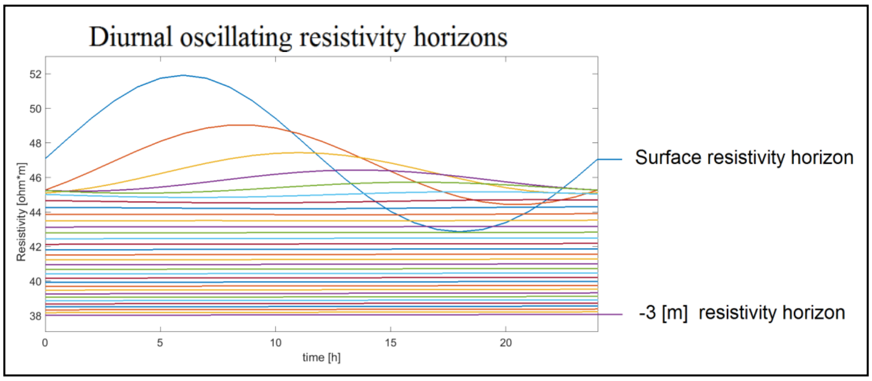

Figure 2-6 Diurnally oscillating resistivity horizons, during a 24 hour period.

2.5 Electrical resistivity methods and the ERT

Among the geophysical methods, the electrical resistivity methods like electrical resistivity profiling, sounding and imaging are used to map the spacial distribution of electrical resistivity of subsurface formations, in typical depths up to 250 m. In this study, the correction of the surface temperature effected horizons will be applied to the electrical resistivity tomography (ERT).

According to Tsourlos (1995) resistivity studies are based on the vector form of Ohm's law, that, for a homogeneous medium of electrical resistivity "ρ", quantifies the current density "J" according to how many coulombs of charge pass every second through a unit area, normal to the direction of the charge flow, when a potential **∇V** is applied by a single current electrode (Figure 2-7).

$$\boldsymbol{J} = \frac{1}{\rho} * \boldsymbol{E_{fs}} \quad \Rightarrow \quad -\frac{1}{\rho} * \ \boldsymbol{\nabla V} = \frac{\boldsymbol{I}}{2 * \pi * r^2} \qquad \text{(2-15)}$$

Where:

J	= current density A/m^2
$\mathbf{E_{fs}}$	= electric field strength N/C
ρ	= specific resistance (or electric resistivity) Ohm-m
∇V	= gradient of a scalar potential V/m
I	= current flow through the ground A
r	= distance from current electrode m

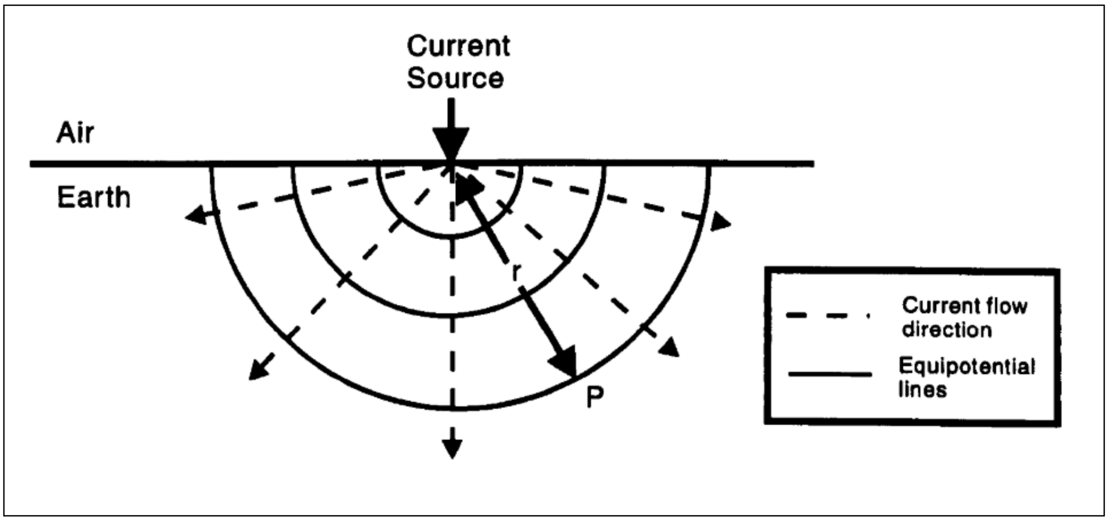

Figure 2-7 Current flow and equipotential lines as the result of a single current electrode source (from Tsourlos (1995) Figure 2.2, p. 19).

The integration of the first order differential equation (2-15) shows that, for a single source point and for a distance "r" from the source, the electric potential "V" with derived SI unit Volts V , is:

$$V = \frac{\rho * I}{2 * \pi} * \frac{1}{r} \tag{2-16}$$

Mapping the underground electric resistivity "ρ" involves the injection of electric current and the measure of electric potential difference on selected points of the surface. Figure 2-8, shows the current flow lines and the equipotencial surfaces created by the application of electric current in points A (source) and B (sink), by nailed electrodes on the ground. Points M and N represent nailed electrodes that are used for the measurement of potential difference between them. This arrangement of electrodes is called an array.

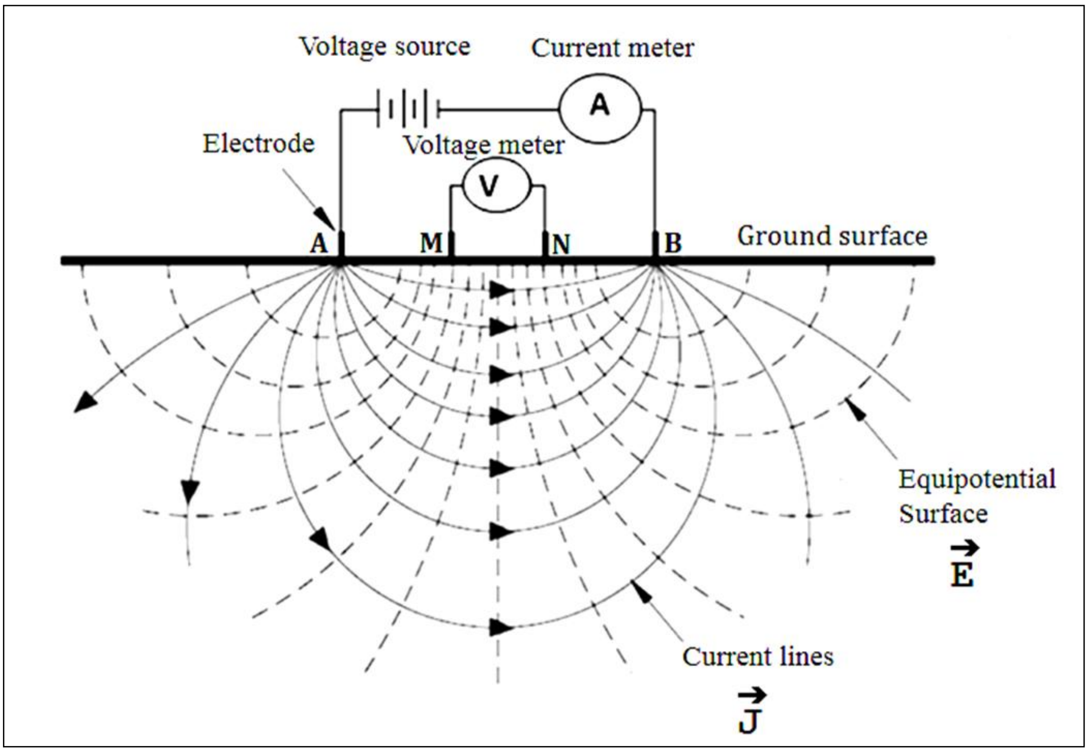

Figure 2-8 ERT method, surface potential difference measurements
(from Muchingami et al., 2012, Figures 4, p. 48).

The potentials at points M and N are given by:

$$V_M = \frac{\rho * I}{2 * \pi} \left[\frac{1}{AM} - \frac{1}{BM}\right] \tag{2-17}$$

$$V_N = \frac{\rho * I}{2 * \pi} \left[\frac{1}{AN} - \frac{1}{BN}\right] \tag{2-18}$$

The potential difference is represented with:

$$V_M - V_N = V_{MN} = \frac{\rho * I}{2 * \pi} \left[\left[\frac{1}{AM} - \frac{1}{BM} \right] - \left[\frac{1}{AN} - \frac{1}{BN} \right] \right] \quad (2\text{-}19)$$

Where

$$\rho = \frac{V_{MN}}{I} * \frac{2 * \pi}{\left[\left[\frac{1}{AM} - \frac{1}{BM} \right] - \left[\frac{1}{AN} - \frac{1}{BN} \right] \right]} \Rightarrow \rho = R * G \quad (2\text{-}20)$$

"R" is the Resistance that corresponds to the bulk geometry as an extensive property, with SI unit Ω (also used ohm). The geometrical factor "G" is used to equalize the measured resistance "R" and the electrical resistivity (specific resistance) "ρ" of the material.

$$G = \frac{2 * \pi}{\left[\left[\frac{1}{AM} - \frac{1}{BM} \right] - \left[\frac{1}{AN} - \frac{1}{BN} \right] \right]} \quad (2\text{-}21)$$

Figure 2-9, shows the geometry of the Wenner electrodes array (A,B,M,N), for 3 different geometrical factors. Red dots represent the estimated position for each calculated electrical resistivity. In case of a homogeneous medium, every calculated "ρ" is expected to have the same value.

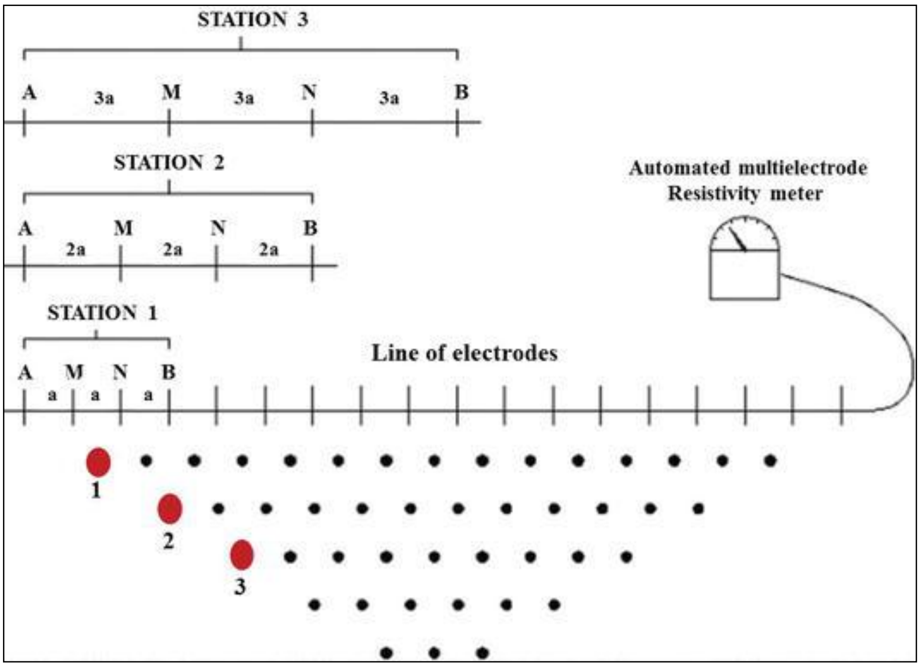

Figure 2-9 ERT measurements (from Matias & Almeida, 2017, Figures 4, p. 120).

In case of a non homogeneous resistivity medium, the measured electrical resistivity is called apparent electrical resistivity "ρ_{app}" because the calculated values have information from the bulk geometry where resistivity is not constant in space. Apparent electrical resistivity is estimated with the assumption of half space geometry.

The measured apparent electrical resistivity is a volume-averaged value affected by all the geologic formations through which the induced electric current flows. In order to calculate the distribution of "ρ" from multiple measurements of apparent electrical resistivity "ρ_{app}" of a non homogeneous medium and create the electric resistivity tomography, an array of electrodes is set on the surface of the ground and the measurements are interpreted with the inversion method.

The arrays that are often used for 2-D imaging surveys are the (a) Wenner, (b) Schlumberger (c) dipole-dipole, (d) pole-dipole and (e) pole-pole. Among the characteristics of an array that should be considered are:

- the sensitivity of the array to the vertical and horizontal changes in the subsurface resistivity
- the depth of investigation
- the horizontal data coverage
- the signal strength
-

As a result of using different electrode configurations, the geometrical factor "G" of each array is changing. Figure 2-10, presents the configuration of some common arrays. In this study the Dipole – Dipole array was used.

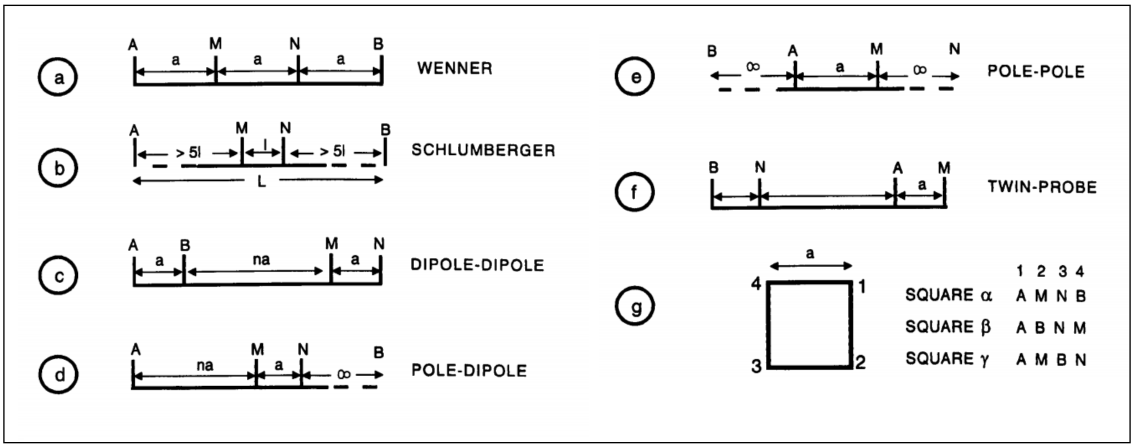

Figure 2-10 ERT electrode array types (from Tsourlos (1995) Figure 2.8, p. 32).

Modeling and Inversion

An inversion procedure is the standard processing tool applied to geoelectrical data in order to "transform" the measured apparent resistivity data into a model of the "true" subsurface electrical resistivity. Inversion method is an optimization process that iteratively changes the electrical resistivities of an initial model, in order to minimize the error between the measured and the calculated values of apparent electrical resistivity. The overall purpose of the inversion algorithm is to iteratively find a 2D subsurface resistivity model that will produce calculated data which are as close as possible to the actual ones measured in the. A measure of the quality of the produced model is the % misfit between the actual and the calculated observations.

In this work the forward and inversion processing was performed using the res2Dmod (Figure 2-11 A) and red2Dinv (Figure 2-11 B) software package (Loke et al., 2003). The red2Dinv program performs smoothness constrained inversion using either L1 or L2 norm inversion schemes and is based on a finite element forward solver. The software offers the ability to establish an inverse model through setting the mesh system and inversion blocks.

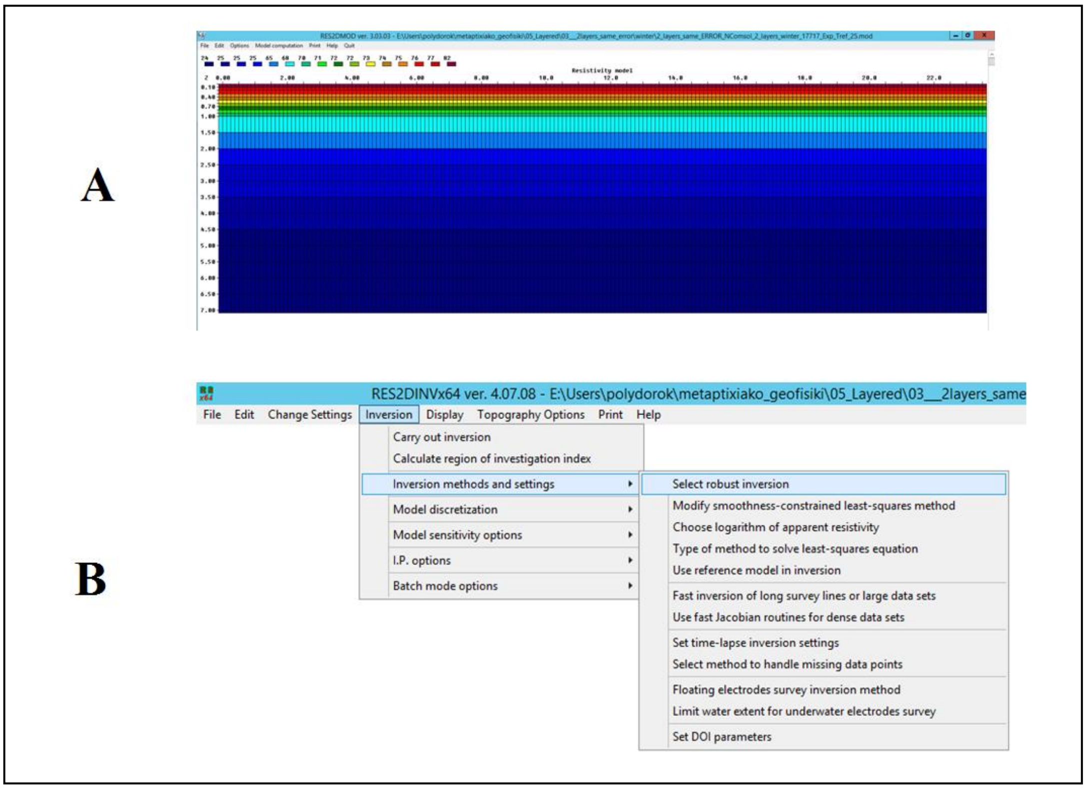

Figure 2-11 Forward and inverse electrical resistivity software.

3. Methodology for the ERT temperature correction

In this chapter the methodology followed for the correction of the ERT inversion results, is described. In the beginning, the subsurface formation properties are determined, and then the surface temperature oscillation events are classified. What follows is the calculation of subsurface temperature profile, where based on the depths of the inversion results and the selected "temperature – electrical resistivity" conversion model, the electrical resistivities are converted to a reference temperature. Finally, the graphical user interface that was created for the surface temperature correction of the surface temperature effected inversion results (inverted with DC2DPro or Res2DInv software), is presented.

3.1 Determination of formation's thermal properties.

For the calculation of conductive heat transfer, the heat properties of thermal conductivity k with unit W/(K*m), heat capacity per unit mass (constant pressure) cP with unit J/(K*kg), density ρ_d with unit Kg/m^3 or heat capacity per unit volume (volumetric heat capacity) VHC with unit J/(K*m^3), are required.

The values of the heat properties are usually calibrated based on the conditions of the study area, but for the purpose of this work we used typical property values found in literature. The values of thermal properties and electrical resistivity that are represented in Table 3-1, are based on bibliographical references (Abu-Hamdeh, 2003), (Hillel, 2004) (Wang et al. 2017c). The heat values of the last column of Table 3-1, that represent a homogeneous clay model, were used for the forward homogeneous models that will be shown in next chapters.

	Phases			Clay			
	Hillel 2004			Abu-Hamdeh 2003		Wang 2017	***Homogeneous clay model***
	Air	Water	Solid minerals average	Clay (Values range)		Clay	Clay
Grain size composition <0.075 mm						100%	
Saturation %						59.9	
Moisture content Kg/Kg				0	0.25		
Electrical resistivity ρ: Ohm-m						33.32	30
Thermal conductivity k : W/(m*K)	0.025	0.57	2.9			1.88	1.88
Density ρ_d : 10^3 Kg/(m^3)	0.00125	1	2.65	1.2	1.4		1.3
Heat capacity per unit Mass cP : 10^3 J/(kg*K)	1	4.2	0.75	1.17	2.25		1.71
Heat capacity per unit Volume C : 10^6 J/(m^3*K)	0.00125	4.2	2	1.48	3.54		2.223
Reference temperature ^{o}C							25

Table 3-1 Physical properties used for the homogeneous forward models.

3.2 Expression of surface temperature oscillation

For the calculation of the subsurface temperature profile, the acquisition of the surface temperature oscillation history is needed. In this work, the actual act of measuring the surface temperature oscillation with a monitoring process was not included, but when temperature data is monitored, it should be mentioned that there is also a temperature lag between skin surface temperature and temperature measured at higher elevation from the surface of the surveyed formation, e.g. there is 2 hours temperature lag at +2 m from the surface in comparison to the temperature oscillation at the skin surface (Jin et al. 2014).

For the purpose of this study, the history of the surface temperature was acquired from the monitored data of the Department of Meteorology and Climatology of Aristotle University of Thessaloniki (A.U.Th.) at 40.37N, 22.57E and altitude 31 m.

For the calculation of the surface temperature profile, the mean seasonal temperature amplitude and the actual diurnal temperature amplitude of the surveyed day are needed.

Mean seasonal temperature oscillation amplitude

For the acquisition of the seasonal oscillation amplitude, the data of the last twelve monitored months of the surface temperature oscillation are needed. Table 3-2 presents data like these, but instead of the last 12 months, this table shows the mean temperatures for the period 1930 – 2005 provided by the A.U.Th. Meteorology station. These records will be used in order to impose the temperature effect to the forward models in the following chapters, as well as to correct the inversion results. The methodology presented below, for the calculation of the seasonal temperature amplitude, is the same for the application of the correction using the actual 12 months temperature recordings prior to the conduction of the ERT survey.

The variables required for the calculation of the mean seasonal temperature amplitude are presented below.

1. Mean annual temperature $\mathbf{T_m}$
2. Annual maximum temperature $\mathbf{T_{amax}}$
3. Mean diurnal temperature amplitude $\mathbf{T_{mda}}$
4. Seasonal variation of mean diurnal temperature amplitude $\mathbf{T_{vda}}$

Temperature Table °C				
	Mean	Mean maximum A	Mean minimum B	Diurnal Amplitude =(A-B)/2
Jen.	6.0	9.6	2.3	3.7
Feb.	7.4	11.6	3.2	4.2
Mar.	10.1	14.4	5.7	4.4
May.	14.4	19.3	9.6	4.9
Apr.	19.4	24.6	14.2	5.2
Jun.	23.7	29.2	18.3	5.5
Jul.	26.2	$\mathbf{T_{amax} = 31.8}$	20.7	**5.6**
Aug.	26.0	31.5	20.5	5.5
Sep.	22.2	27.4	16.9	5.3
Oct.	17.1	21.7	12.5	4.6
Nov.	12.1	16.0	8.2	3.9
Dec.	7.7	11.3	4.1	**3.6**
Annual	$\mathbf{T_m = 16.1}$	20.8	11.4	$\mathbf{T_{mda} = 4.7}$

Table 3-2 Auth meteorology station mean temperatures 1930 – 2005.

The mean annual temperature T_m for this period is $\mathbf{T_m = 16.1}$ **°C.** The temperature's mean annual maximum T_{amax} appears during July with $\mathbf{T_{amax} = 31.8}$ **°C.** According to maximum and minimum temperatures of every month, the temperature's mean diurnal amplitude T_{mda} was calculated as $\mathbf{T_{mda}= 4.7}$ **°C.** Finally, the seasonal variation of diurnal amplitude T_{vda} (the half of the difference between maximum and minimum diurnal amplitudes at last column of Table 3-2) has amplitude equal to $\mathbf{T_{vda} = 1}$ **°C.** The mean seasonal amplitude $\mathbf{T_{msa}}$ can be estimated with the equation (3-1).

$$T_{msa} = T_{amax} - T_m - T_{mda} - T_{vda} \tag{3-1}$$

Actual diurnal temperature oscillation amplitude of the surveyed ERT

The actual diurnal surface temperature amplitude $\mathbf{T_{ada}}$, for which the ERT is going to be corrected, is acquired as the half of the difference between the minimum and maximum temperatures during the 24 h period before the surveyed ERT equation ((3-2).

$$T_{ada} = \frac{Diurnal\max - Diurnal\ min}{2} \tag{3-2}$$

3.3 Subsurface temperature calculation and temperature correction.

For the heat properties described in chapter 3.1 (clay formation) and the surface temperature condition described in chapter 3.2 (using as actual diurnal amplitude 4.7 ℃ with oscillating deviation 1 ℃ during the annual cycle), Figure 3-1 presents the surface temperature history and the subsurface temperature profile of the first day and first hour of the year.

Figure 3-1 A, upper blue graph, shows the temperature profile with time for a period of one year, while B anc C upper blue graphs shows the time scale in logarithmic scale. Figure 3-1 A and B correspond to a winter date (time ID:010101) while C correspond to a summer day during July (time ID:071008).

Downright red graphs of Figure 3-1, shows the temperature profile with depth. A and B red lines, present the same subsurface temperature profile, during the first hour of the year that is the result of previous six months surface temperature activity, As a result, due to the heat transition that gained during summer period, 6 months before the winter date that subsurface temperature profile represents. The perturbation depth of the diurnal temperature effect is also labelled in this graph with depths of about 0.3 m, while the annual (seasonal) perturbation depth is labelled as the result of the annually oscillating harmonic of the temperature oscillation at earth's surface. The same perturbation depths can be seen in Figure 3-1 C, during a summer surface day.

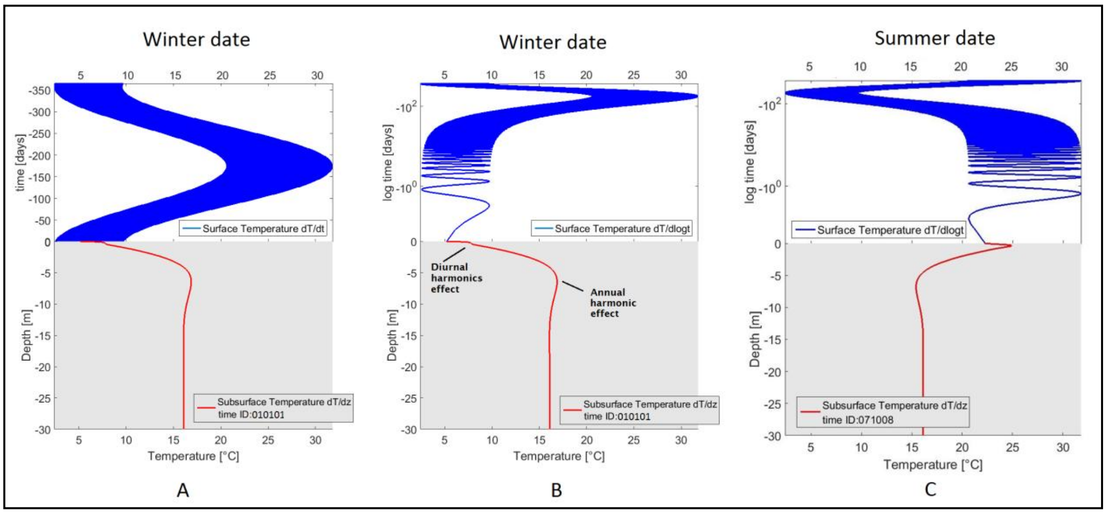

Figure 3-1 Upper graphs show the surface temperature history, while bottom graphs show the subsurface electrical resistivity profiles during the selected time.

In order to correct the temperature effected inversion results, the soil's temperature profile has to be calculated based on the surface temperature oscillation history, the thermal diffusivity of the formation, the depths of the inversion results, the temperature at the highest depth of the ERT and the and the time that the survey was held. For the calculation of the subsurface temperature profile, the equation (3-3) was used (modified by Hillel, 2004).

$$T(z,t) = T_{ssz} + T_{msa} * \mathrm{e}^{-\left(\frac{z}{d_a}\right)} * \sin\left(\omega_a * t + \varphi_a - \frac{z}{d_a}\right) + T_{ada} * \mathrm{e}^{-\left(\frac{z}{d_d}\right)} * \sin\left(\omega_d * t + \varphi_d - \frac{z}{d_d}\right) \quad (3\text{-}3)$$

$T(z,t)$ is the temperature at the selected time of the year and depth

z is the selected depth (z ≥ 0 m)

t is the selected hour of the year (t hours)

T_{ssz} is the steady state temperature at depth z, caused by the temperature difference of the surface and the deep horizons

$T_{ssz}(z) = T_m + \theta * z$

T_m is the mean annual surface temperature

θ is the coefficient of the steady state temperature gradient

$$\theta = \frac{\text{bottom temperature } T_{ssz}(L) - \text{mean surface temperature } T_m}{L}$$

$L =$ depth of bottom temperature (L$\geq$ 0 m)

T_{msa} is the mean seasonal oscillation amplitude

$T_{msa} = T_{amax} - T_m - T_{mda} - T_{vda}$

T_{ada} is the actual temperature amplitude of the surveyed day

$$T_{ada} = \frac{\text{Diurnal max} - \text{Diurnal min}}{2}$$

ω_a is the annual radial frequency = 2*π / (365*24)

φ_a is the phase change of annual temperature oscillation

$\varphi_a = (3 * \pi)/2 - (a * 24 * \omega_a)$,*a = min temperature day of the year (0-364)*

ω_d is the diurnal radial frequency = 2*π / 24

φ_d is the phase change of diurnal temperature oscillation

$\varphi_d = (3 * \pi)/2 - (b * \omega_d)$, *b = min temperature hour of "a" (0-23)*

D is the thermal diffusivity of the homogeneous medium

d_a is the damping depth of annual temperature oscillation = sqrt (2* D/ω_a)

d_d is the damping depth of diurnal temperature oscillation = sqrt (2* D/ω_d)

The correction of the surface temperature effected ERTs uses the temperatures that was calculated for the depths of the inversion results, and in conjunction with a selected "electrical resistivity – temperature" conversion model, the corresponding electrical resistivity of each depth is converted to a reference temperature, specified by the conversion model.

3.4 Temperature correction and correction logistics

The necessary variables needed for the correction of an electrical resistivity tomography inversion results, are inserted to the algorithm using a matlab graphical user interface (GUI), which includes the correction algorithm that exports the temperature corrected inversion results from the dc2Dpro or the res2Dinv software. Figure 3-2 presents a concept map of the correction algorithm.

Input of variables

The GUI is divided into four panels, where a set of 14 basic variables and some extra options are imported from the user.

- The 1st panel imports the ERT inversion results and the exact date, time that survey was carried out.
- Panel number 2 holds the surface temperature variables, for the calculation of the near subsurface temperature profile.
- Panel number 3 holds the variables that describe the heat properties of a homogeneous medium.
- Panel number 4 has choices for the correction process that will be applied to the inverted ERT data.

Export

- Temperature corrected inversion results.

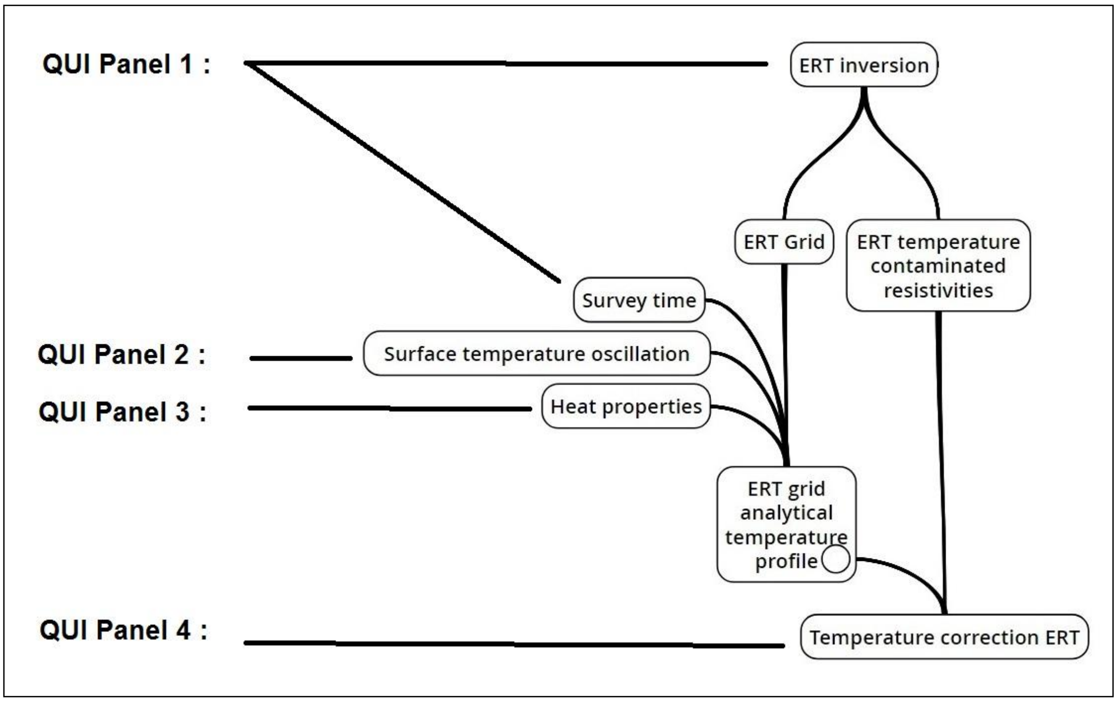

Figure 3-2 Concept map of the correction algorithm.

Panel number 1

On TRC (Temperature Resistivity Conversion) panel number 1 (Figure 3-3), the inversion results produced either by DC2DPro or Res2DInv software can be imported. The time ID (time that the survey took place) based on the Gregorian calendar, no leap year, should be stated as the last 6 digits of the file name with the form of “MMDDHH” [month, day, hour]. The values for the month range are 01-12, for the day range 01-31 and for the hour range are 00 - 23.

Import 01 : Survey time

The survey time will determine the selected temperature profile, among the profiles of each hour of the year.

Import 02 : Inversion results

The algorithm uses the depths of the inversion’s grid and creates a table of depths. Based on these depths the temperature profile is being calculated.

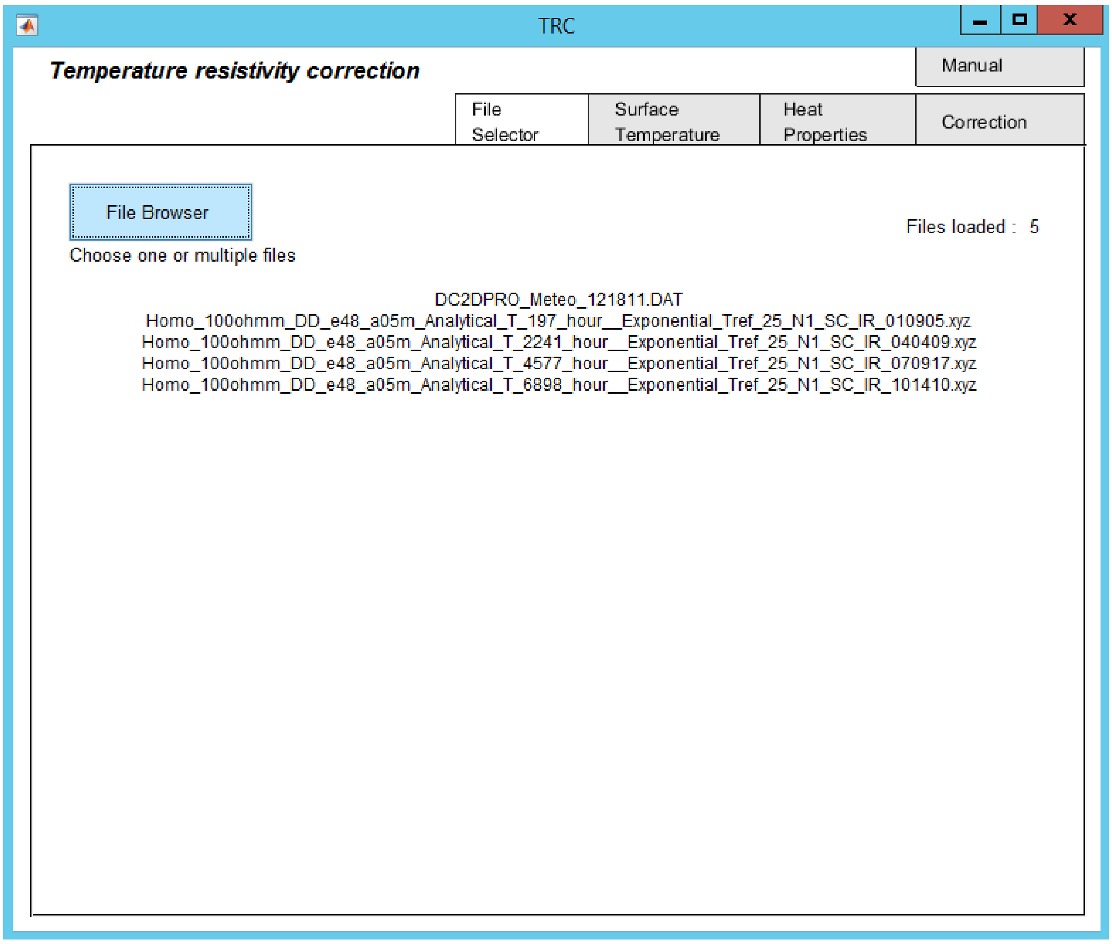

Figure 3-3 GUI panel number 1: Inversion data import.

Panel number 2

Surface temperature oscillation is imported in panel number 2, where a set of variables describe the harmonics that the temperature oscillation consists of (Figure 3-4).

Import 03 : Minimum annual temperature (T_{amin})
Import 04 : Maximum annual temperature (T_{amax})
Import 05 : Mean diurnal temperature amplitude (T_{mda}).
Import 06 : Seasonal variation of diurnal's amplitude (T_{vda})
Import 07 : Actual diurnal's amplitude of surveyed day (T_{ada})

Import 08 : Day of the year with the minimum temperature (0-364)
Import 09 : Hour of the day with minimum temperature (0-23)

Import 10 : Selected depth for temperature determination
Import 11 : Temperature at the selected depth

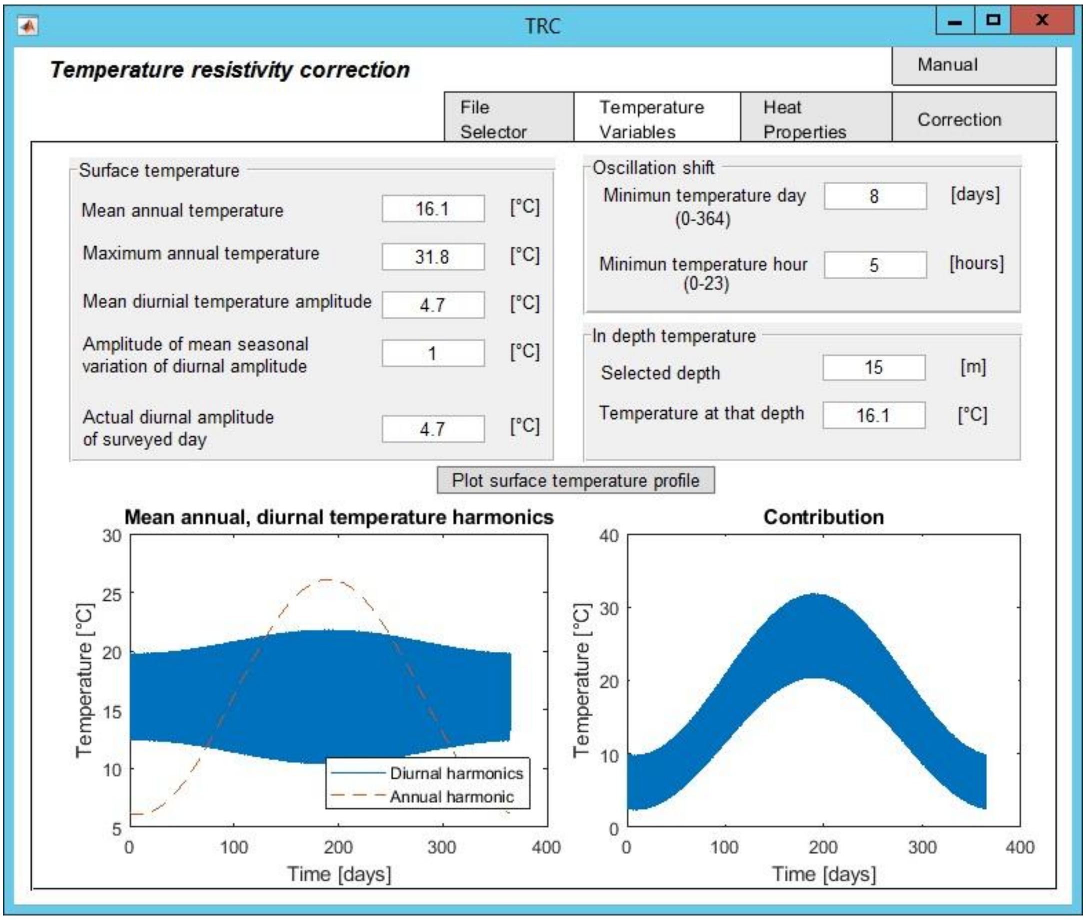

Figure 3-4 GUI panel number 2: Surface temperature data import.

Panel number 3

In order to describe the conductive heat propagation in a homogeneous medium, user can choose either to input the thermal diffusivity or the variables usually used in bibliography (Figure 3-5). These variables are 1) the thermal conductivity and the heat capacity per unit volume (constant pressure) or 2) the thermal conductivity, the heat capacity per unit mass and the density.

Import 12 : Thermal diffusivity
Import 12.1 : Thermal conductivity
Import 12.2 : Heat capacity per unit volume
Import 12.3 : Heat capacity per unit mass
Import 12.4 : Density

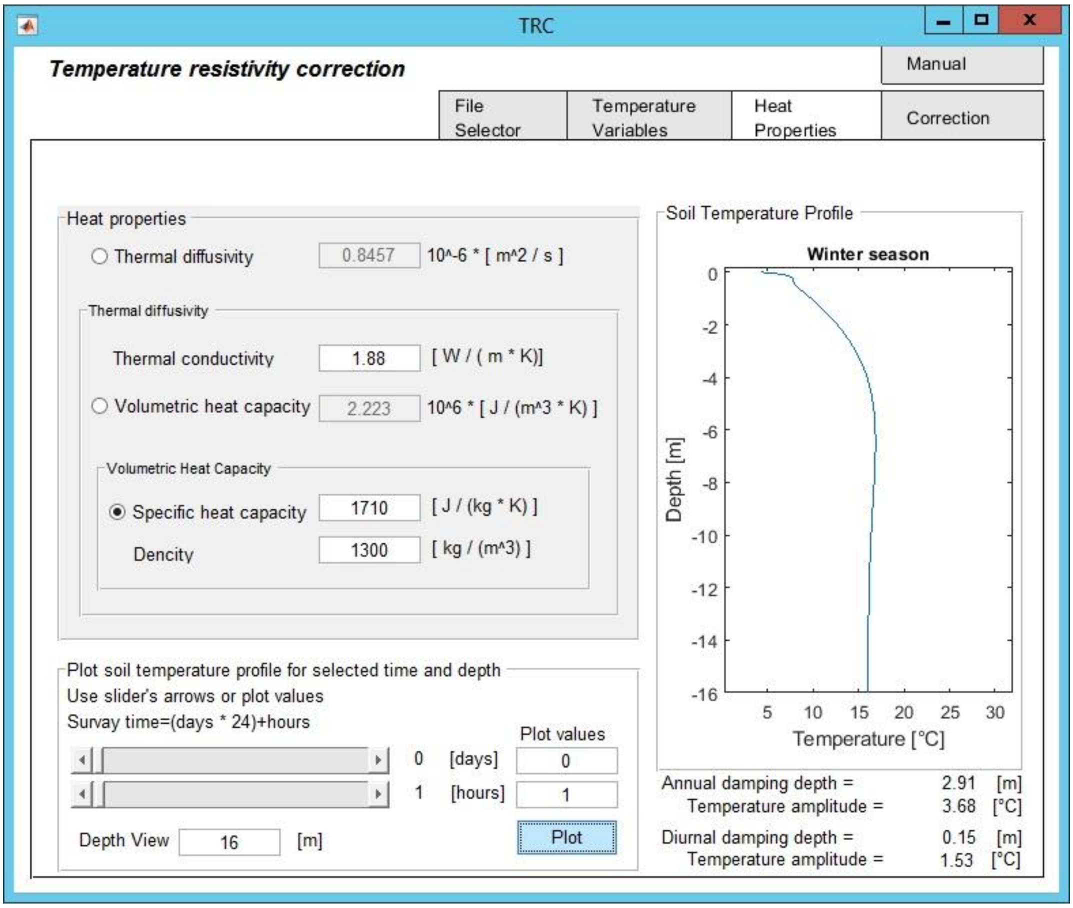

Figure 3-5 GUI panel number 3: Heat properties import.

Panel number 4

Panel number 4 (Figure 3-6) has choices for the correction process, such as the conversion model that will be used, and the export of visual and corrected inversion results. User can choose between 3 conversion models and fill in the necessary information. In cases where the temperature ranges are in agreement with the limits of power function conversion model (Besson et al. 2008), this model can be used. In case of low resolution ERT, the mean temperature of the inversion block can be used.

Import 13 : Conversion model selection
Import 13.1 : Ratio's model temperature coefficient of resistance δ
Import 13.2 : Ratio's model reference temperature
Import 13.3 : Power's function model reference temperature
Import 14 : Inversion block divisions for the calculation of inversion's block mean temperature.

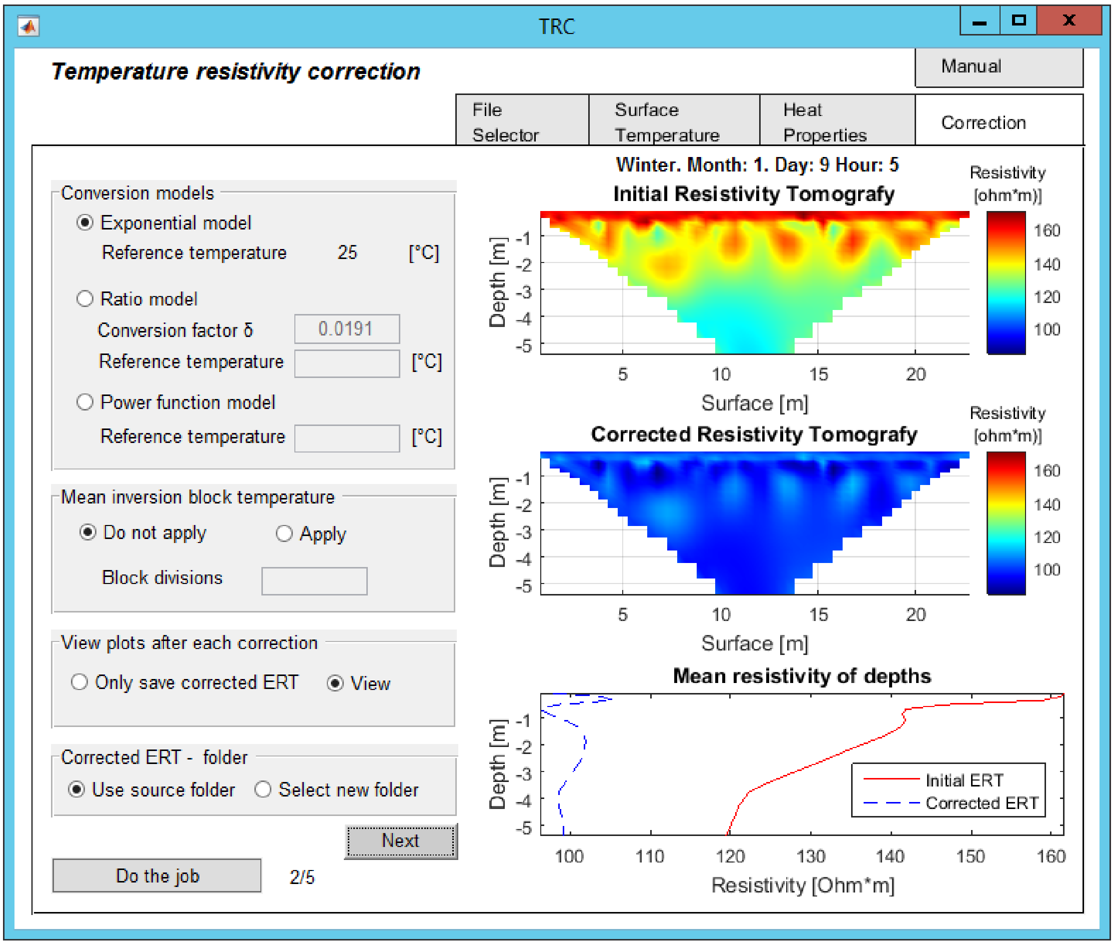

Figure 3-6 GUI panel number 4: Correction choices.

4. Validation of the correction approach

In this chapter, the methodology followed for the acquisition of reference and temperature effected inversion results with the use of forward modelling for the validation of the correction process, is presented.

The approach for the validation of the temperature correction, is based on the creation of "temperature reference" and "surface temperature effected" forward models of homogeneous and inhomogeneous geometries/formations. The accuracy of the inversion results to detect the temperature effect and the RMS error between the "reference temperature inversion results and the temperature corrected inversion results", present the validity of the correction's approach.

4.1 Forward and inverse surface temperature effected models

In order to import the temperature effect into the reference temperature forward models, the work flow followed the steps below:

1. Expression of surface temperature boundary condition.
2. For the above surface temperature boundary condition and a homogenous formation, comparison of the subsurface temperature profiles provided by the numerical simulation of heat transition and the corresponding analytical solution.
3. Use of the calculated temperature profiles in conjunction with the exponential conversion model to temperature-effect the reference resistivity values of the homogeneous forward models.
4. Numerical simulation of heat transition for inhomogeneous formations and acquisition of the temperature profiles.
5. Use of the calculated temperature profiles to temperature-effect the inhomogeneous forward models.
6. Inversion of the forward models.

4.2 Expression of surface temperature boundary condition

During an annual cycle, two major surface temperature oscillation events occur, the seasonal and the diurnal. A 3rd temperature oscillation event, with smaller amplitude was added to the surface temperature condition, to include the effect caused by the seasonal variation of diurnal's amplitude between summer and winter seasons. In Figure 4-1 left is plotted the seasonal oscillation event with dashed line, while with continuous line, the diurnal oscillation with the variation of its amplitude during the annual cycle, is presented. The total interference of these events are presented to the right side of Figure 4-1 compared to the mean hourly temperatures from the hourly monitored temperature data of the department of meteorology and climatology of Aristotle University of Thessaloniki (A.U.Th.) for the period 1951-2002.

For the expression of the surface temperature boundary condition, the temperature data of Table 3-2 was used. This table is represented again in the next page, in order to help readers follow the acquisition of the necessary variables.

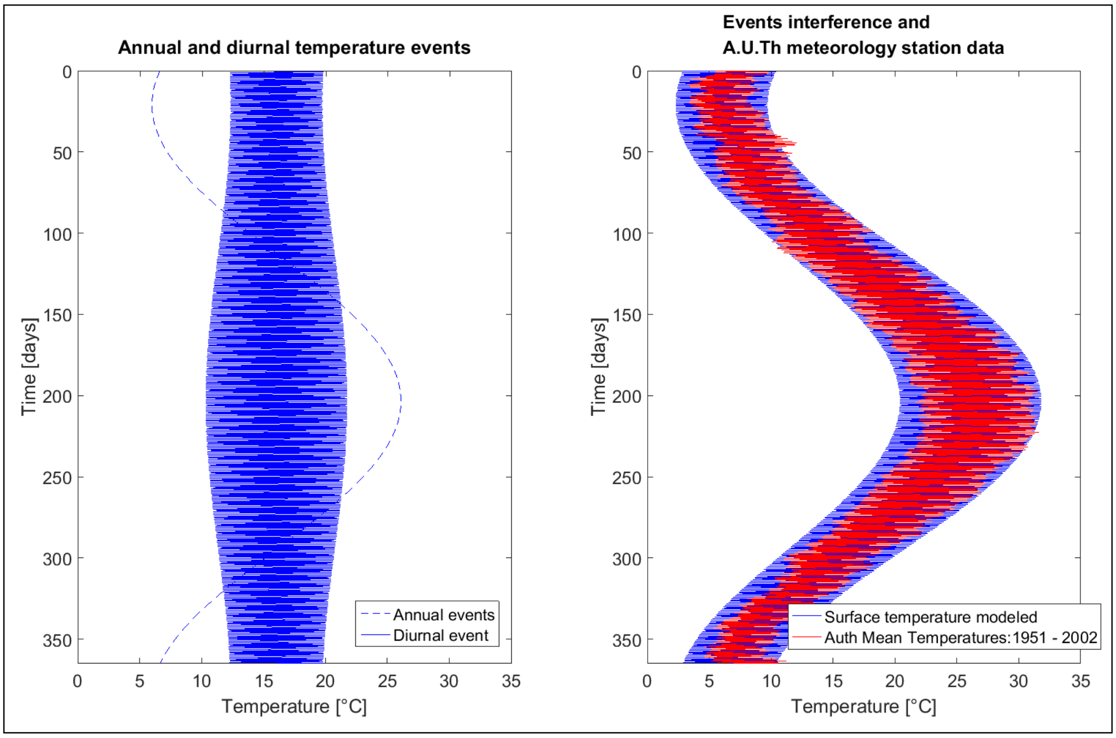

Figure 4-1 Surface temperature oscillation. Left graph, diurnal and annual temperature oscillation harmonics. Right graph, interference and comparison with real data.

Temperature Table °C				
	Mean	Mean Maximum A	Mean Minimum B	Diurnal Amplitude =(A-B)/2
Jen.	6.0	9.6	**T_{amin} = 2.3**	3.7
Feb.	7.4	11.6	3.2	4.2
Mar.	10.1	14.4	5.7	4.4
May.	14.4	19.3	9.6	4.9
Apr.	19.4	24.6	14.2	5.2
Jun.	23.7	29.2	18.3	5.5
Jul.	26.2	**T_{amax} = 31.8**	20.7	**5.6**
Aug.	26.0	31.5	20.5	5.5
Sep.	22.2	27.4	16.9	5.3
Oct.	17.1	21.7	12.5	4.6
Nov.	12.1	16.0	8.2	3.9
Dec.	7.7	11.3	4.1	**3.6**
Annual	**T_m = 16.1**	20.8	11.4	**T_{mda} = 4.7**

Table 3-2 Mean temperatures of period 1930 – 2005. Auth meteorology station data.

The mean seasonal temperature is T_m = 16.1 °C. The temperature's mean annual maximum appears the month July with T_{amax} = 31.8 °C while the temperature's mean annual minimum T_{amin} = 2.3 °C appears at January.

If the mean annual temperature T_m, was calculated as the half of the difference between mean maximum and mean minimum temperature of the year, $T_m = (T_{amax} - T_{amin})/2$, the result would be a mean annual value of 17.05 °C instead of 16.1 °C . In order to achieve 16.1 °C as the mean temperature, firstly the deference of T_{amax} = 31.8 °C and T_m = 16.1 °C sets the initial temperature amplitude equal to 15.7 °C , and as a result, for T_m = 16.1 °C the new annual range of temperature that will be used, is T_{amax} = 31.8 °C and T_{amin} = 0.4 °C . According to maximum and minimum temperatures of every month, the temperature's mean diurnal amplitude T_{mda} was calculated as T_{mda} = 4.7 °C. The mean diurnal amplitude was subtracted from the initial temperature amplitude. Finally, the seasonal variation of diurnal amplitude T_{vda} (the half of the difference between maximum and minimum diurnal amplitudes at last column of Table 3-2) with amplitude of T_{vda} = 1 °C was also subtracted from the initial amplitude.

In order to set the actual diurnal oscillation during the annual cycle, the mean diurnal oscillation combined with a sinusoidal function of 1 °C that has the same period and the phase with the diurnal oscillation, was used.

The function that used and stands for the surface temperature boundary condition is presented with eq. (4-1):

$$T(0,t) = T_m + T_{msa} * \sin(\omega_a * t + \varphi_a) + (T_{mda} + T_{vda} * \sin(\omega_a * t + \varphi_a)) * \sin(\omega_d * t + \varphi_d) \quad (4\text{-}1)$$

Where :

$T(0,t)$ is the surface temperature at a specific hour of the year
T_m is the annual mean temperature
$T_{msa} * \sin(\omega_a * t + \varphi_a)$ is the seasonal oscillation
$(T_{mda} + T_{vda} * \sin(\omega_a * t + \varphi_a)) * \sin(\omega_d * t + \varphi_d)$ is the actual diurnal oscillation

and :

t is the selected hour of the year
T_m is the mean annual temperature
T_{msa} is the mean seasonal amplitude
$T_{msa} = T_{amax} - T_m - T_{mda} - T_{vda}$
T_{mda} is the mean diurnal amplitude
T_{vda} is the seasonal variation of diurnal amplitude
ω_a is the annual radial frequency = 2*π/(365*24)

φ_a is the phase change of annual temperature oscillation

$$\varphi_a = \frac{3*\pi}{2} - \left(a * 24 * \omega_y\right) \qquad \textit{a = min temperature day of the year (0-364)}$$

ω_d is the diurnal radial frequency = 2*π/24

φ_d is the phase change of diurnal temperature oscillation

$$\varphi_d = \frac{3*\pi}{2} - \left(b * \omega_d\right) \qquad \textit{b = min temperature hour of “a” (0-23)}$$

The result of equation (4-1) using the temperature data of Table 2-3 with values T_{amax} = 31.8 °C, modified T_{amin} = 0.4 °C, T_{mda} = 4.7 °C, T_{vda} = 1 °C, arbitrary selected a = 8 days and arbitrary selected b=5 hours, is an oscillation with mean value T_m = 16.1 °C, T_{max} =31.8 °C and T_{min} 2.4 = °C, plotted with blue colour in Figure 4-1 right.

4.3 Numerical simulation and analytical solution of heat transition

The surface boundary condition of equation (4-1) was numerically simulated with the Comsol multiphysics software, that is a simulation program that solves the differential equations of selected physics. Using heat transfer module, the numerical simulation was held for five years, using only the conduction physics where no mass movement or phase change take place. Top boundary was set to be a Dirichlet boundary condition (temperature boundary), which for this case, specifies the surface temperature oscillation with the equation (4-1). Assuming that in depth, where surface temperature influence and earth interior temperature influences are zero, the temperature should be equal to the mean surface temperature, so bottom boundary condition was also set to be a Dirichlet boundary with the value of mean annual temperature T_{ssz} (L)=16.1. The other sides were set to be insulated.

A swept mesh with element ratio distribution, was used to construct the mesh (Figure 4-2 A). The simulation was done for a time range of five years, with one hour time step and a relative tolerance equal to 0.0001. The results of the simulation with “the mean annual temperature” as initial temperature condition of the medium or “the results of the analytical solution equation (3-3)”, where the same for the 3rd and the next year. Simulation result for the 1st hour of the 3rd year is shown in Figure 4-2 B, while the temperature profile for this hour is presented in Figure 4-2 C.

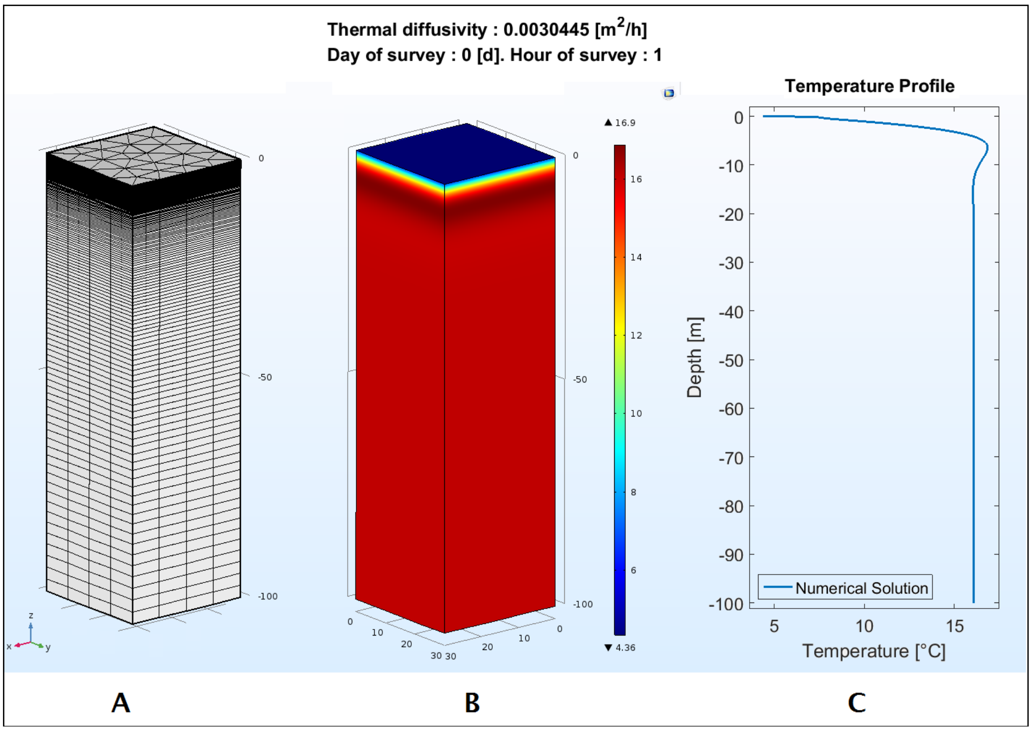

Figure 4-2 Numerical solution of heat transition for a homogeneous medium with common soil heat properties and a Mediterranean climate surface boundary condition.

The results of the numerical simulation and the analytical solutions are presented in Figure 4-3. The temperature profiles (analytical and numerical) represent the homogenous clay formation with mid thermal diffusivity equal to 0.8 * 10^{-6} m^2/s during the first day of the year.

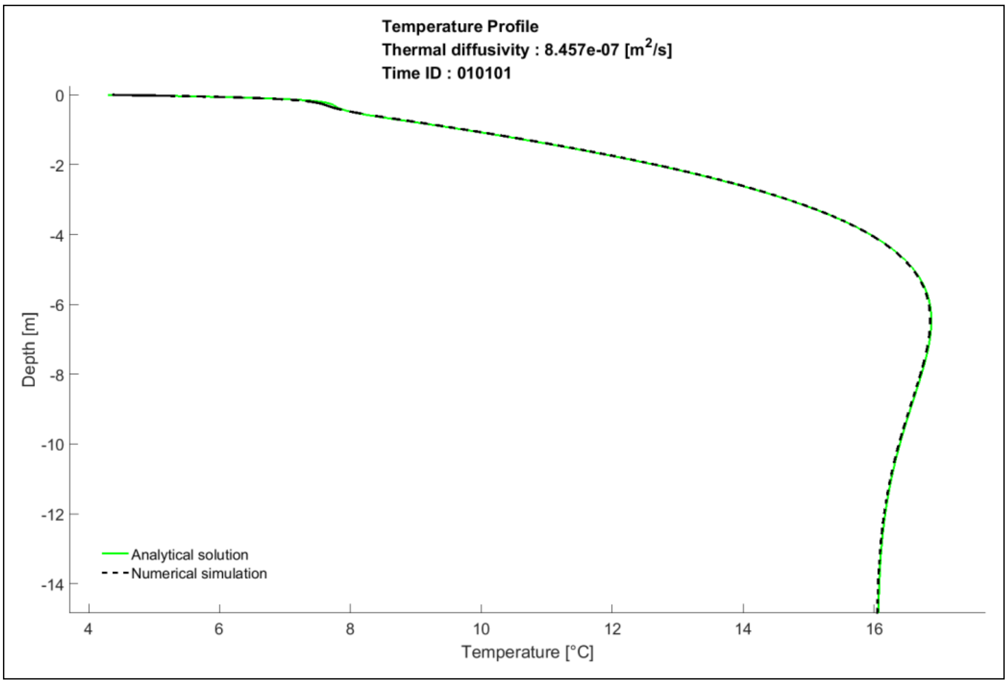

Figure 4-3 Comparison between the numerical and the analytical temperature profiles.

The hourly difference (Figure 4-4), between the numerical simulation and the corresponding analytical solution eq. (3-3), shows less than 0.5 °C misfit for the first 0.5 m, and less than 0.2 °C misfit for points deeper points.

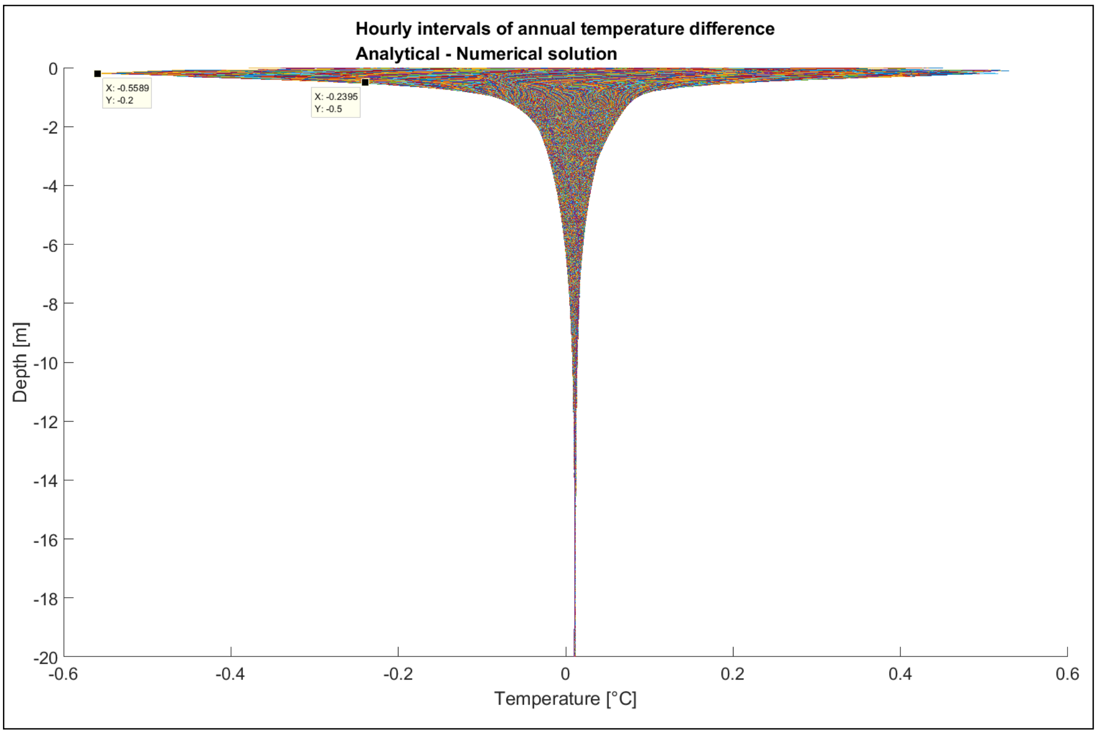

Figure 4-4 Hourly difference between the numerical and the analytical temperature profile during an annual period.

Based on the exponential conversion model and a formation with electrical resistivity 100 ohm-m at reference temperature of 25 °C, the impact of the 0.5 °C error at the first 0.5 m of soil profile will lead to a resistivity error < 0.8 Ohm-m caused by the summer's temperatures and < 2.4 Ohm-m for the effect caused by winter's temperature (Table 4-1).

	Temperature °C	Exponential conversion model. Resistivity ohm-m	Resistivity difference ohm-m
Reference	25	100	
	31.8 - 0.5	86.778	- 0.792
Maximum	31.8	87.57	0
	31.8 + 0.5	88.377	+ 0.807
	2.4 - 0.5	175.44	- 2.42
Minimum	2.4	173.02	0
	2.4 + 0.5	170.65	+ 2.37

Table 4-1 Impact of 0.5 °C difference to annual max and min resistivity values.

For a homogeneous medium, an overview of the temperature variations per hour in relation to depth for an annual cycle, is presented at Figure 4-5 and Figure 4-6.

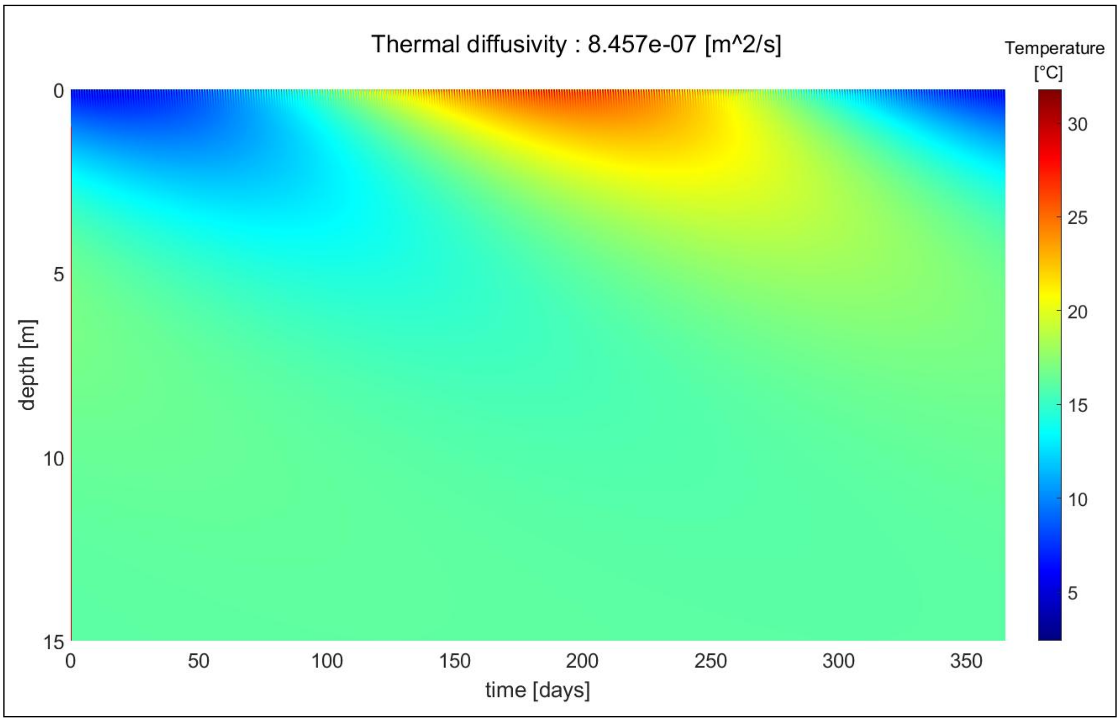

Figure 4-5 Annual overview of temperature profiles.

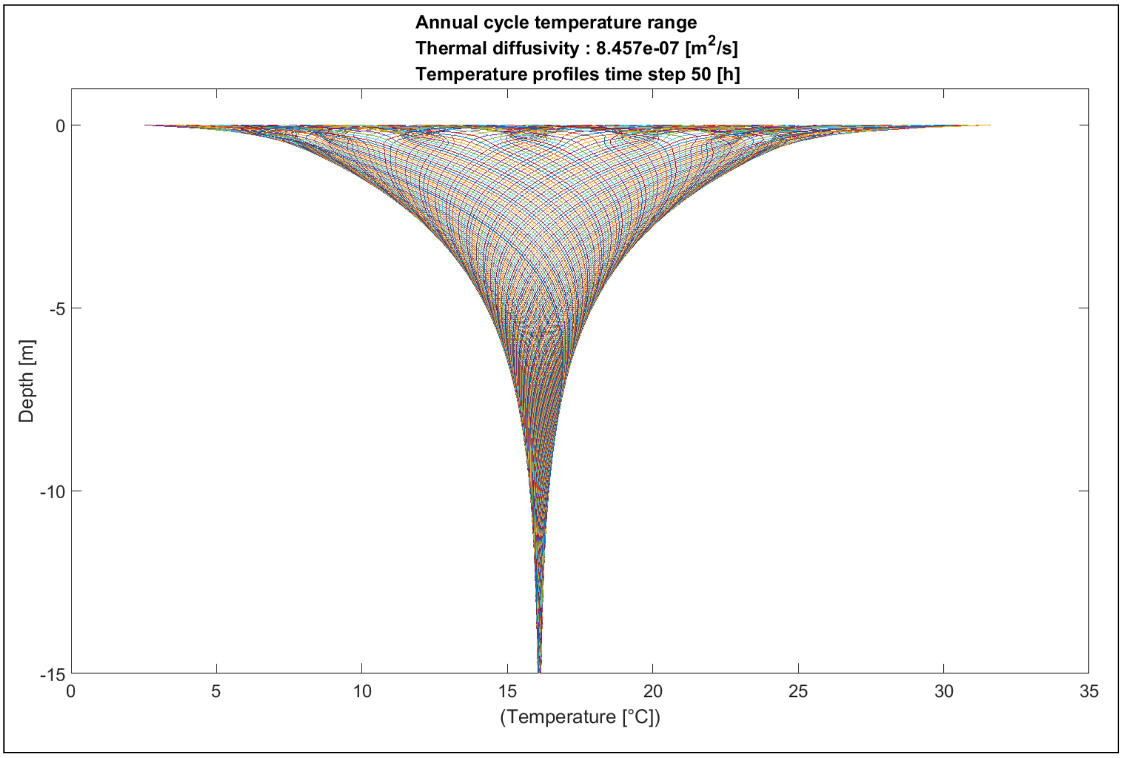

Figure 4-6 Annual overview of temperature profiles every 50 hours.

In case of homogeneous earth interior where the temperature in deeper sections is constant and different from the mean annual surface temperature $T_{ssz}(L) \neq T_m$, it seems that the linear correlation of the surface and the bottom temperatures used in the analytical solution, works fine in comparison τo the numerical simulated results.

Figure 4-7 presents three temperature profiles of a homogeneous formation. The profile of the numerical simulation was provided by a 50 year simulation with bottom temperature boundary condition to be 50 °C. The analytical solution with also $T_{ssz}(L) = 50$ °C, presents good correlation with the numerical solution for the first day of the 50th year. In the same figure and for comparison reasons is also presented the analytical solution with bottom temperature equal to the mean annual surface temperature $T_{ssz}(L) = 16.1$ °C.

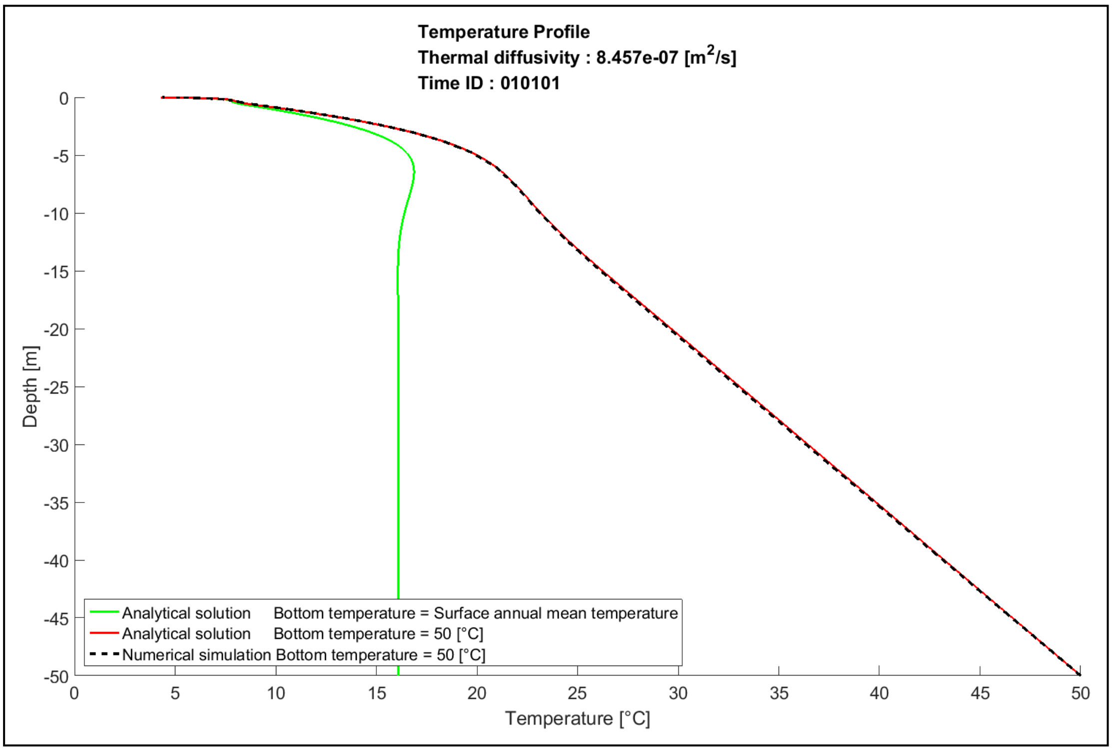

Figure 4-7 Temperature profiles of homogeneous medium with different temperatures in depth of 50 m.

All the models of this study where created with the assumption that the bottom boundary condition has temperature equal to the mean annual surface temperature, and as a result for the equation (3-3) the value $\theta=0$.

4.4 Homogeneous formations temperature effect import

The methodology needed to import the temperature effect into a homogeneous medium is presented using the example bellow. The temperature profile of Figure 4-8 left, was calculated considering a clay homogeneous medium, with heat properties as described in chapter 3.1, and setting a new reference resistivity of 100 ohm-m at rest conditions of 25 °C for the bulk medium. The values of electrical resistivity (Figure 4-8) right, which are effected by the temperature profile, are calculated based on the exponential model (2-11)

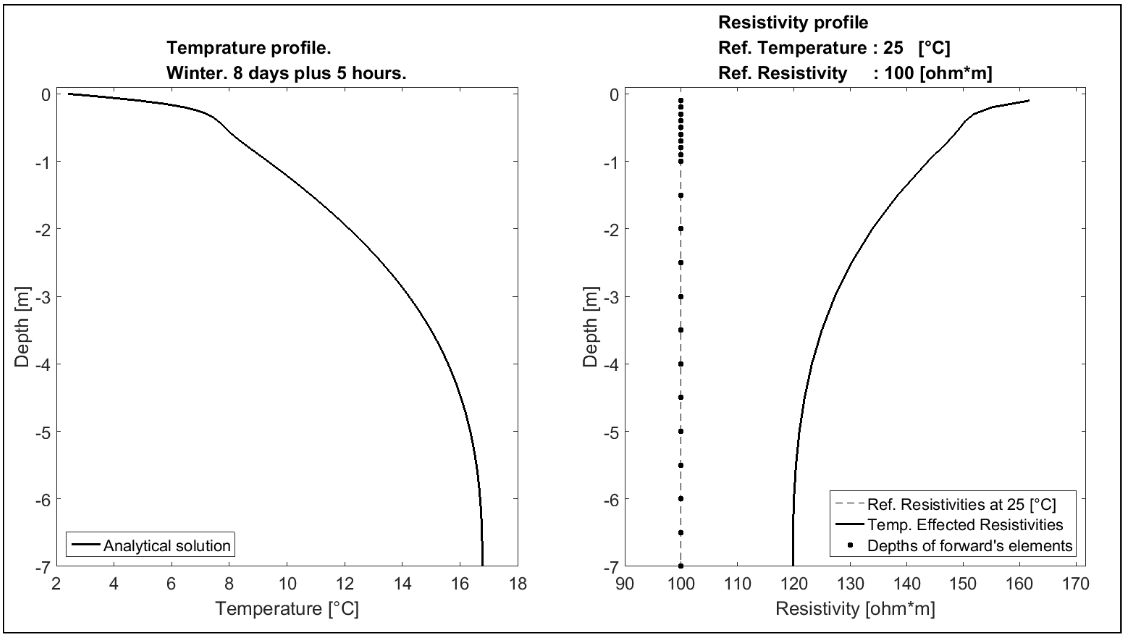

Figure 4-8 Left, calculated temperature profile. Right, reference and temperature effected resistivity profiles for a reference medium of 100 ohm-m at 25 °C.

The forward modelling of the electrical resistivity was conducted using the res2Dmod software. This software offers a set of 16 different values of electrical resistivity, up to 40 elements for different depths and unlimited horizontal elements in order to describe the forward model. In order to use an electrical resistivity forward model with good resolution and also avoid reflections, the vertical elements of the forward model was set with ranges, steps and values as (-0.1:-0.1:-1), (-1:-1:-17), -20, -30, -50, -70 m . The black dots in right graph of Figure 4-8 present these depths, only until the depth of -7 m.

Due to the limitation of 16 values for the electrical resistivity description, an algorithm was created to divide the resistivity spectrum of the temperature profile into

16 classes of electrical resistivity values, in order to fit in the software specifications (Figure 4-9). The calculated effected resistivities of each depth, were separated into classes to create the forward model (Figure 4-10) in order to be imported into the res2Dmod software.

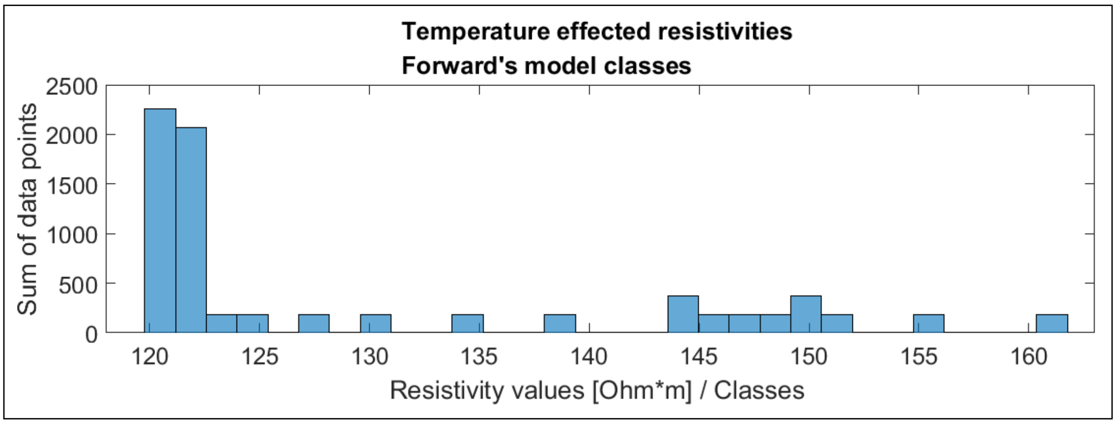

Figure 4-9 Resistivity spectrum of temperature effected models divided into classes for the creation of the temperature effected forward model.

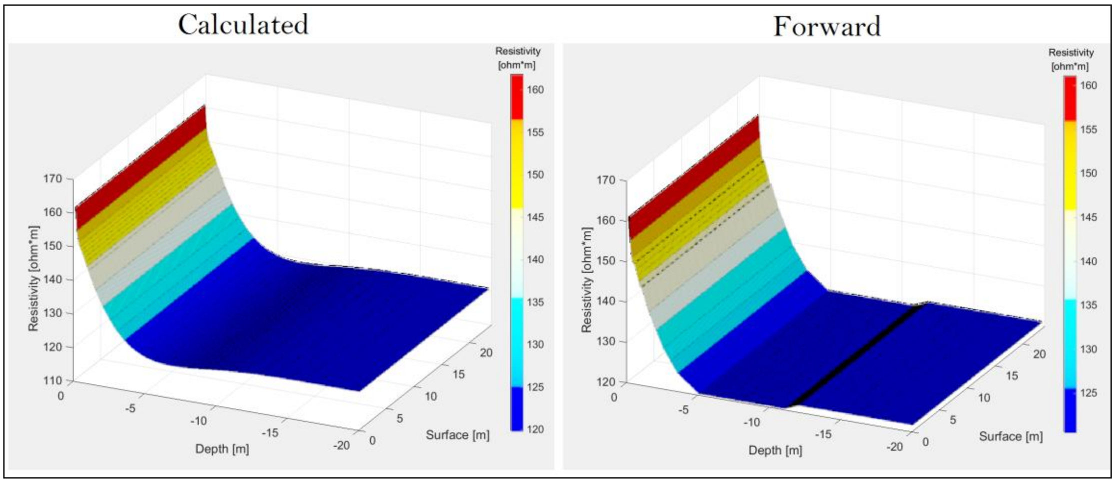

Figure 4-10 Left, Temperature effected calculated model.
Right, forward model after divided into classes for the forward model.

The reference and temperature effected forward model, were produced with the "res2dmod" software, based on a Dipole-Dipole array of 48 electrodes and 0.5 meters spacing. A noise of 3% was added to the forward. Inversion of the forward models was done using the "res2Dinv" software, with the selection of standard data constraints (L2 norm), and the first layer thickens to be 0.125 m, which increases in depth with a ratio of 1.1. Figure 4-11 shows the reference homogeneous forward model, the pseudosection and the inversion results. Figure 4-12 shows the forward, the pseudosection and the inversion results of temperature effected homogeneous model. Both inversion results will be used for the evaluation of the correction.

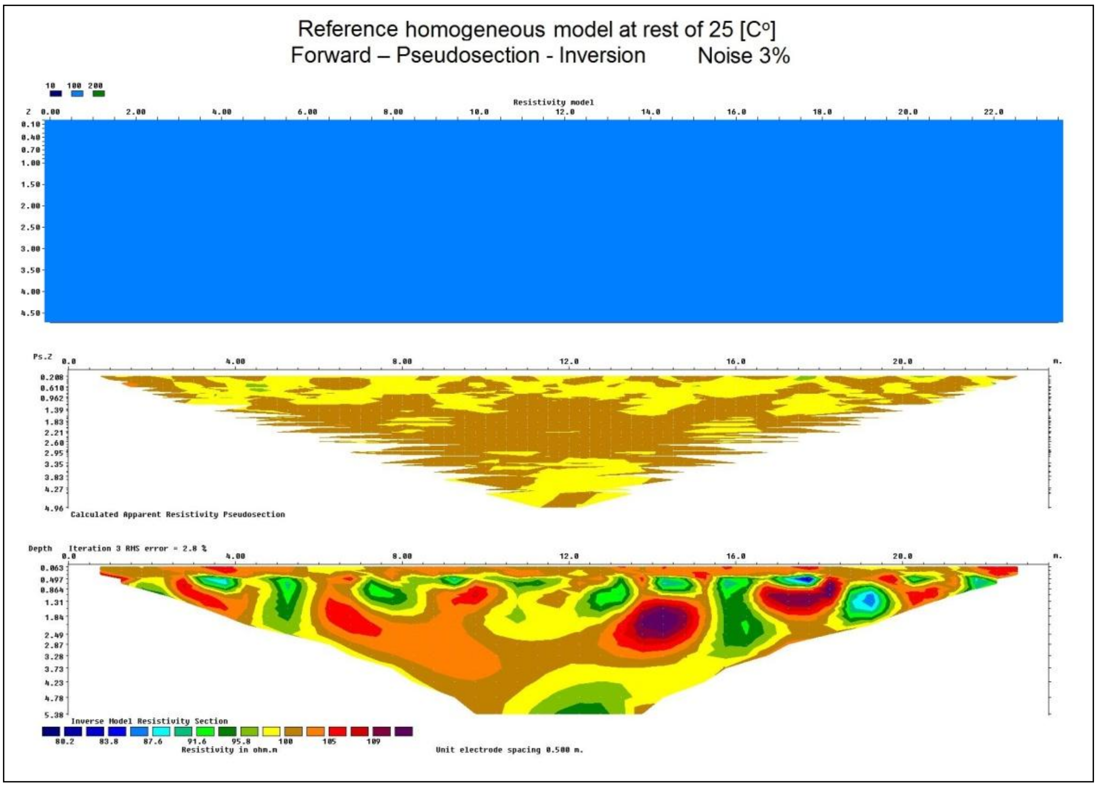

Figure 4-11 Forward, pseudosection and inversion of reference homogeneous model.

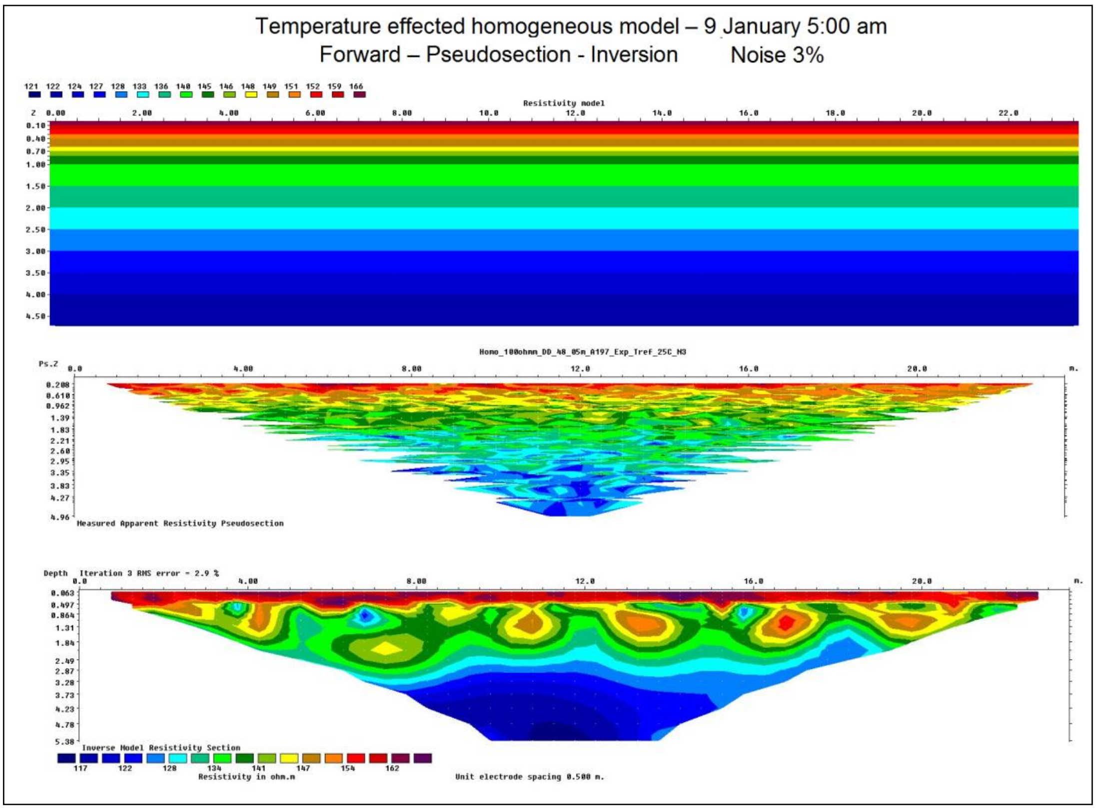

Figure 4-12 Forward, pseudosection and inversion of temperature effected homogeneous model.

4.5 Inhomogeneous formations temperature effect import

The method used for the temperature effect of inhomogeneous models / complex models, is the same as the homogeneous model's method, with the difference that the temperature profiles used, derived from the numerical simulation of heat transition, calculated with Comsol multiphysics software. Figure 4-13 (left) shows the geometry of the reference electrical resistivity model that has three different soils with electrical resistivities at rest conditions of 25 °C. At the right of Figure 4-13, for the same geometry and the corresponding thermal diffusivities, the numerical results of the subsurface temperature variations during the first day of the year, are presented. The values used for this model are shown is Table 4-2 (also appears with light blue colour in Table 5-1).

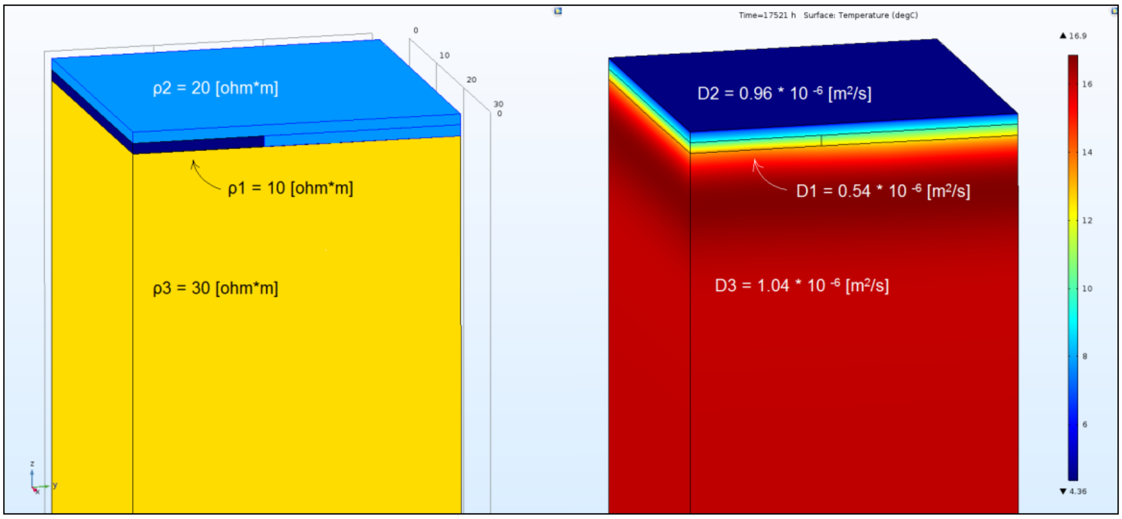

Figure 4-13 Left, reference resistivity model at 25 ºC. Right, numerical simulated temperature distribution used to temperature effect the reference resistivity model.

		China CLAY sat (1)	**Sandy CLAY (2)**	**Fine SAND (3)**
Heat properties from Hamdhan & Clarke (2010)	Water content %	46.2	19.51	24.6
	Thermal conductivity k : W/(m*K)	1.52	2.45	2.75
	Dry Density ρ_d : 10^3 Kg/(m^3)	1.183	1.757	1.613
	Heat capacity per unit Mass cP : 10^3 J/(kg*K)	2.362	1.459	1632
	Thermal diffusivity D : 10^{-6} m^2/s	D1=0.54	D2=0.96	D3=1.04
Electrical resistivity values used	Electrical resistivity at 25 °C ρ : Ωhm-m	ρ1=10	ρ2=20	ρ3=30

Table 4-2 Material properties used for the complex model.

Figure 4-14 (left), shows the 2D geometry of the reference resistivity forward model. In the middle, the temperature profile from the numerical simulation is shown. Right graph of Figure 4-14 presents the temperature effected resistivities, as they have changed due to the influence of the temperature variation.

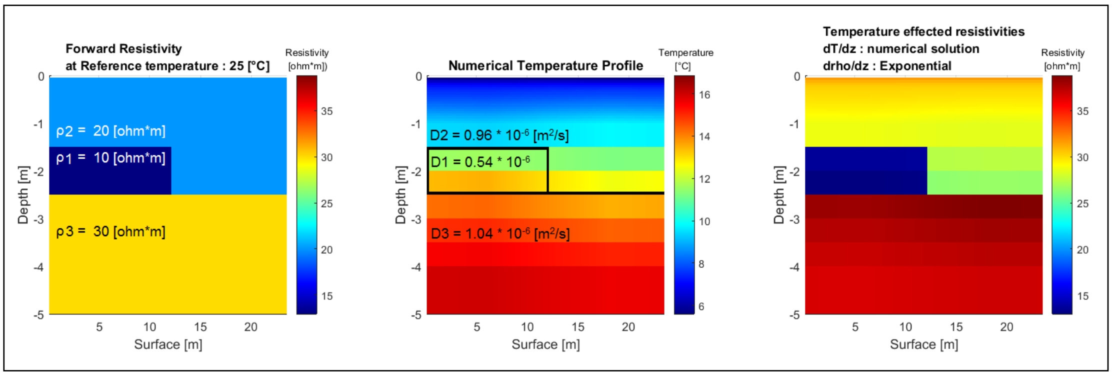

Figure 4-14 Left, reference resistivity model. Middle, simulated temperature distribution. Right, temperature effected model by the temperature distribution.

Figure 4-15, presents the final stage of the inhomogeneous effect where the temperature effected resistivities (left), are divided into 16 classes (middle figure) in order to fit into the res2dmod limitation of 16 electrical resistivity values and create the 2D effected electrical resistivity forward model (right).

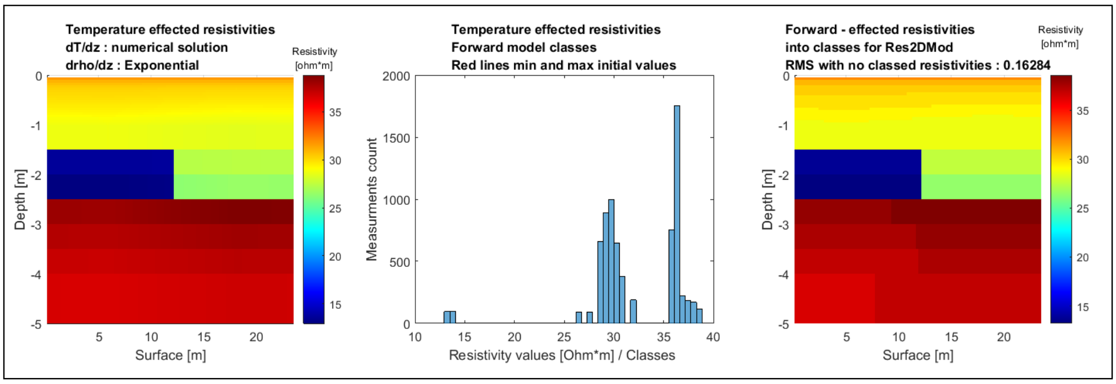

Figure 4-15 Left, calculated resistivity model. Middle, division of resistivity spectrum to 16 classes. Right, the forward model used.

Figure 4-16 presents the forward model, the pseudosection and the inversion results for the inhomogeneous medium at reference temperature of 25 ^{o}C. Figure 4-17 presents the same graphs for the temperature effected model during the first day of the year. Again, both inversion results of reference and temperature effected models, will be used later for the evaluation of the correction.

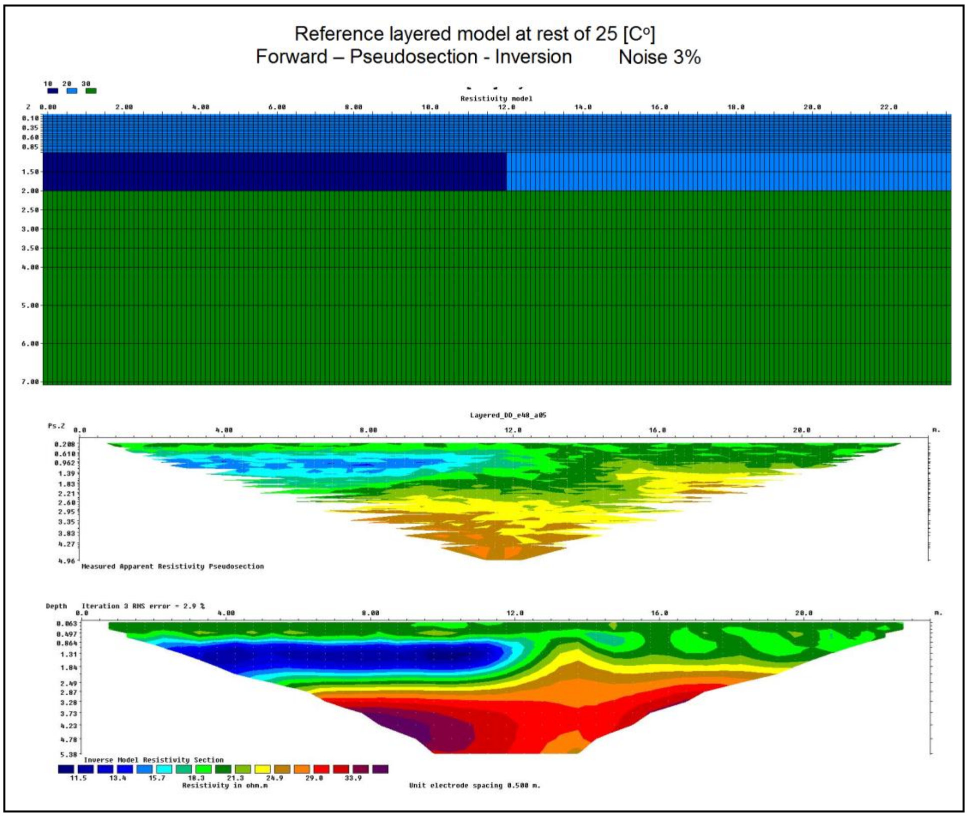

Figure 4-16 Forward, pseudosection and inversion of reference complex model.

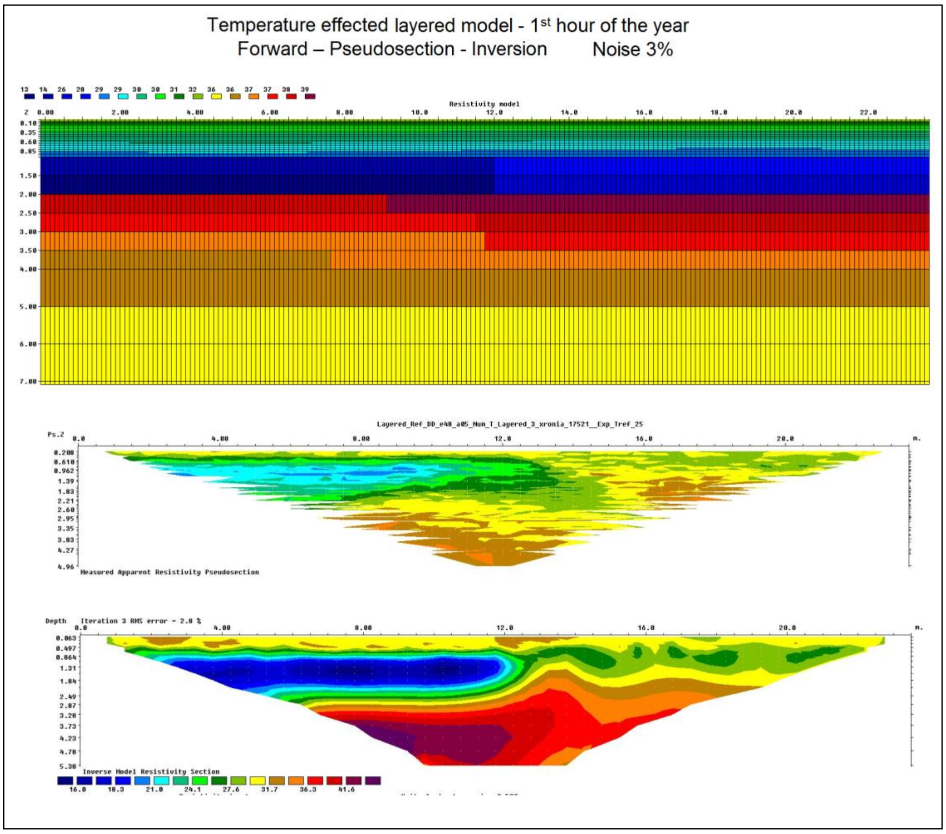

Figure 4-17 Forward, pseudosection and inversion of temperature effected complex model.

4.6 Evaluation of the correction approach

The example below shows the evaluation of the correction method with the correction of a forward homogeneous model of 100 Ohm-m at rest conditions of 25 °C and target depth 5 m, which was temperature effected, inverted and corrected. The results are shown with the form of tomography as well as the linear form, which presents the mean electrical resistivity for each depth. Figure 4-18 could be considered as the evaluation panel of the correction, as it consists of a set of figures that qualify the accuracy of the inversion method and quantifies the correction's validity.

In Figure 4-18 at the upper left graph, temperature effected forward model with no noise imported, is shown. In this forward model, a noise of 3 % was imported and inverted. The inversion results can be seen at the middle left graph. Lower left graph shows the corrected inversion results.

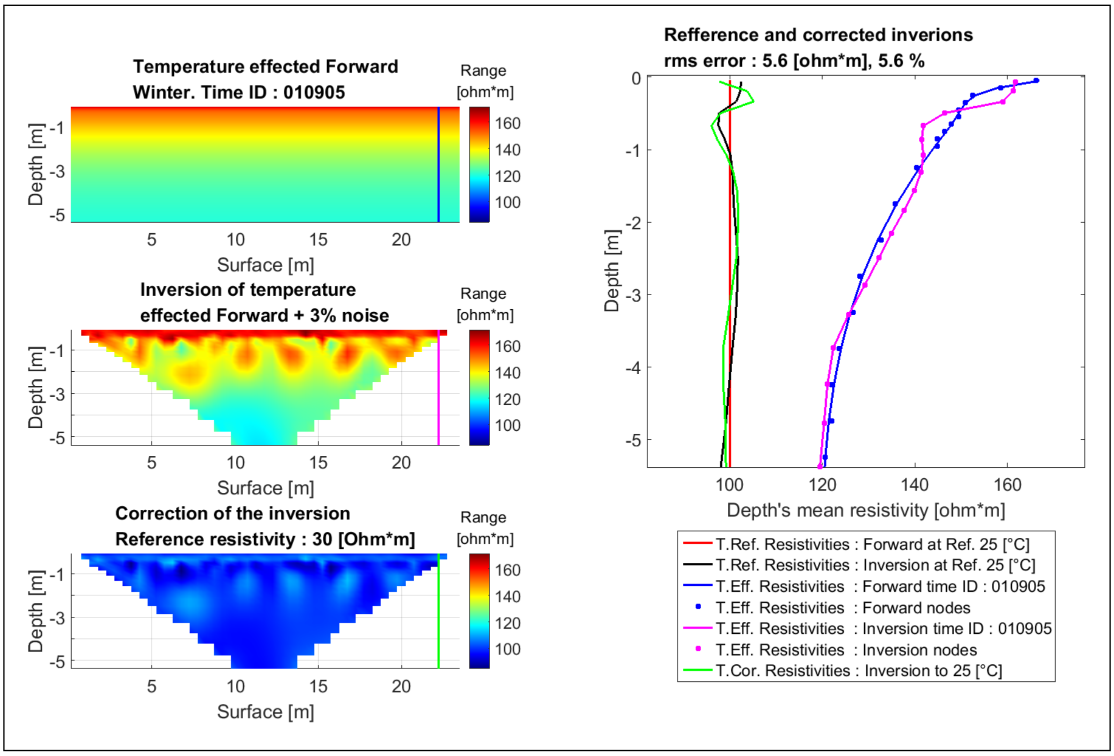

Figure 4-18 Evaluation panel of the correction. Left, forward, inverted and corrected ERTs. Right, resistivity profiles of ERTs with the mean resistivities of each depth.

At the right side of Figure 4-18, the linear graph shows the mean electrical resistivity of each depth, for both the forward and inverse models. The red line shows the reference forward model and the black line shows the inversion of the reference model with 3% noise added. The blue line shows the surface temperature effected forward model and the magenta line presents the temperature effected inverse model for the selected time ID. The green line shows the corrected inversion results of the temperature effected model.

The rms error (unit and percentage), which is presented at the evaluation panel, is calculated between the inversion results of the reference model and the inversion results of the temperature corrected model, using equations (4-2) and (4-3) where n is the number of data.

$$rms\ error_{unit} = \sqrt{\frac{\sum_{i=1}^{n}\left(reference(i) - corrected(i)\right)^2}{n}} \qquad ohm * m \qquad (4\text{-}2)$$

$$rms\ error_{percentage} = 100 * \sqrt{\frac{\sum_{i=1}^{n}\left(\frac{reference(i) - corrected(i)}{reference(i)}\right)^2}{n}} \qquad \% \qquad (4\text{-}3)$$

5. Validation of the results

Using the above methodology, a set of forward models was used to evaluate the efficiency of the ERT, to detect the temperature effect as well as to evaluate the efficiency of the correction algorithm. Firstly, the range of common values of electrical resistivity and thermal diffusivity were tested in order to settle the range of the imposed temperature effect. Then the resolution of the ERT method was tested, in order to examine the accuracy of dipole - dipole array to detect the temperature effect using different array spacing. Dividing the temperature effect into diurnal effect and annual (seasonal) effect, specified by the perturbation depth of each cycle, homogeneous temperature effected forward models of selected days and hours of the year, were used to evaluate the correction method. Finally inhomogeneous temperature effected forward models with high contrast of electrical or heat properties, were used to examine the inversion accuracy and the correction results.

5.1 Physical properties range and profiles.

In order to examine the range of the temperature effected resistivities, the exponential conversion model was used to calculate the temperature effected resistivity values for a 25 °C reference electrical resistivity range of 0-1000 ohm-m and a temperature effect range of 0 – 50 °C. The temperature perturbation depths were calculated assuming typical thermal diffusivity values (i.e. typical rock formations) of the range between 0.12 - 2.12 * 10^{-6} m^2/s. Finally, the percent change of the electrical resistivity with increasing depth and temperature cycle was established on the basis of the adopted temperature profiles.

Temperature effected resistivities range

The exponential conversion model, which was used for the temperature effect and the correction of the forward models of this study, shows that the rate of resistivity change increases at lower temperatures. Figure 5-1 presents the behaviour of this model in the range of different temperatures and resistivities. The white line represents the x axis where the values are the reference resistivities ρ_{ref} for the reference temperature T_{ref} =25 °C of y axis. The coloured background (z axis), shows the resistivities ρ_{mes} as they would appear if they were measured under the different temperatures of y axis.

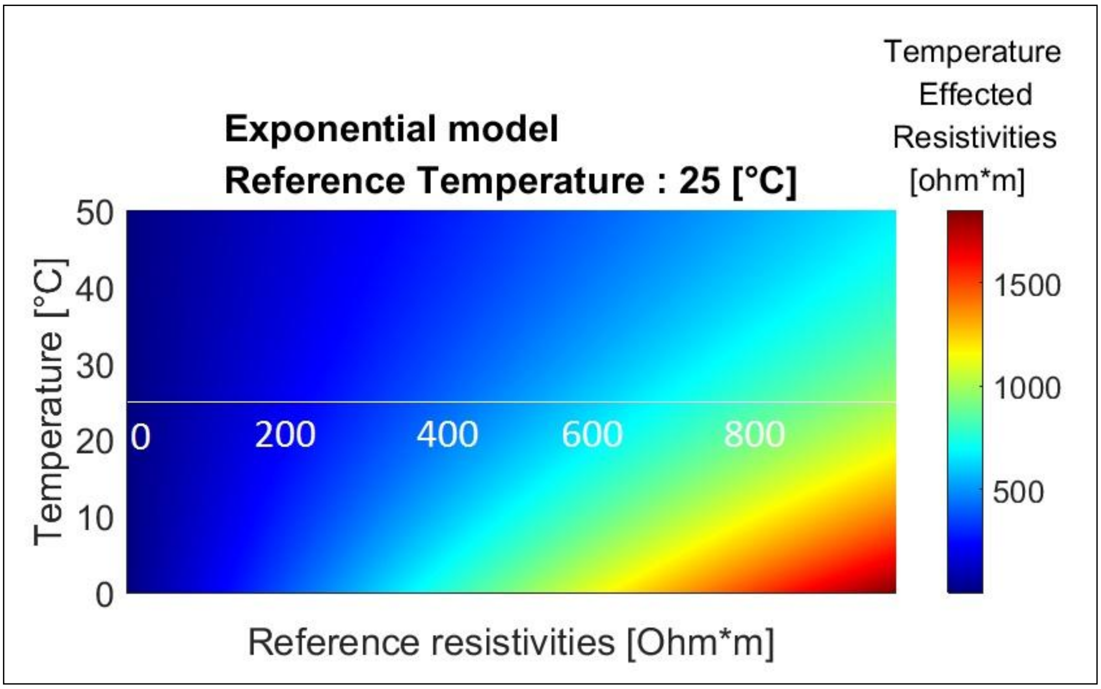

Figure 5-1 Temperature effected resistivity range (z axis) as a result of the application of the exponential conversion model, on reference resistivities of 25 °C (x axis).

Figure 5-2 shows the same information, with the difference that y axis represents the variation of ρ_{mes} for the same range of temperatures between 50 and 0 °C. The white line represents again the reference resistivities of x axis at 25 °C , and it is clear that the most significant changes of electrical resistivity is due to the decrease of temperatures, lower that 25 °C.

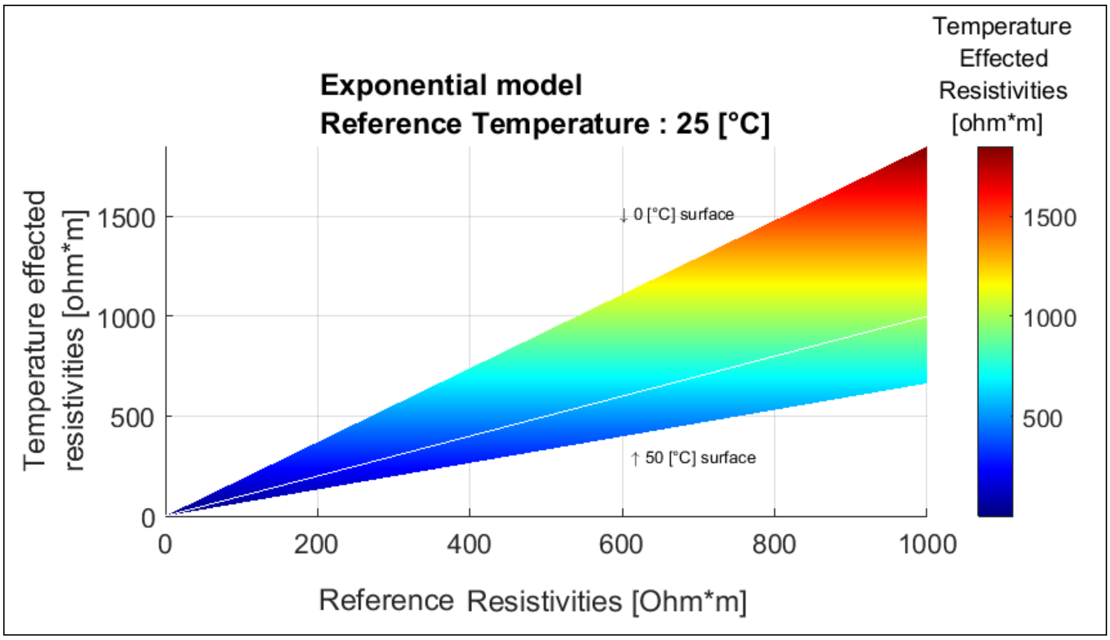

Figure 5-2 Temperature effected resistivity range (z and y axis) as a result of the application of the exponential conversion model, on reference resistivities of 25 °C.

Thermal diffusivity and temperature profile range

In order to evaluate the impact of different thermal diffusivities to the resistivity profiles, the range of 2 thermal diffusivities and 2 electrical resistivities structuring four different forward modelling structures, were evaluated. Considering a homogeneous soil, higher values of thermal diffusivity will increase the perturbation depth of temperature effect. Hamdhan & Clarke (2010) produced a table with the heat properties of various soil types. We modified this table by adding a column describing "**Thermal Diffusivity**" (Table 5-1). The lowest value of thermal diffusivity is for "Fine SAND (dry)" sample (black background colour in table) with value $0.12 * 10^{-6}$ m^2/s

and the highest value is for “Grey slightly silty sandy GRAVEL” sample (orange background colour) with value 2.12 * 10^{-6} m^2/s .

Soil Type	Water Content %	Bulk Density Kg/m^3	Dry Density Kg/m^3	Specific Heat Capacity J/(kg*K)	Thermal Conductivity W/(m*K)	Thermal Diffusivity 10^{-6} m^2/s
Fine SAND (dry)	0	1600	1600	800	0.15	0.12
Course SAND (dry)	0	1800	1800	800	0.25	0.17
Medium SAND (dry)	0	1700	1700	800	0.27	0.20
China CLAY (D) (dry)	0	1390	1390	800	0.25	0.22
China CLAY (D) (sat.)	46.2	1730	1183	2362	1.52	0.54
Sandy CLAY	26.5	1890	1494	1696	1.61	0.64
Homogeneous clay model			**1300**	**1710**	**1.88**	**0.84**
Sandy CLAY	19.5	2100	1757	1459	2.45	0.96
Fine SAND (sat.)	24.6	2010	1613	1632	2.75	1.04
Soft grey fine sandy CLAY	41.4	1741	1231	2200	3.03	1.12
Grey limestone (very hard)	0.1	2690	2687	803	2.54	1.18
Very soft grey fine sandy CLAY	46.2	1711	1170	2362	3.51	1.27
Medium SAND (sat.)	20.2	2080	1730	1483	3.34	1.30
Stiff grey brown sandy gravelly CLAY	9	2352	2158	1104	3.2	1.34
Stiff dark grey sandy gravelly CLAY	9.6	2369	2161	1125	3.28	1.35
Soft dark grey sandy gravely CLAY	28.5	1912	1488	1764	3.57	1.36
Course SAND (sat.)	20.2	2080	1730	1483	3.72	1.45
Soft grey fine sandy CLAY	54.6	1650	1067	2646	4.2	1.49
Stiff dark grey sandy gravely CLAY	10.1	2299	2088	1141	3.69	1.55
Dark grey clayey fine sand/silt	28	1848	1444	1747	4.26	1.69
Made ground (Silty gravely sand)	13.9	2182	1916	1270	5.03	2.07
Grey slightly silty sandy GRAVEL	11.1	1983	1785	1175	4.44	2.12

Table 5-1 Thermal properties of various formations (after Hamdhan & Clarke,2010).

The lowest and highest values of thermal diffusivity were used to calculate the range of temperatures that can be observed at each depth during an annual cycle. Figure 5-3 A, presents the temperature profile range for each depth, for the sample of “Fine SAND (dry)” (black line) with the lowest value of thermal diffusivity. Also the temperature profile range for the sample of “Grey slightly silty sandy GRAVEL” with the highest value of thermal diffusivity is plotted (orange line of Figure 5-3 A), for which the perturbation depth is greater. With teal colored line, the thermal diffusivity of the homogeneous clay model, that have been used for the homogeneous models so far, is also plotted.

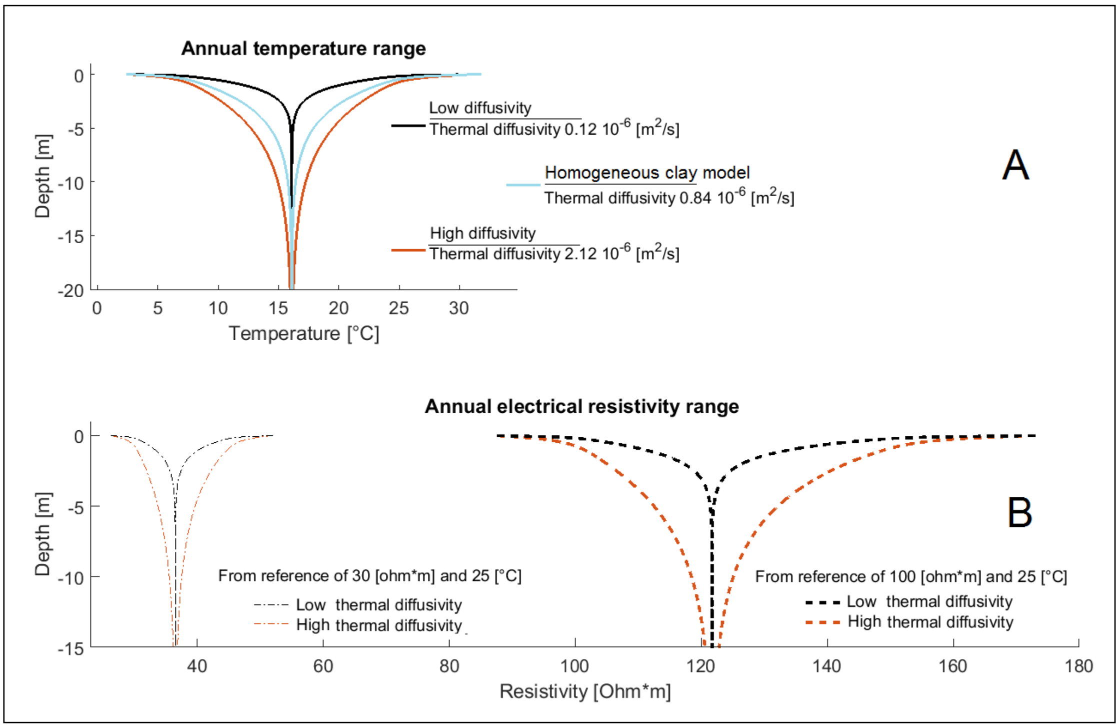

Figure 5-3 A, Annual subsurface temperature range for 3 typical diffusivity values. B, Annual subsurface resistivity range for reference resistivity 30 and 100 0hm-m at 25 °C, in conjunction with 2 typical thermal diffusivity values.

Electrical resistivity profile range

Combining the two temperature profiles (produced by the lowest and the highest diffusivity Figure 5-3 A) with two cases of 25 °C reference electrical resistivities (30 and 100 ohm-m), four homogeneous models can be created. In Figure 5-3 B (left), the **thin dash&dot lines** represent the electrical resistivity profiles of a 30 ohm-m homogeneous medium for the cases of low thermal diffusivity (black colour) and high thermal diffusivity (orange colour).

In Figure 5-3 B right, the **bold dashed lines** represent the electrical resistivity profiles for a medium of 100 ohm-m for the two thermal diffusivity cases, one with low thermal diffusivity (black colour) and one with high thermal diffusivity (orange colour). In Figure 5-3 B, it can be observed that the electrical resistivity amplitudes, caused by the low temperatures of winter (> 122 ohm-m), are greater than the electrical resistivity amplitudes caused by the high temperatures of summer (< 122 ohm-m).

The percentage of the change of electrical resistivity with respect to the 16.1 °C mean annual resistivity value, for each depth of the lowest (black colour) and the highest (orange colour) thermal diffusivity of Table 5-1, are depicted in Figure 5-4. The depths of the resistivity horizons, that the change of resistivity amplitude becomes smaller than 1%, 3% and 5%, of the reference resistivity at 16.1 °C, are presented with the horizontal lines in the same figure and also in the figure's table. Dashed lines present the resistivity amplitudes caused by the transition of heat gained at the hottest day of the year, while continuous lines present the resistivity amplitudes caused by the transition of heat loss during the coldest days of the year. Winter's lower temperatures result in higher resistivity amplitudes. Concluding, for this range of thermal diffusivities and a Mediterranean climate, the 3% resistivity change horizon cannot be found at depths greater than -9.6 m.

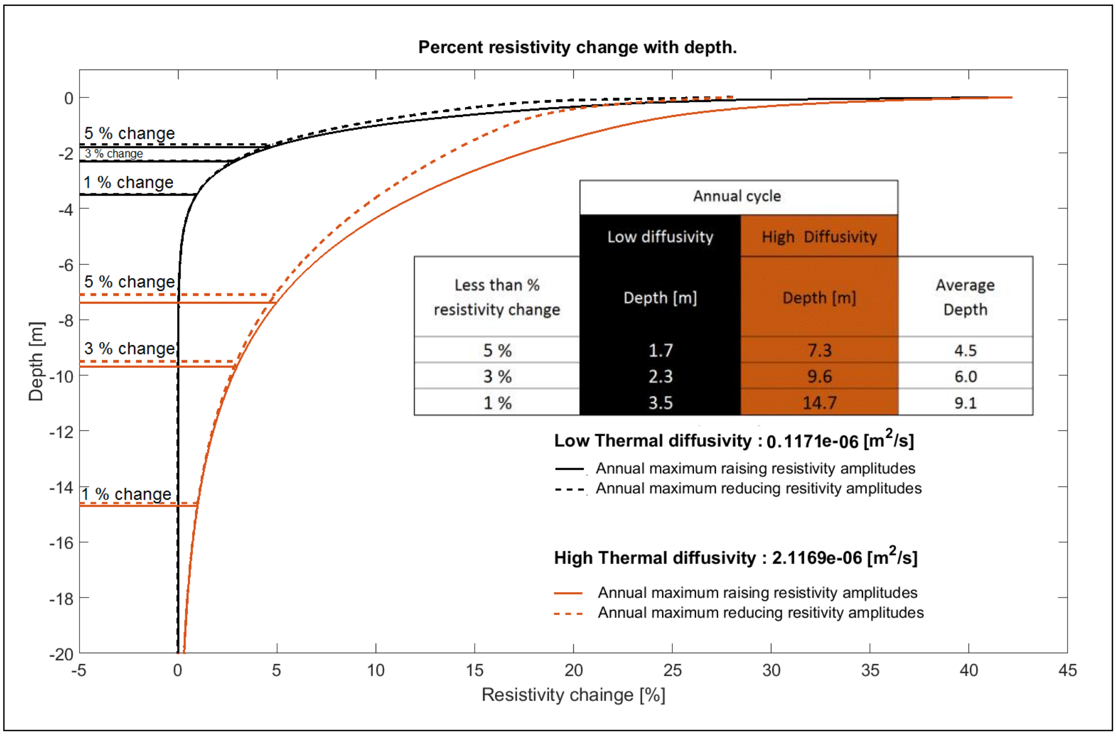

Figure 5-4 Annual subsurface resistivity percent change with depth.

Figure 5-5, focus on the first -1 m depth from the surface and presents the same percentage of resistivity change, with respect to the 16.1 °C mean annual resistivity value, for the two cases of thermal diffusivity during the annual cycle. The two thermal conductivities start with the same temperature effect on the surface resistivities, while at larger depths, the high thermal conductivity medium causes greater percentage of change to the electrical resistivity amplitudes than the low diffusivity medium. The amplitudes of electrical resistivity variations caused by winter's heat loss transition, are also higher than the resistivity variations caused by summer's heat gain transition.

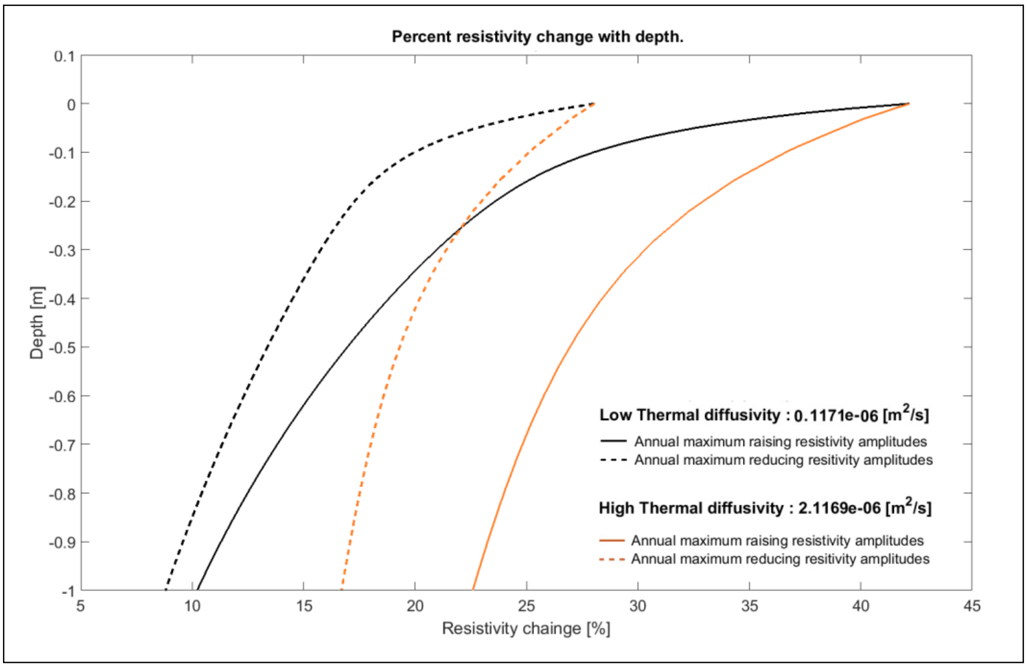

Figure 5-5 Annual subsurface resistivity percent change up to -1 m depth.

In Figure 5-5 the percentage of change of the mean annual reference resistivity at the first -1 m is also shown. In Figures 5-6 and 5-7 the percentage change of the diurnal mean resistivity of each depth during a diurnal cycle of winter and summer for the first -1 m from the surface is shown. Figure 5-6 presents the maximum depths of the 5 %, 3% and 1% resistivity change horizons, during the coldest diurnal cycle of the winter. Figure 5-7 presents the same resistivity change horizons for the hottest diurnal cycle of the summer.

Concluding, both in summer and in winter, the depth of 3 % diurnal resistivity change horizon, for the range of thermal diffusivities of Table 5-1, is found to be -0.33 m and less. Also, the change of perturbation depths between winter and summer diurnal cycles is less than 0.05 m.

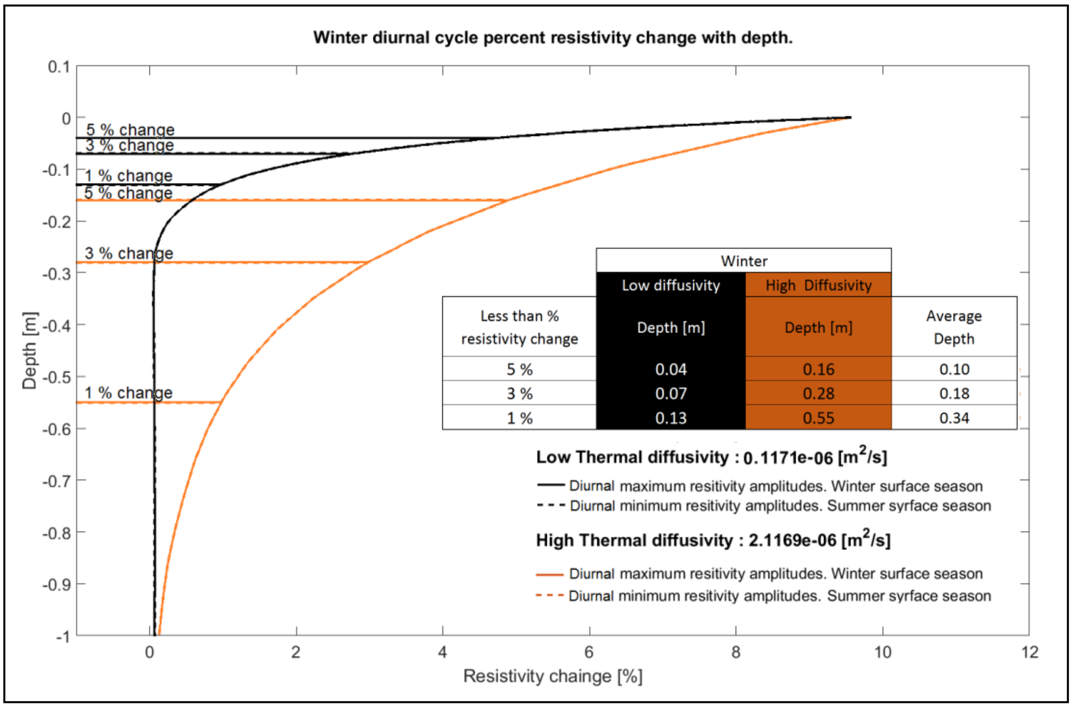

Figure 5-6 Diurnal subsurface resistivity percent change, during winter season.

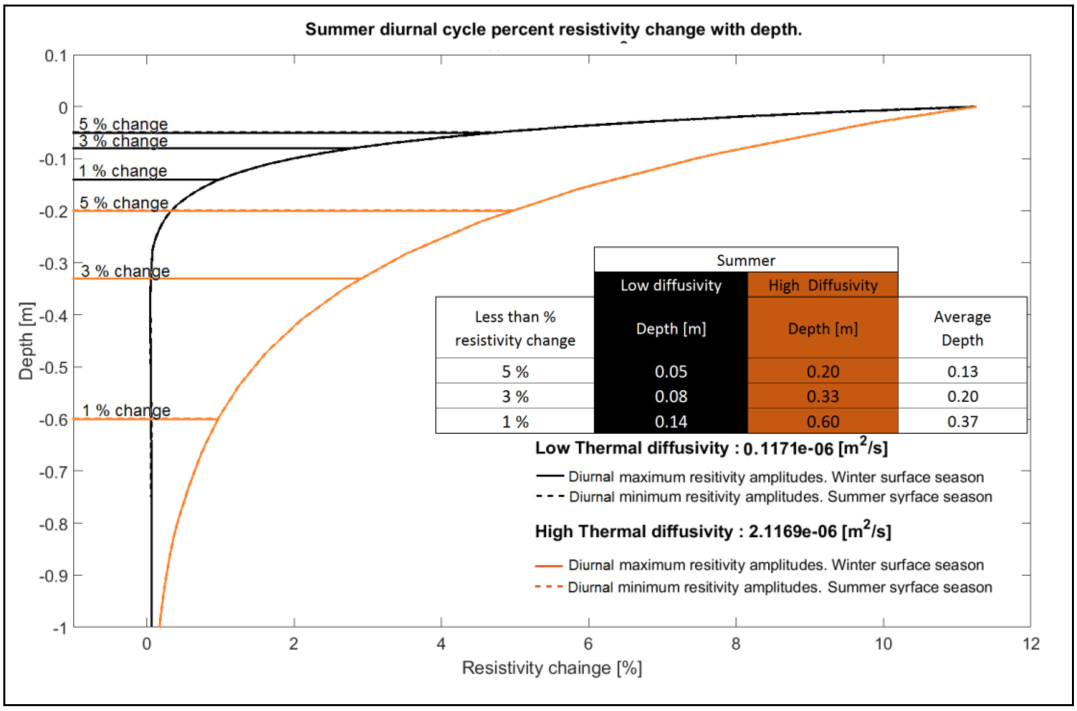

Figure 5-7 Diurnal subsurface resistivity percent change, during summer season.

Figure 5-8 presents the combined time-lapse resistivity profiles of the first 1 m for the heat values of the homogeneous clay model with 30 ohm-m reference resistivity, during a winter's diurnal cycle (left) and a summer's diurnal cycle (right). Figure 5-9 presents the 24 hour resistivity time-lapse up to 10 m depth.

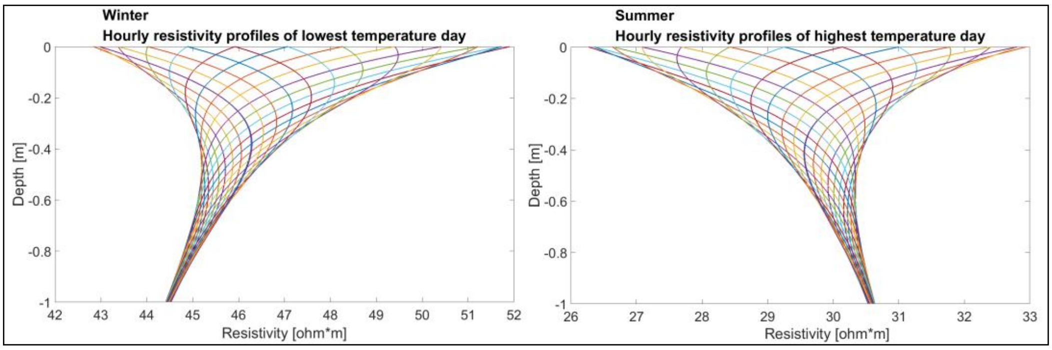

Figure 5-8 Hourly resistivity profiles during a diurnal cycle, up to 1 m.

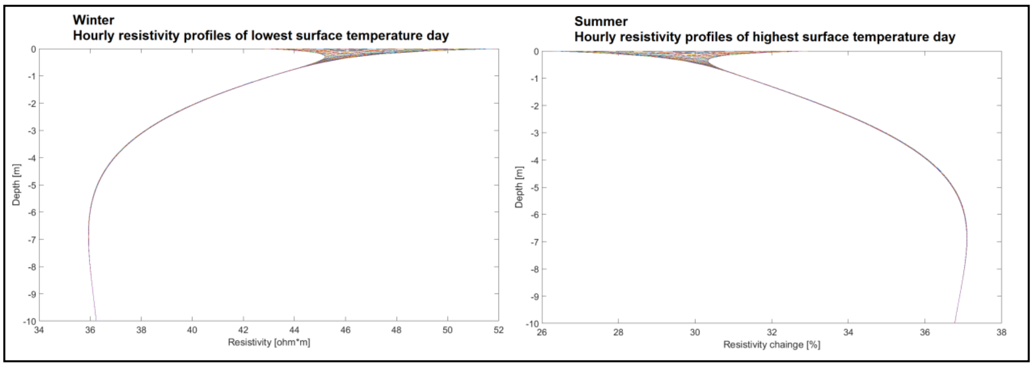

Figure 5-9 Hourly resistivity profiles during a diurnal cycle, up to 10 m.

From the aspect of resistivity-contour lines where the z axis is the depth axis in Figure 5-10, starting from 0 m and continuing with -0.1 m depth step up to -15 m, Figure 5-10 shows for a 24 hour period, the very low frequencies (seasonally oscillating) electrical resistivity horizons (that are close to steady state condition), act as chords where the diurnal temperature oscillation cycle effect only the 1st meter.

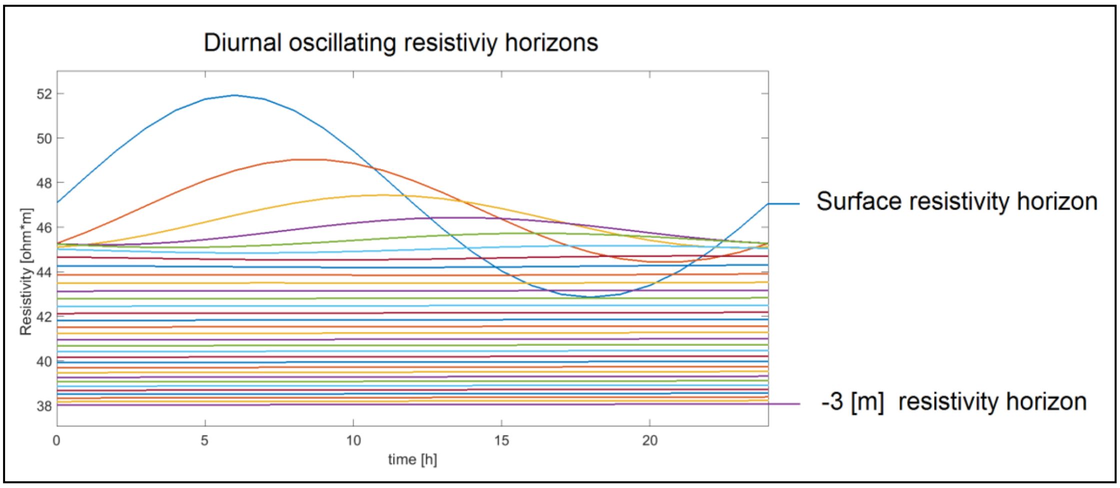

Figure 5-10 Diurnally oscillating resistivity horizons for 0 to 3m depth of a homogeneous medium.

5.2 Correction implementation and ERT resolution

In order to study the sensitivity of the ERT method to temperature changes and in order to study and correct the temperature effect we generated synthetic models. Initially a homogenous model was used with the electric and heat values of chapter 2.1, presenting a clay medium with reference electrical conductivity 30 ohm-m at temperature of 25 °C and thermal diffusivity equal to 0.84 * 10^{-6} m^2/s. In Figure 5-11 the teal colour shows the percentage change of electrical resistivity with depth for this clay medium in contrast to the thermal diffusivity range discussed before. For this model and during an annual surface temperature cycle that consist of the annual oscillation, the diurnal oscillation and the seasonal variation of diurnal's amplitude, the resistivity horizon of 5% change is found at depths closer to surface than -4.5 m. The 3% change resistivity horizon is found at depths closer than -6.1 m and the 1% change resistivity horizon is found at depths closer than -9.3 m.

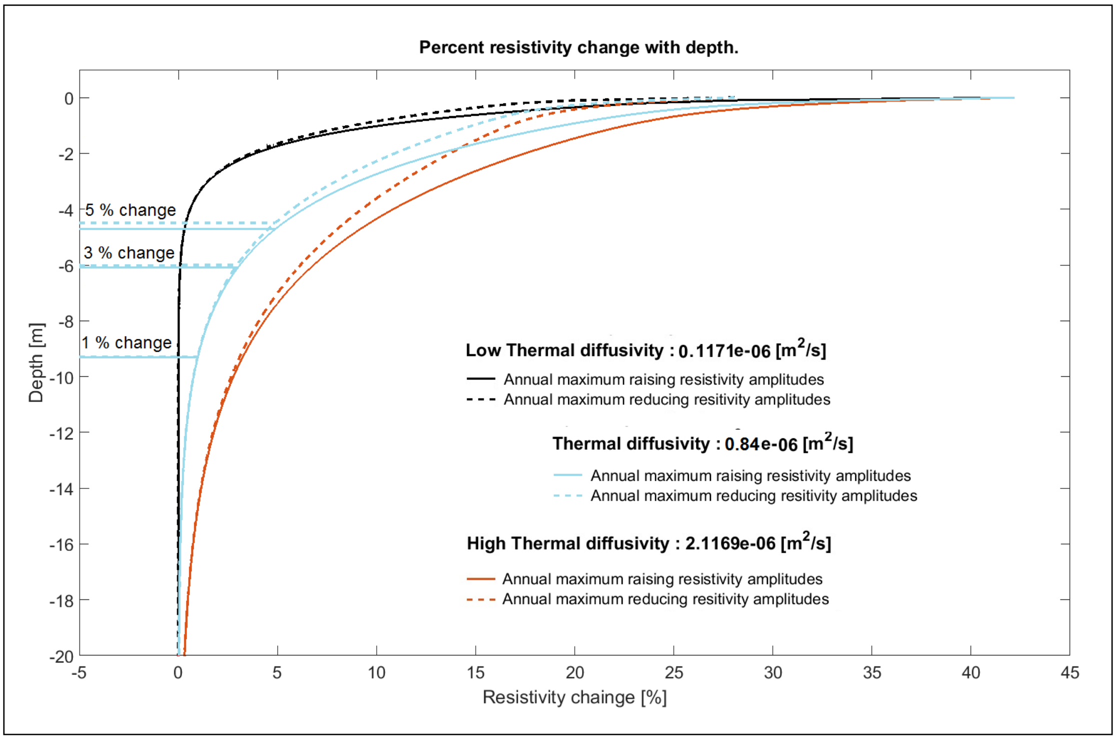

Figure 5-11 Annual subsurface resistivity percent change for a soil with medium range thermal diffusivity.

Figure 5-12, depicts the correction for a forward survey conducted during the 9th day of January (coldest surface temperature of the year), using a Dipole-Dipole array with 48 electrodes and 1.5 m spacing. The blue colored line presents the temperature effected forward model, where the electrical resistivity profile has been influenced by the temperature variations. The forward model suggests that the resistivity horizons of 5 %, 3 % and 1 % change are found between 3 and 4 m depth.

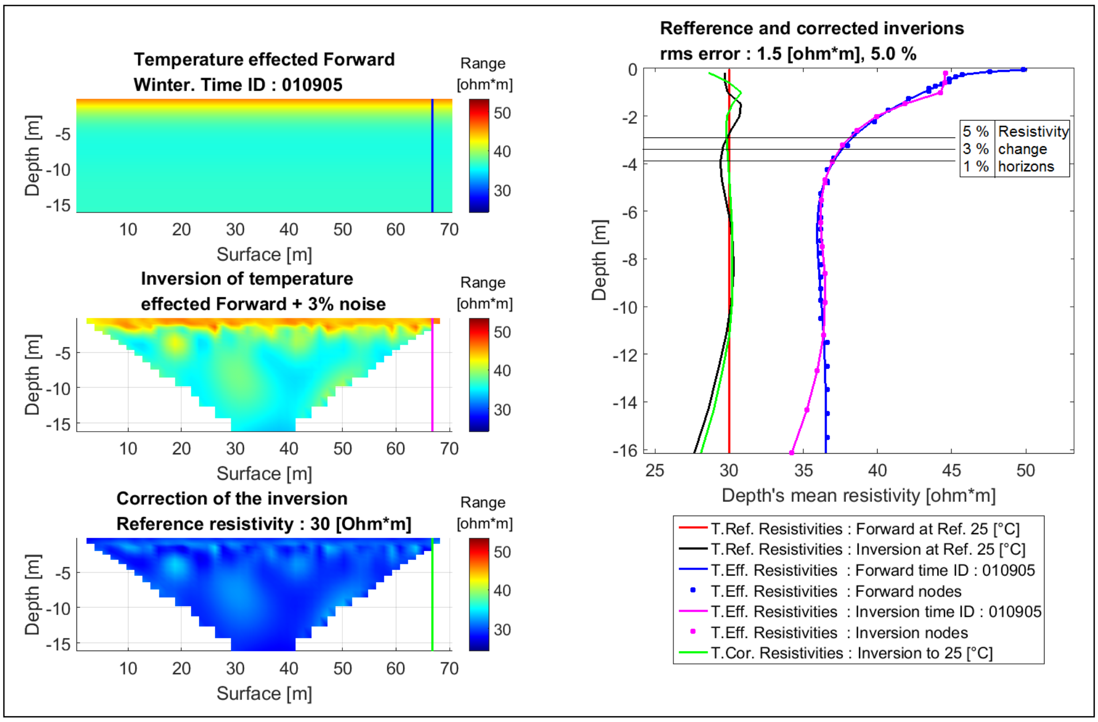

Figure 5-12 Correction of the inversion results for the case of a 48 electrode array with 1.5 m spacing.

The inversion results of the forward model are presented with magenta colored line at the graph of Figure 5-12. The green line of the same figure presents the corrected inversion results of the temperature effected forward model. The red line is the forward reference model at 25 °C and the black line presents the inversion of the reference model. The rms error is calculated between the inversion results of the reference model (black line) and the corrected inversion results of the temperature effected forward model (green line).

Figure 5-12 provides an overview of the annual perturbation depth of the surface temperature effect, which can be recorded by the ERT method. For the particular survey date and model the perturbation depth of the surface temperature effect can be identified by the ERT method at depths up to 4 and 5 m.

When lower resolution ERT data sets are used (with 24 electrodes, 5m spacing) the inversion results tend to underestimate the temperature effect as shown in Figure 5-13 (left). Accordingly, for even larger spacings (i.e. spacing equal to 10 m) the resolution is so low that the temperature effect is not detected by the inversion results, and as a result the temperature correction is inapplicable (Figure 5-13, right).

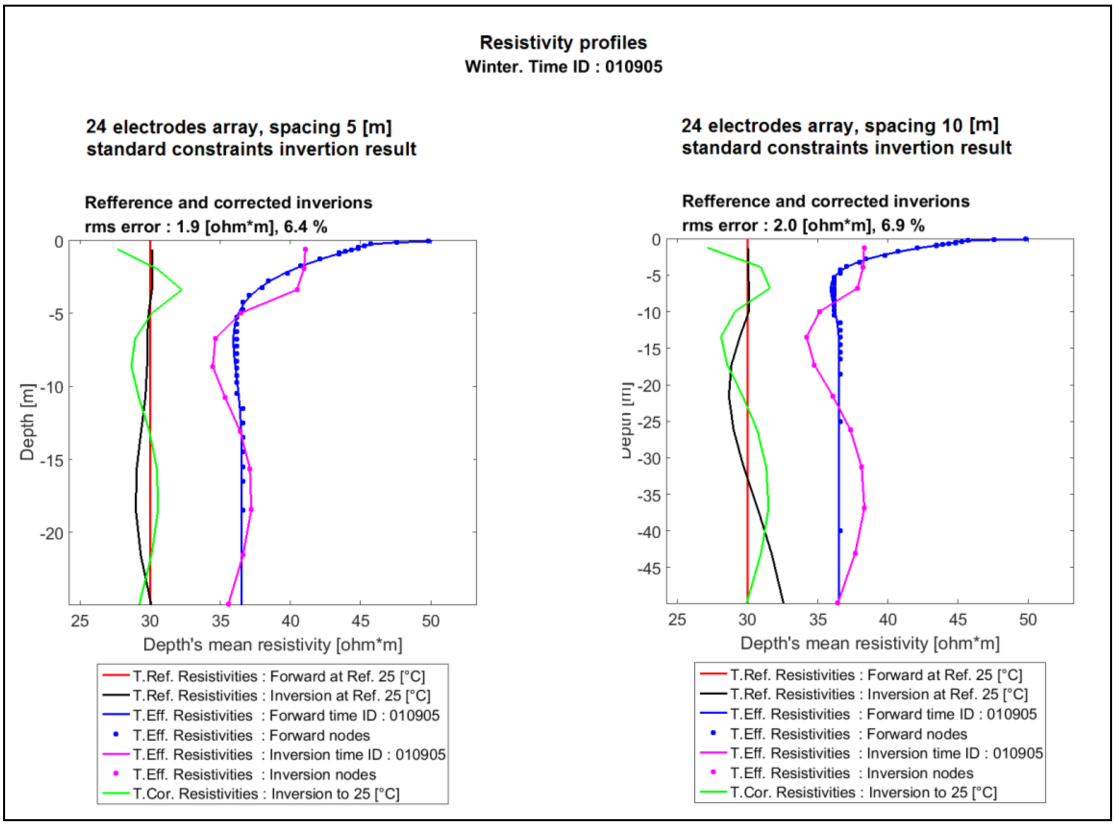

Figure 5-13 Correction of the inversion results for the case of a 24 electrode array with 5 and 10m spacing.

Additionally, two further tests were conducted with smaller electrode spacings. Focusing on the first -5 m from the surface with the resolution offered by two different dipole dipole array sets, one with 24 electrodes and 1 m inter electrode spacing and the other with 48 electrodes and 0.5 m spacing, the temperature effect is well recorded by the inversion results for both array sets. The better resolution offered by the array with 48 electrodes, provides greater sensitivity of the inversion process to the temperature effect. As a result, for the same calculated temperature profile, the correction provides lower rms error for the temperature corrected inversion results of the high resolution array. Figure 5-14 presents the inversion and the correction results of those arrays with rms errors 6.3% for the 24 electrode set and 4.6% for the 48 electrode set respectively.

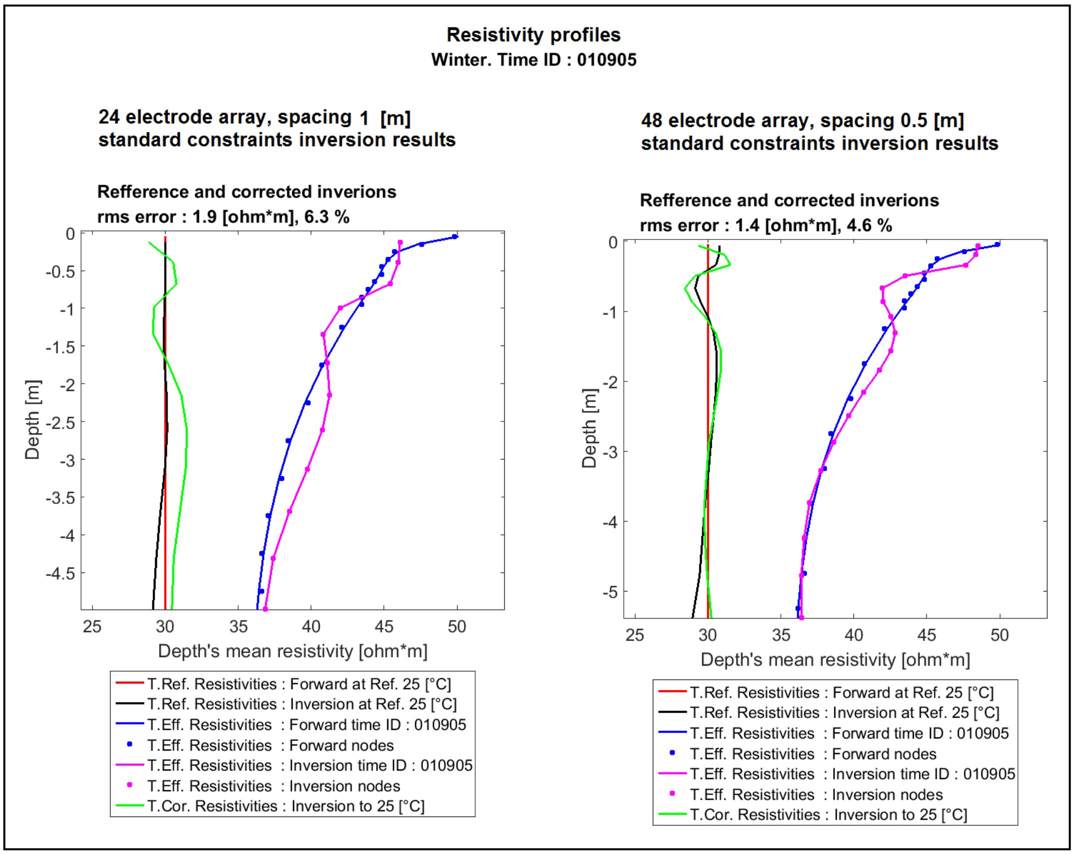

Figure 5-14 Correction of the inversion results for the case of a 24 electrode array, 1m spacing (left) and 48 electrodes, 0.5m spacing (right).

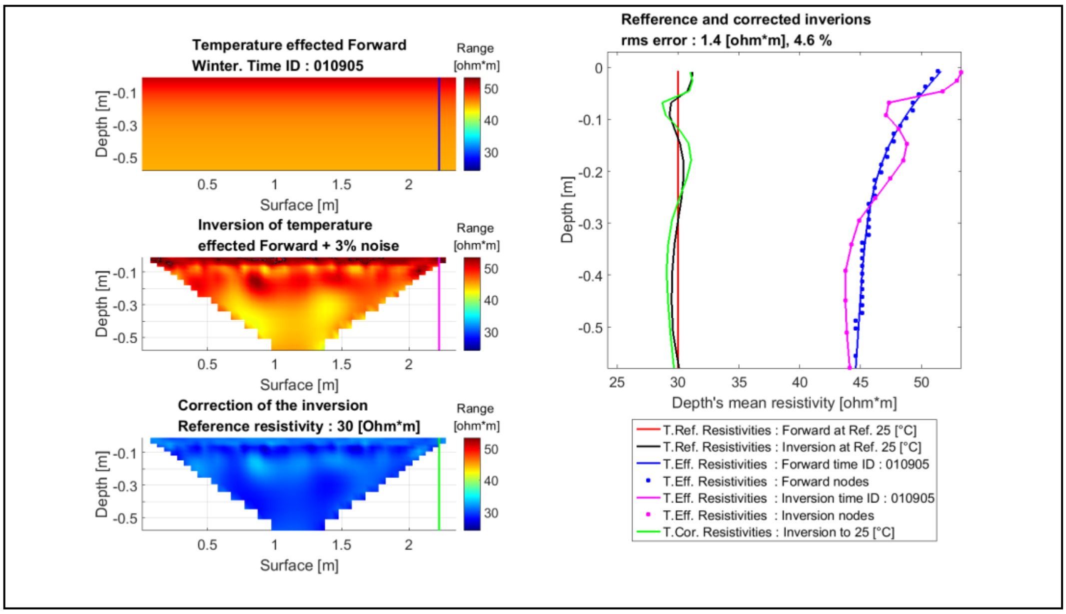

Figure 5-15 Correction of the inversion results for the homogeneous model (48 electrode array with 0.05 m electrode spacing).

Focusing at depths affected by the diurnal surface temperature oscillation i.e. approximately 0.3m, the inversion process will detect the resistivity changes at the diurnal oscillating resistivity horizons only when extremely small electrode spacing

(< 0.1 m) is used for the acquisition of ERT measurements. The correction of these profiles is being processed with an rms error close to 4.6 % as it can be seen in Figure 5-15 for the case of 48 electrode array with 0.05m spacing.

In this section, the efficiency of the correction method relative to the depth dimension, showed that for inter electrode spacing smaller than 7 [m], the ERT method is highly sensitive to the surface temperature effect that can be corrected. In the following, the efficiency of ERT to detect and correct the time depended changes of temperature effect during an annual cycle, focusing separately on the seasonal and the diurnal oscillating resistivity horizons and their corresponding perturbation depths, will be examined.

5.3 Annual surface temperature effect

The temperature effect and the corresponding perturbation depth caused by the surface temperature oscillation during an annual cycle can be considered as the annual (seasonal) effect. Using the values of chapter 2.1 for the homogeneous clay medium at reference temperature 25 °C, the inversion results of one temperature effected forward model, for each season of the year, was corrected for the temperature variations. The electric resistivity tomographies have been carried out based on a Dipole – Dipole array scheme with 48 electrodes and 1.5 m spacing.

Figure 5-16 presents four temperature profiles of the dates: 9 January during the lowest surface temperatures of the year, 10 July during the highest surface temperatures of the year and two more days close the equinoxes. Figure 5-17 presents the corresponding resistivity profiles for these dates. These profiles were used to produce the temperature effected forward models and also to test the efficiency of the array to detect the temperature effect as well as to evaluate the efficiency of the correction algorithm.

Figure 5-18, Figure 5-19, Figure 5-20 and Figure 5-21 show the inversion and the correction results for each model respectively. As a result of these models, the inversions can detect the seasonal effect up to depths related to the percentage resistivity change of 3%. The Rms errors that are calculated between the reference and the corrected inversion results, are close to 5.2%. The inversion results of these arrays are insensitive to the diurnal temperature oscillations due to the reduced resolving ability of the measurements at the depths (i.e. around 0.3m) effected by the diurnal temperature changes.

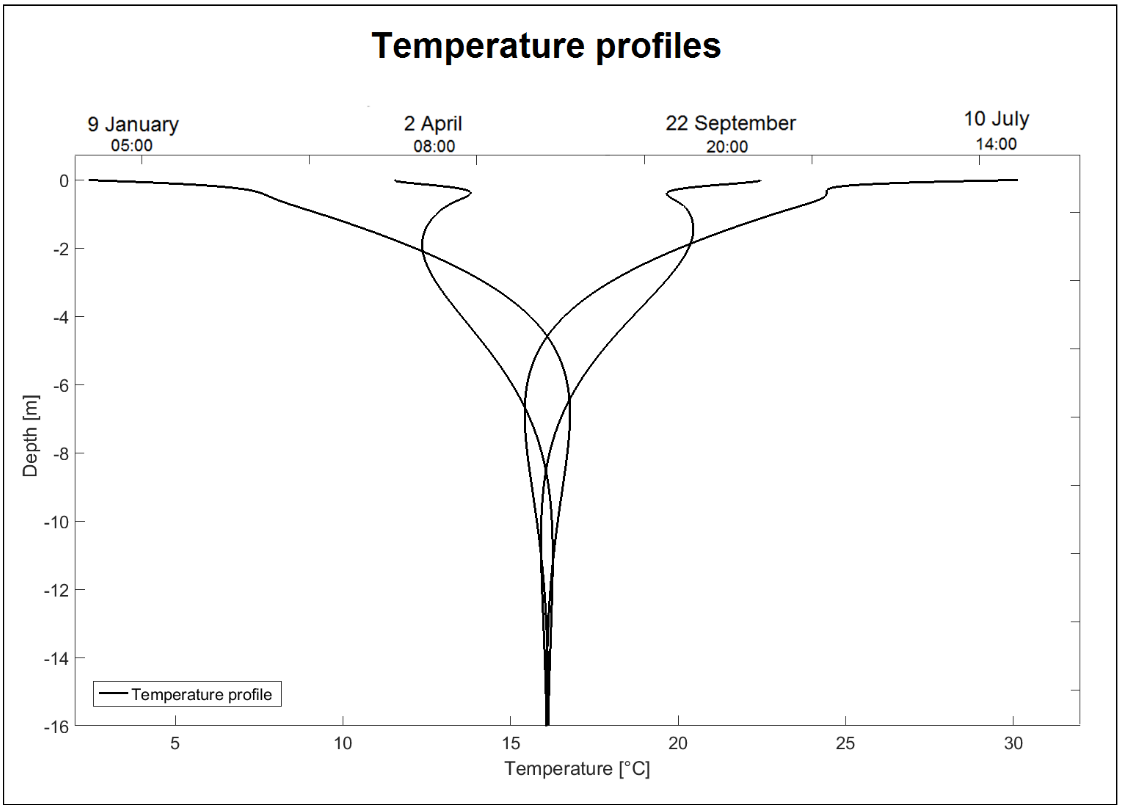

Figure 5-16 Temperature profiles for the four tested dates during an annual cycle.

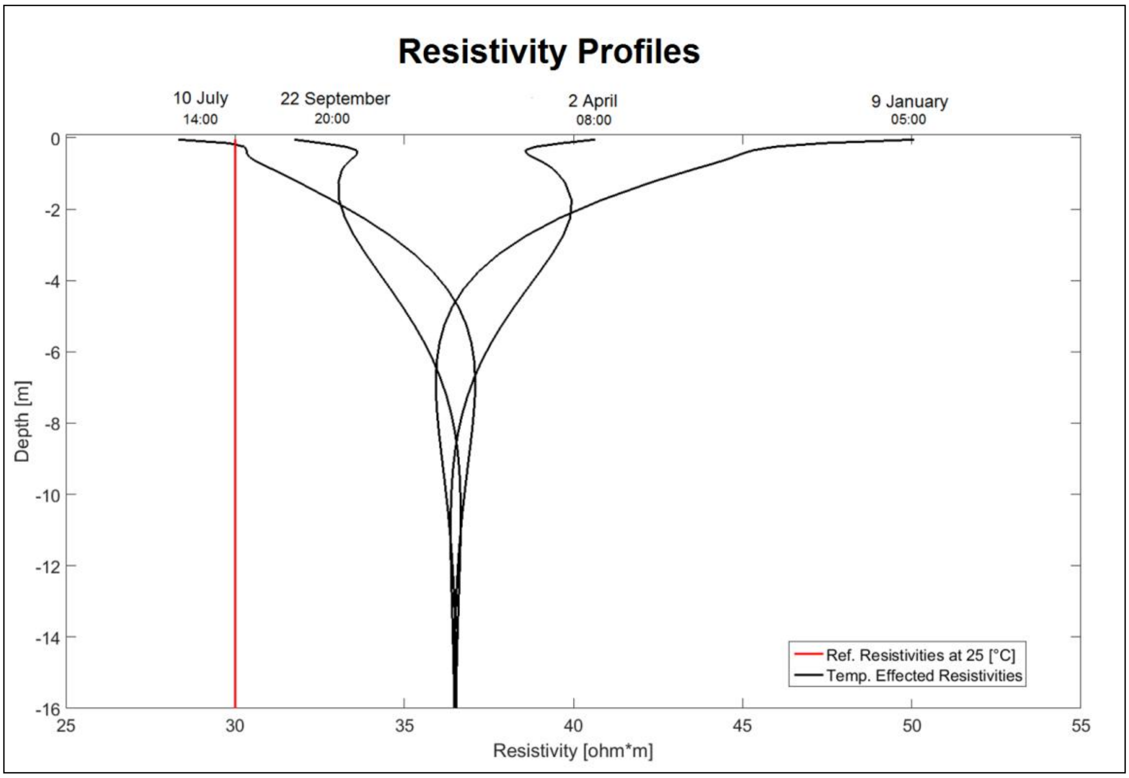

Figure 5-17 Temperature effected resistivity profiles for the four tested dates.

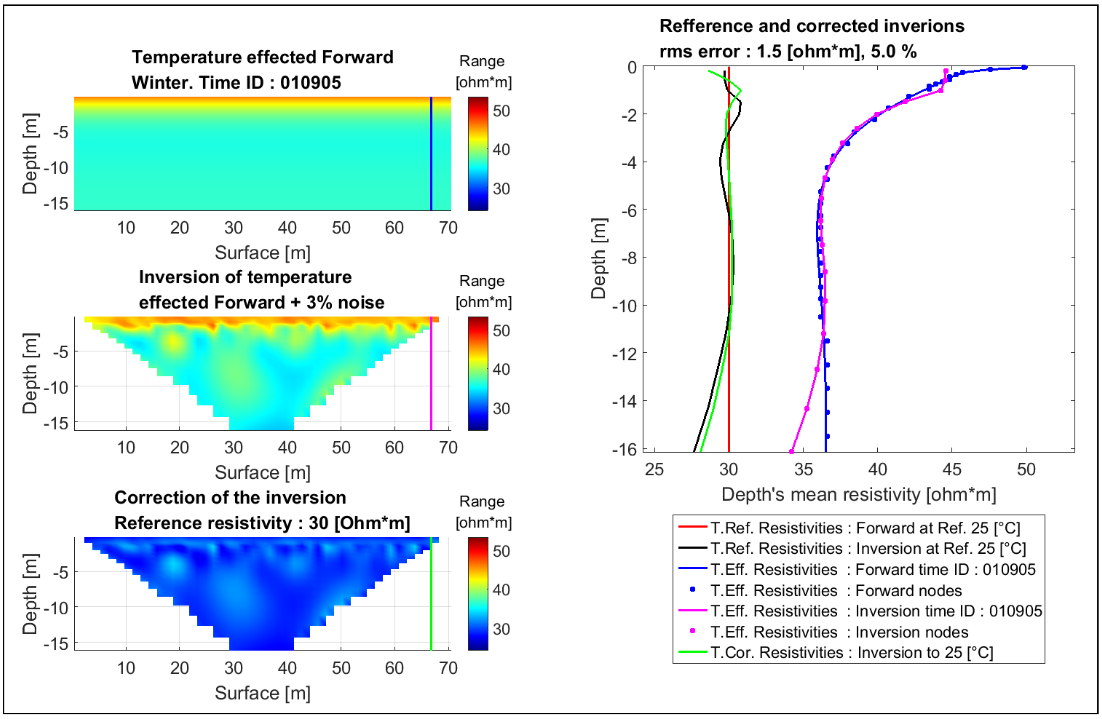

Figure 5-18 Correction of the inversion results for the data collected at January.

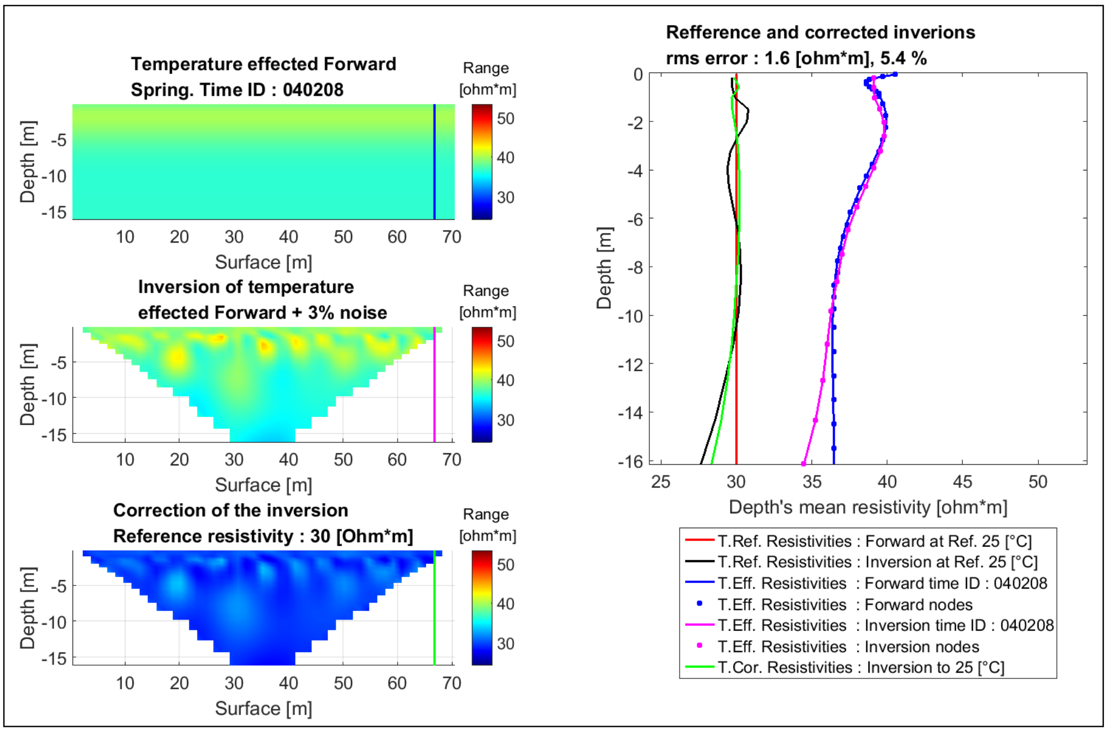

Figure 5-19 Correction of the inversion results for the data collected at April.

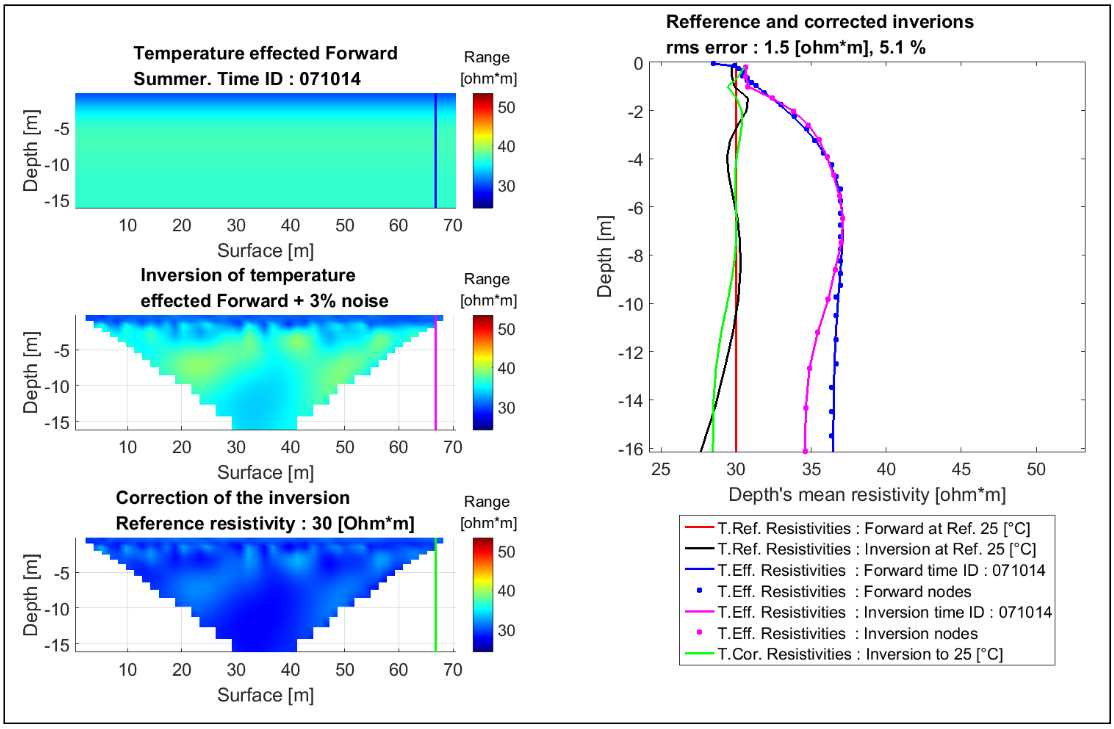

Figure 5-20 Correction of the inversion results for the data collected at June.

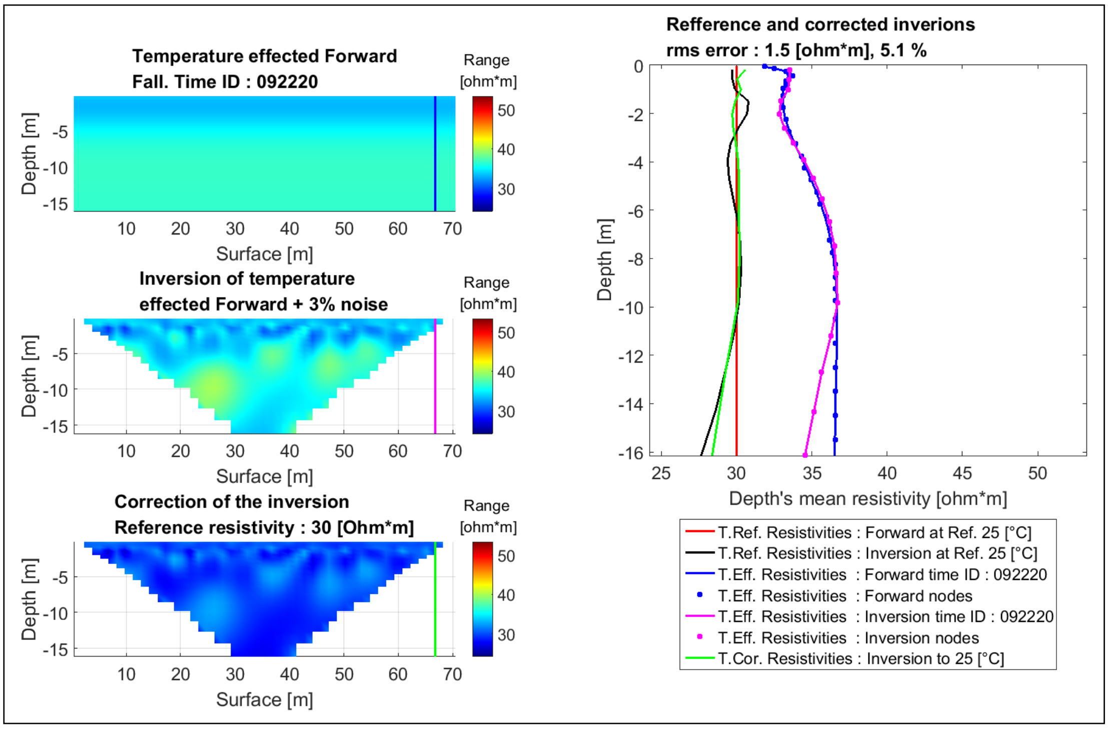

Figure 5-21 Correction of the inversion results for the data collected at September.

5.4 Diurnal temperature effect

We also performed tests to study the diurnal effect i.e. the temperature effect produced by the diurnal surface temperature oscillation cycle. The changes to the resistivity profile due to the diurnal oscillation is more than 1% up to the depths of -0.5m while below that depth the amplitude of diurnal resistivity fluctuation becomes insignificant. This is clearly shown in Figure 5-22 and Figure 5-23 which present the temperature and resistivity profiles up to 1.5 m depth, for three different (low, medium and high) thermal diffusivity values.

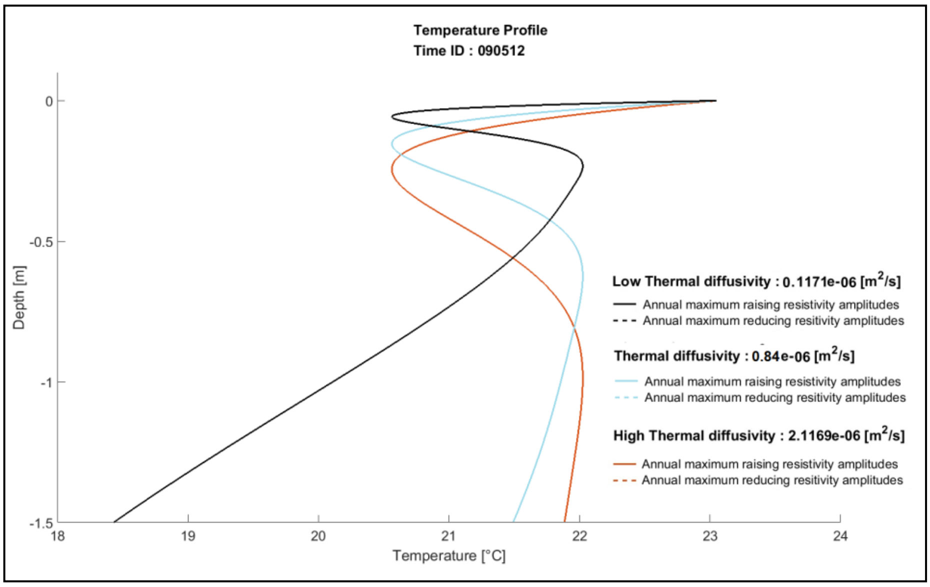

Figure 5-22 Diurnal temperature profiles for three different thermal diffusivity values (low, medium and high).

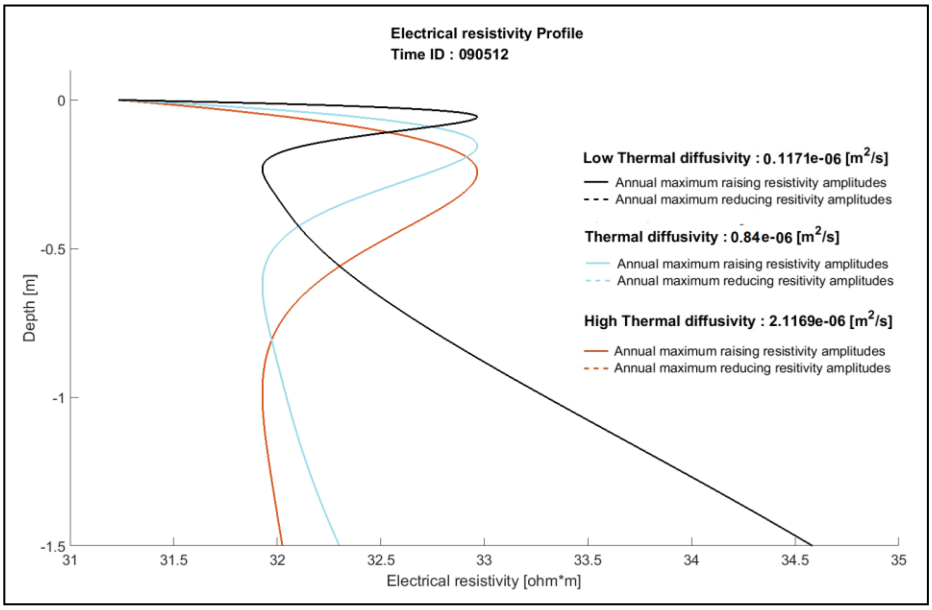

Figure 5-23 Diurnal resistivity profiles due to the surface temperature oscillation for three different thermal diffusivity values (low, medium and high).

A set of seven forward homogeneous models, with the medium thermal diffusivity value (clay formation) were calculated in order to examine the efficiency of the method to detect and correct the temperature effect. A dipole-dipole array ERT data set was considered with 48 electrodes and 0.05 m spacing, for both annual and diurnal cycles.

Figure 5-24 presents the temperature profiles for one day of each season. For January 9, three extra temperature profiles represent the changes during a 24 hour period. Figure 5-25 shows the corresponding resistivity profiles that were used for the forward models. From Figure 5-26 to Figure 5-30, the results of the forward models and their corrections, starting from month April, continues to July, then to September and to January, are examined. For January, Figure 5-30 shows the inversions and corrections of the 4 ERT sections obtained every 6 hours of a diurnal cycle, where all the corrections converge to a single resistivity value for each depth. The rms error between the forward and the temperature corrected inversion results is close to 5 %.

As a result the ERT method is highly sensitive to the diurnal temperature oscillation when the inter electrode spacing is small (< 0.1 m). The correction with a well established temperature profile can be implemented, but the artefacts from the inversion's noise need to be taken into account during the interpretation process.

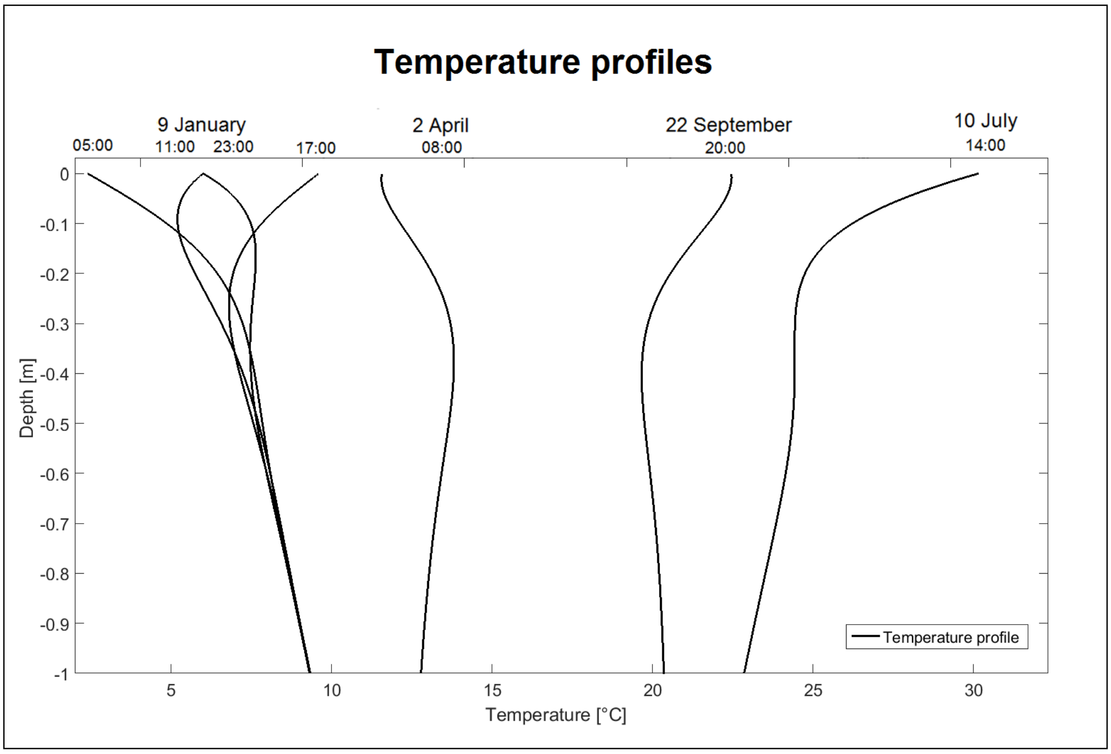

Figure 5-24 Temperature profiles for the seven tested dates.

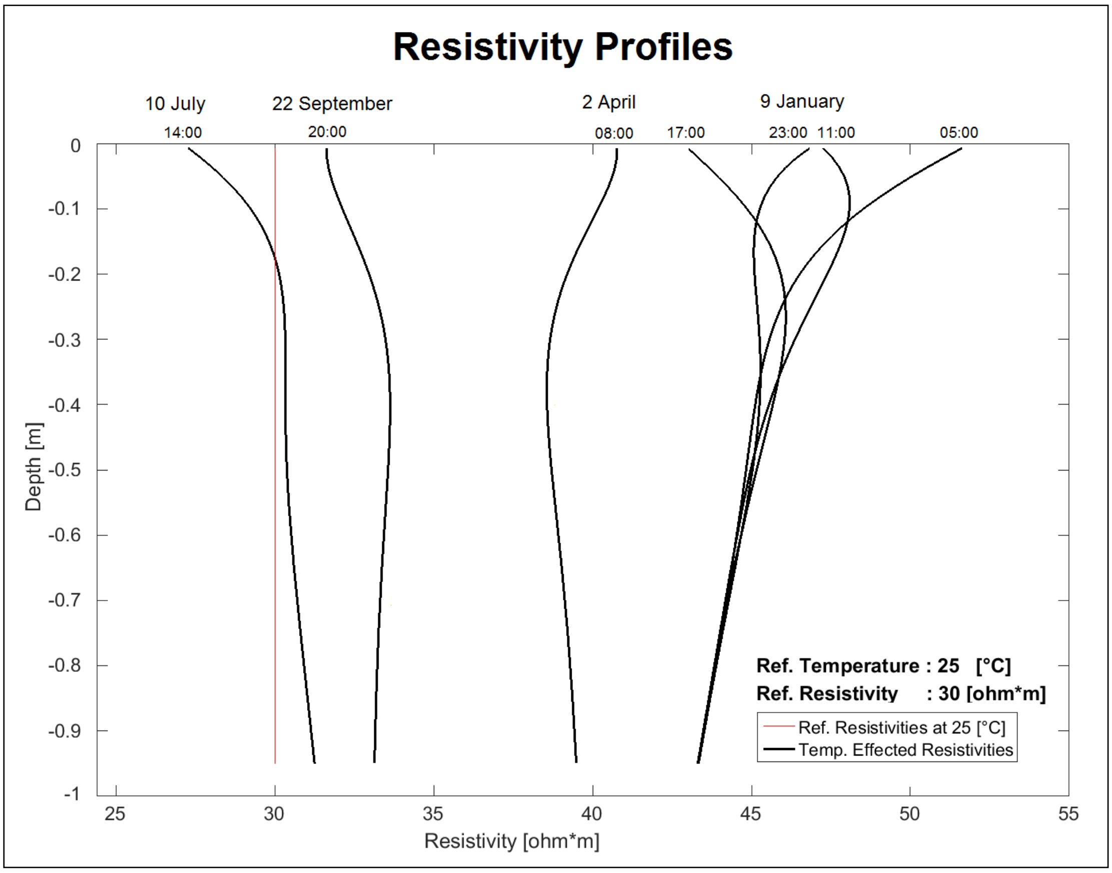

Figure 5-25 Resistivity profiles for the seven tested dates.

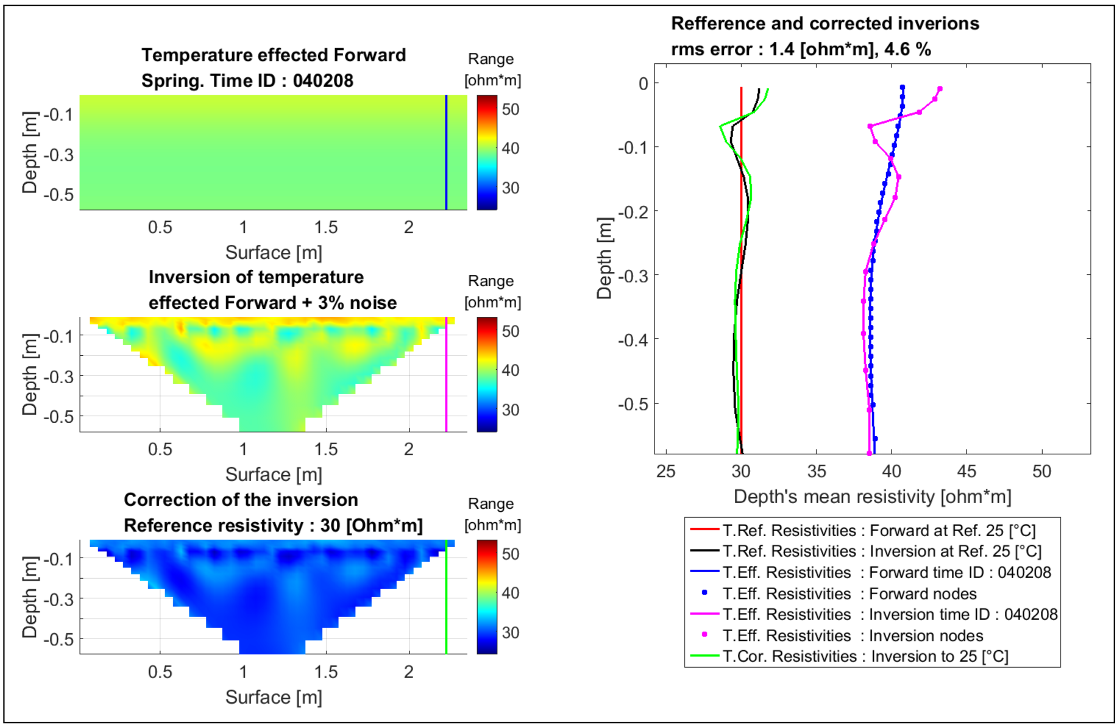

Figure 5-26 Correction of the inversion results for the data collected at April.

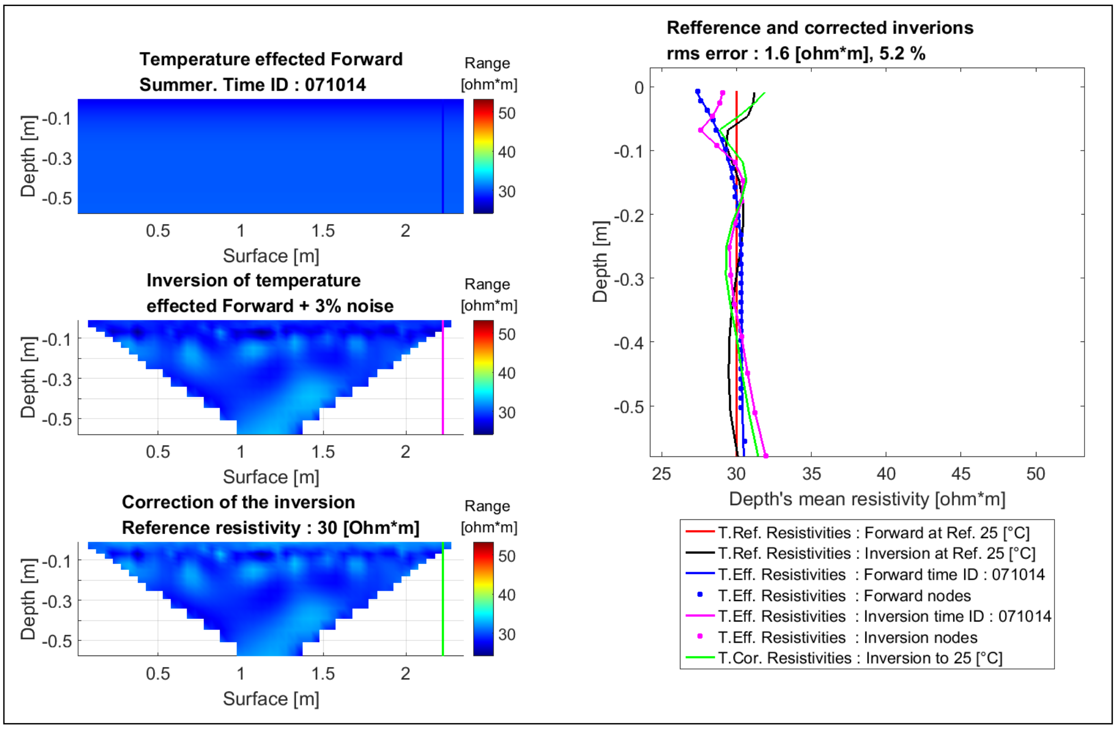

Figure 5-27 Correction of the inversion results for the data collected at June.

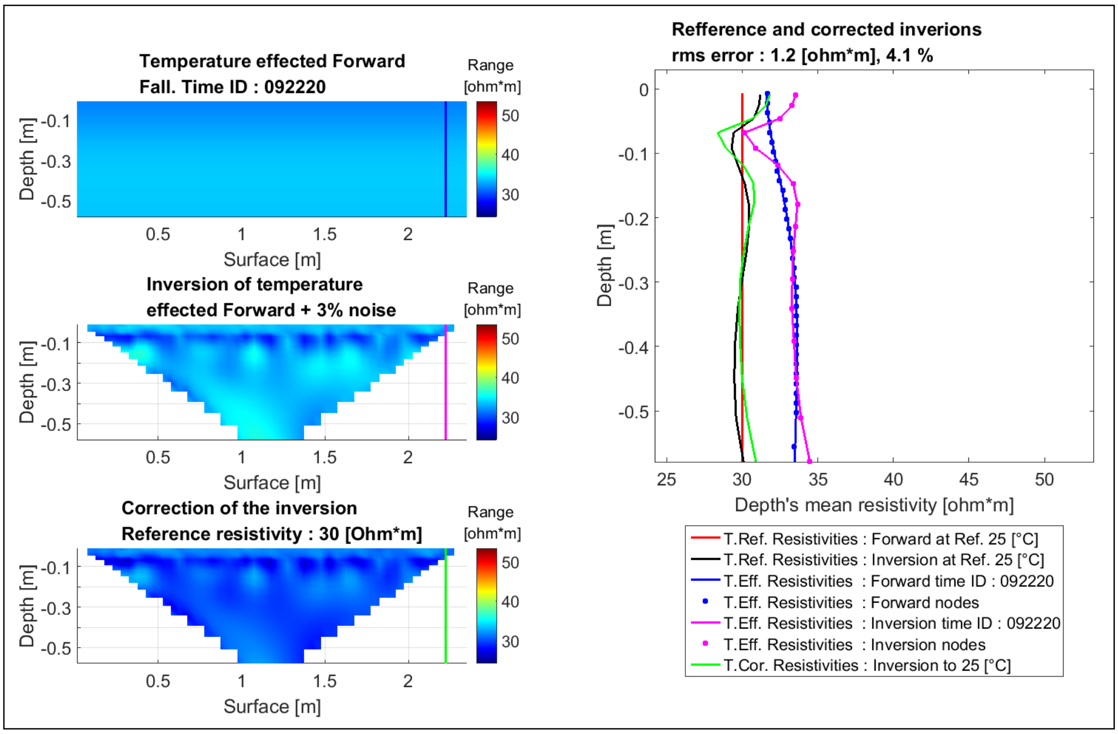

Figure 5-28 Correction of the inversion results for the data collected at September.

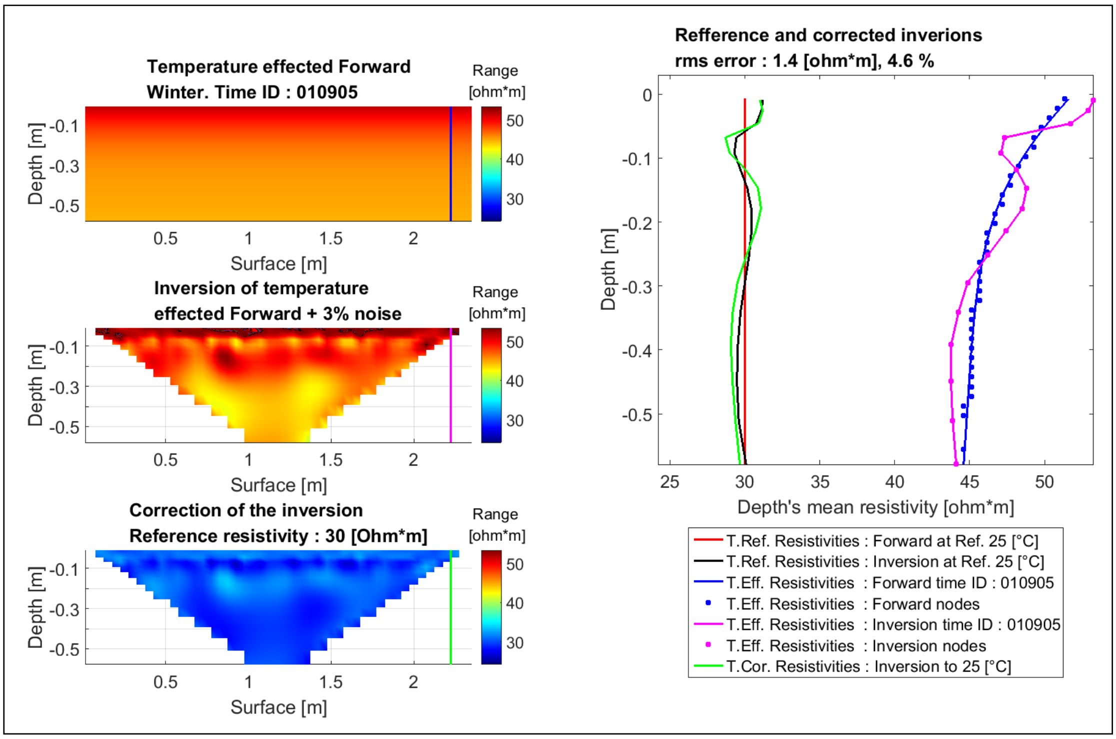

Figure 5-29 Correction of the inversion results for the data collected at January.

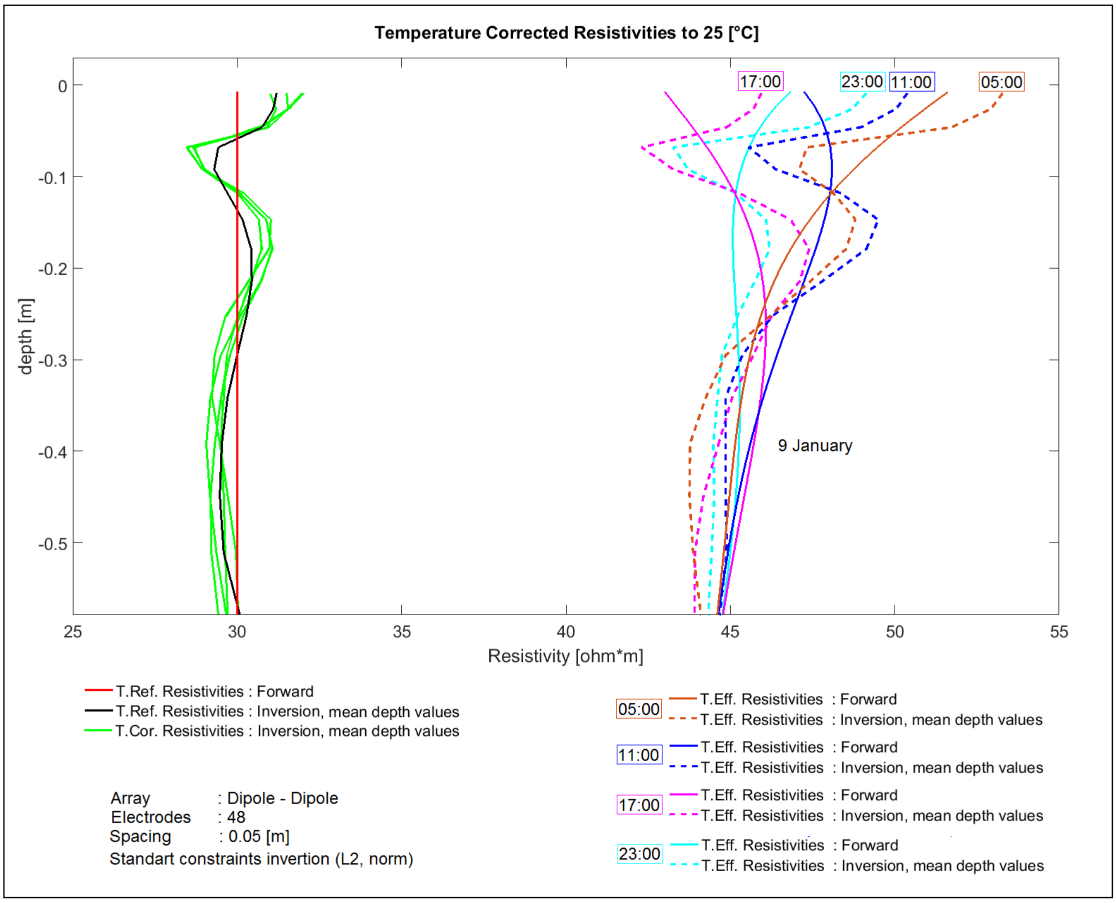

Figure 5-30 Correction of 4 ERT time lapse sections collected during January 9.

5.5 Thermal diffusivity contrast

Wide thermal diffusivity contrast

In order to evaluate the validity of the correction for non thermally homogeneous media i.e. media which consist of materials with different thermal diffusivities, a set of two layered forward models, with two values of thermal diffusivity, was calculated and corrected using the analytical solution for a single thermal diffusivity value. Note that temperature variation profile in this case was calculated using the COMSOL package.

In Table 5-1 a low thermal diffusivity “dry China clay” (yellow colour) and a high “Dark grey clayey fine sand silt 28% water content” (green colour) with values of 0.22 and 1.69 * 10^{-6} m^2/s respectively, were used to simulate the heat transition of two models (Figure 5-31). In the first model, the low diffusivity layer overlays the high diffusivity layer and in the second model, the layers are placed with opposite arrangement. For both models the thickness of the first layer is 1.5 m.

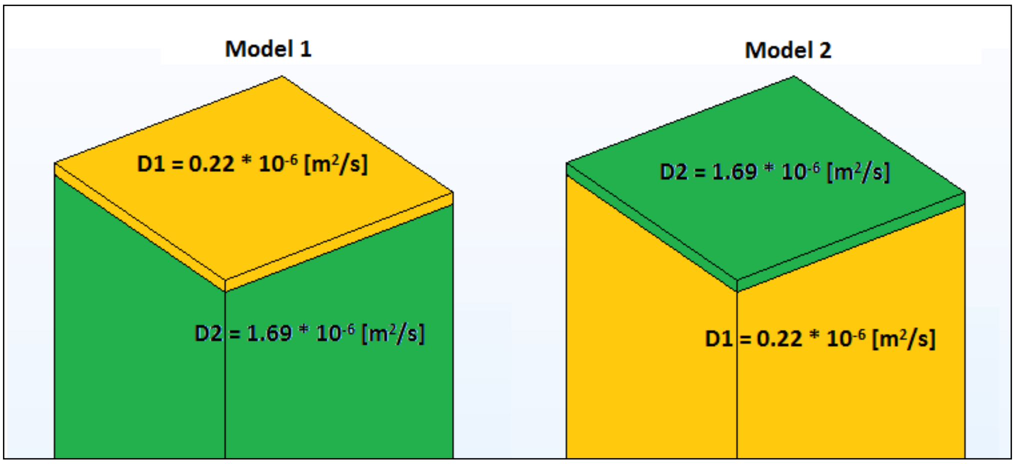

Figure 5-31 High diffusivity contrast models used for the layered forward modeling.

Figure 5-32 presents the temperature profiles from the numerical simulations of the above models, as well as the analytical solutions that are based on the thermal diffusivities of each one of the soil layers as well as an average value of 0.84* 10^{-6} m^2/s, for the correction. In case of the model 1, the low amplitude of temperature at the depth of 1.5 m damps very fast inside the second layer that has higher diffusivity. In the case of mode 2, the low diffusivity of the second layer acts as a barrier for the heat transition and the result is an accumulation of energy gain or loss (from summer or winter) inside the first 1.5 m.

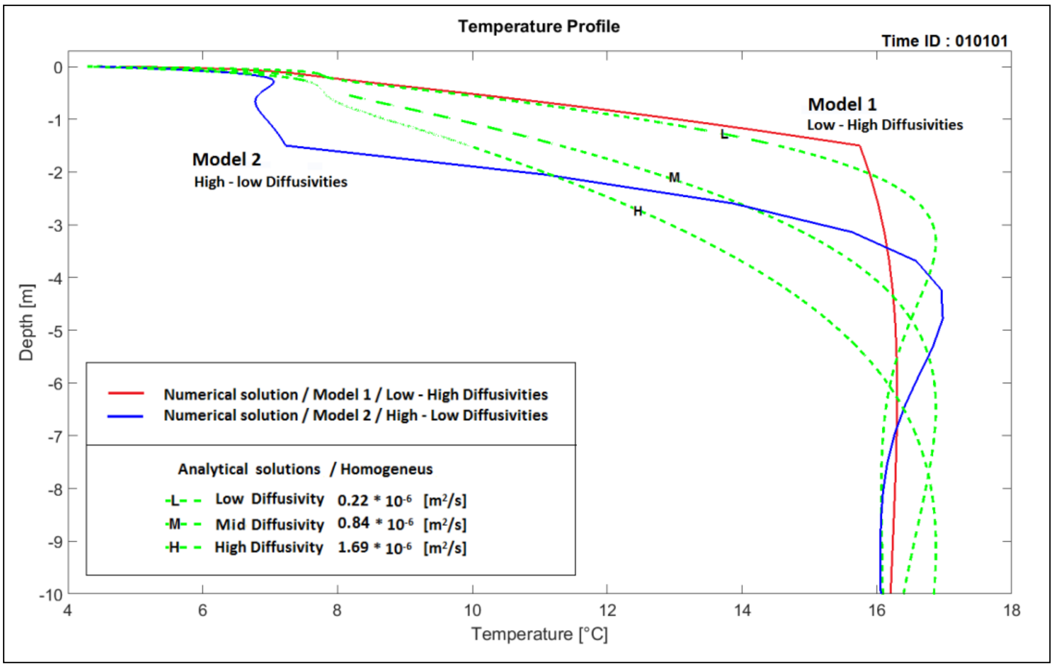

Figure 5-32 Temperature profiles (green lines) used to correct model 1 (red line) and 2 (blue line).

The analytical temperatures profiles of Figure 5-32 with green colour were used to correct the inversion results of both model 1 and model 2. Figure 5-33, presents the model 1 for the three cases of correction with low, high and mid thermal diffusivity. For this model, when the low thermal diffusivity of the upper layer was used for the correction, the RMS error was the smallest.

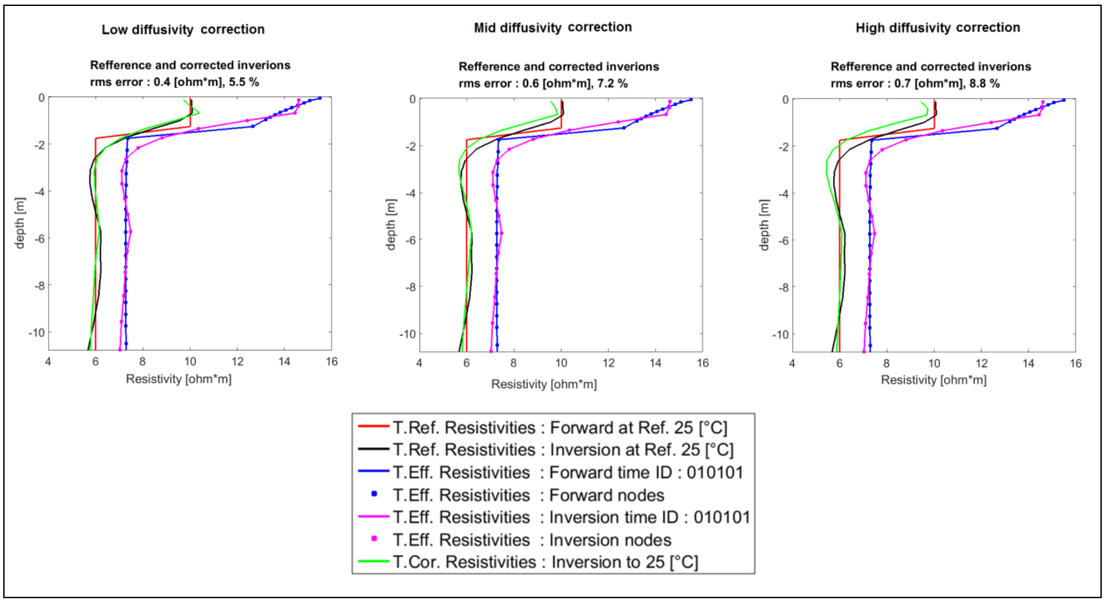

Figure 5-33 Correction of the resistivity profile for the Model 1 (Fig. 5-31) after applying different homogeneous diffusivity correction models.

Figure 5-34 presents the results of the second model where the high thermal diffusivity medium ovelay the low one. For this case, again using the top-layer's thermal diffusivity (high thermal diffusivity this time) for correcting the resitivities produces the smallest RMS error. As a result it is preferable to use the thermla porperties of the upper layer for the calculation of the temperature profile.

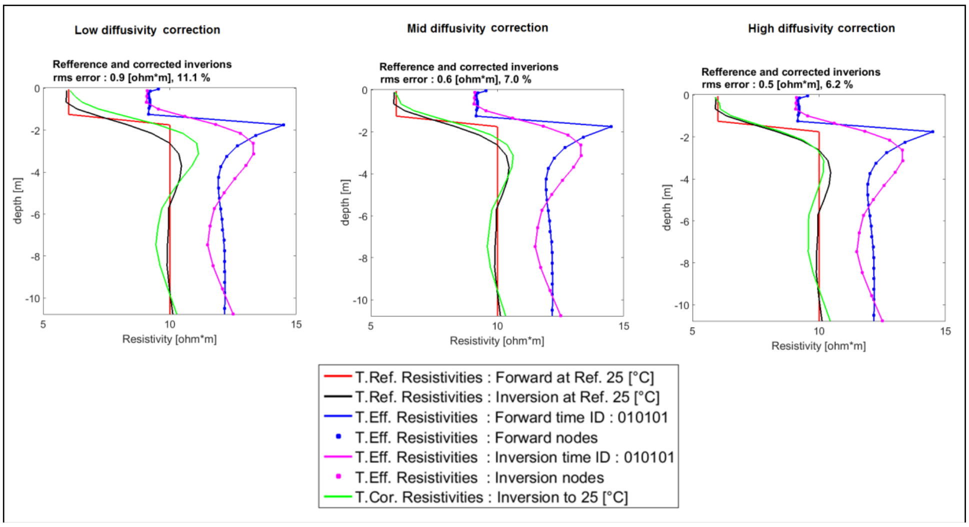

Figure 5-34 Correction of the resistivity profile for the Model 2 (Fig. 5-31) after applying different homogeneous diffusivity correction models.

Narrow thermal diffusivity contrast

A special model was created in order to examine the correction results for a narrow thermal diffusivity contrast (0.54 – 1.04 m^2/s). Figure 5-35 left, shows the 2D geometry of the forward reference resistivity model at 25 °C. The numerical result of the 2D temperature distribution (calculated with Comsol) is shown in Figure 5-35 (middle) while in Figure 5-35 (right) the temperature effected 2D geoelectrical distribution is shown, indicating the variation inflicted to the initial resistivity model due to the temperature variations.

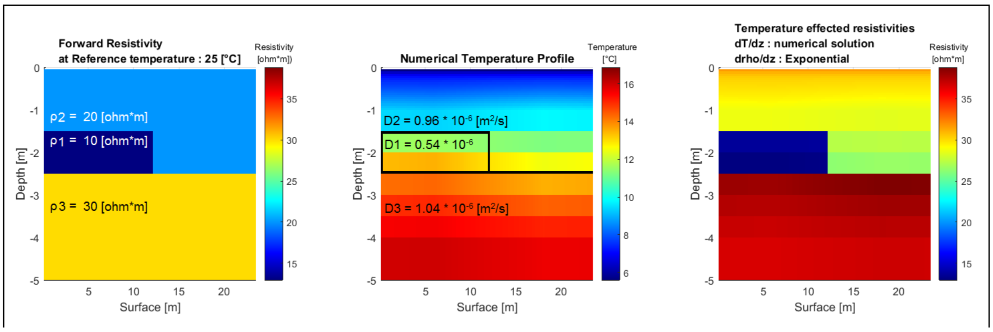

Figure 5-35 (left) the 2D geometry of the resistivity model, (middle) the numerical result of the 2-D temperature distribution for the model, (right) the temperature effected 2D geoelectrical distribution.

Figure 5-36 and Figure 5-37 present the reference and temperature effected forward models with their inversions, as well as the correction results. For the correction, a mean value of thermal diffusivity was used equal to 0.84 * 10^{-6} m^2/s. As a result when the thermal diffusivity range is small a mean value of thermal diffusivity can be used.

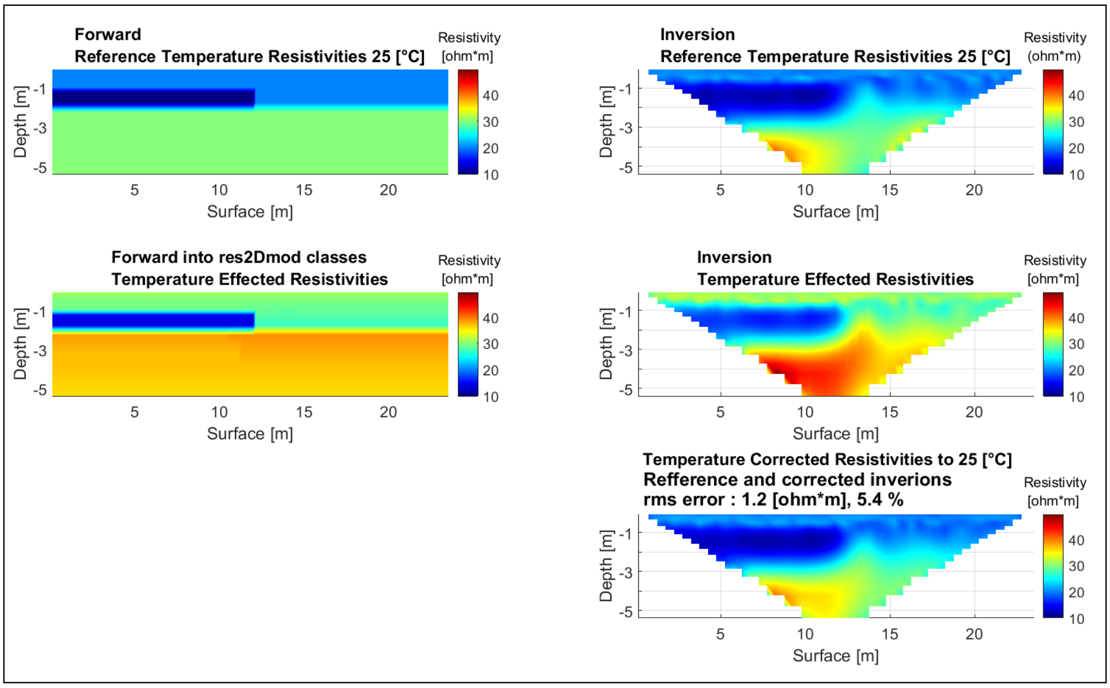

Figure 5-36 Left panel: reference and the temperature effected models. Right panel: inverted models of the synthetic data for the model with and without the temperature effect and bottom right is the inversion model after “temperature correction”.

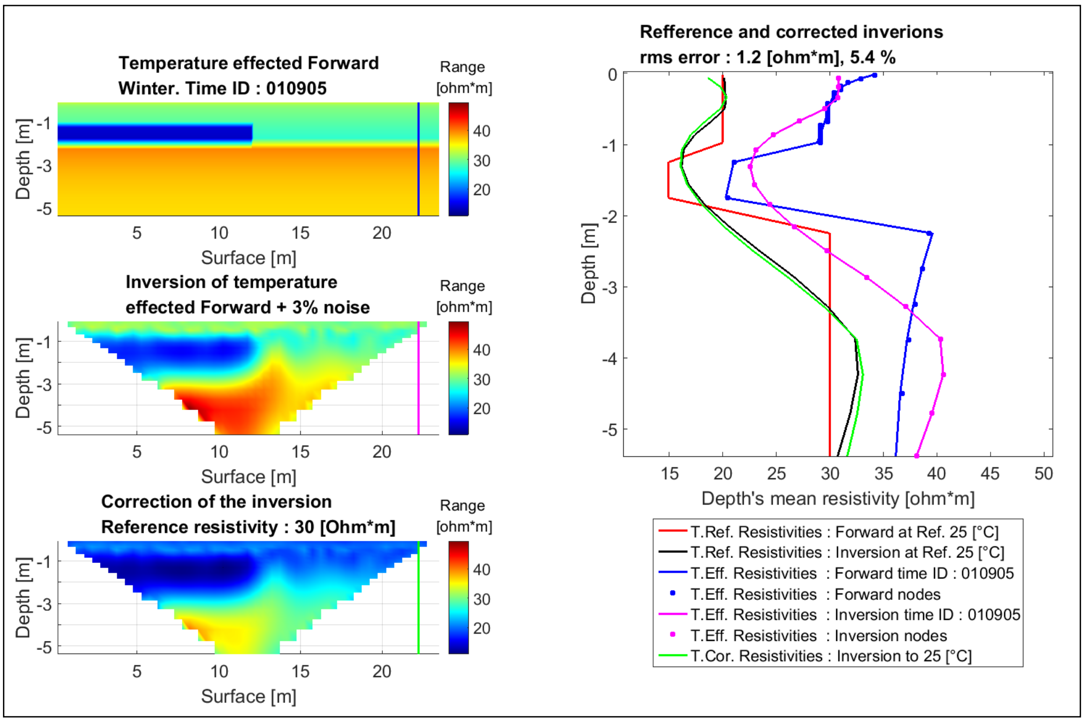

Figure 5-37 Correction of the inversion results for the narrow thermal diffusivity contrast, complex model of figure 5-35.

5.6 Electrical resistivity contrast

In order to evaluate the correction in cases that electrical resistivity contrast is large, a vertical discontinuity model of a limestone with sand and clay soils was created. The upper layer with thickness 0.5 m consists of fine sand with 24.6 % water content, thermal diffusivity D1 = $1.044 * 10^{-6}$ m^2/s and electrical resistivity ρ1 = 20 ohm-m. The second soil layer consist of china clay with 46.2 % water content, thermal diffusivity D2 = $0.544 * 10^{-6}$ m^2/s and electrical resistivity ρ2 = 10 ohm-m. The limestone that "occupies" the rest of the model has thermal diffusivity D3 = $0.878 * 10^{-6}$ m^2/s and electrical resistivity ρ3 = 1000 ohm-m. Figure 5-38 left, presents the geometry of the model with the resistivity values at a reference temperature of 25 °C , and at the right we present the respective temperature distribution model resulted from the numerical simulation with the Comsol multiphysics software, for the 1st hour of the 3rd year.

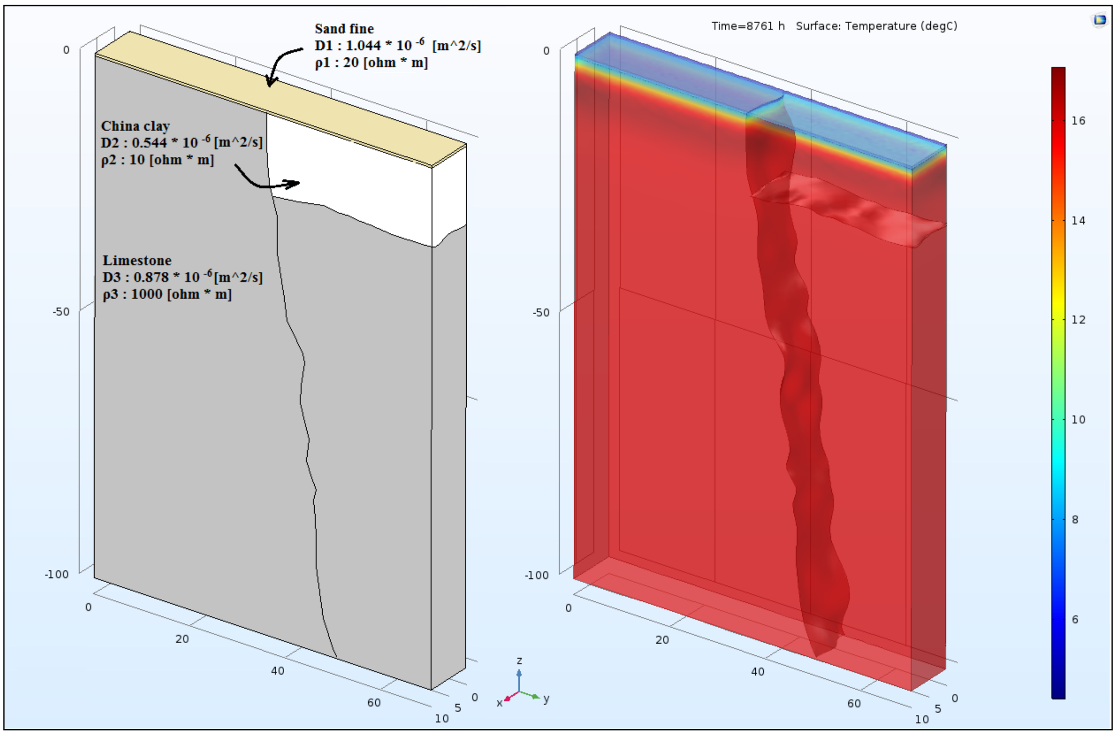

Figure 5-38 High electrical resistivity contrast model at reference temperature (left) and the numerical distribution of temperature (right).

Figure 5-39 presents the temperature effect imposed to the resistivities of the formation, where only 3 electrical resistivity classes were used to describe the resistivity profile of the sand and clay part of the geometry, as the majority of the classes were bound by the wider range that has the 1000 ohm-m reference limestone under the influence of the same temperature effect.

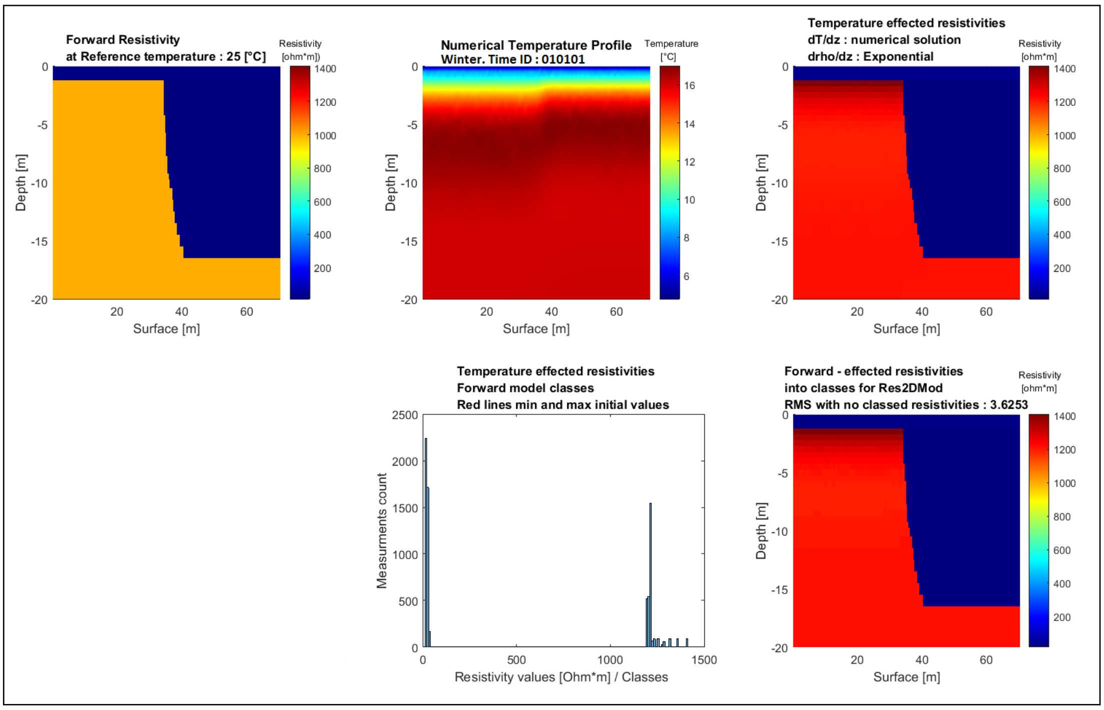

Figure 5-39 Forward modeling of vertical discontinuity model under the influence of the surface temperature effect.

Figure 5-40 shows the inversion results (robust data constraints - L1 norm) of the reference model at 25 °C and the effected model, at the first day of the year. Downright side of this figure show the tomographic result after temperature correction.

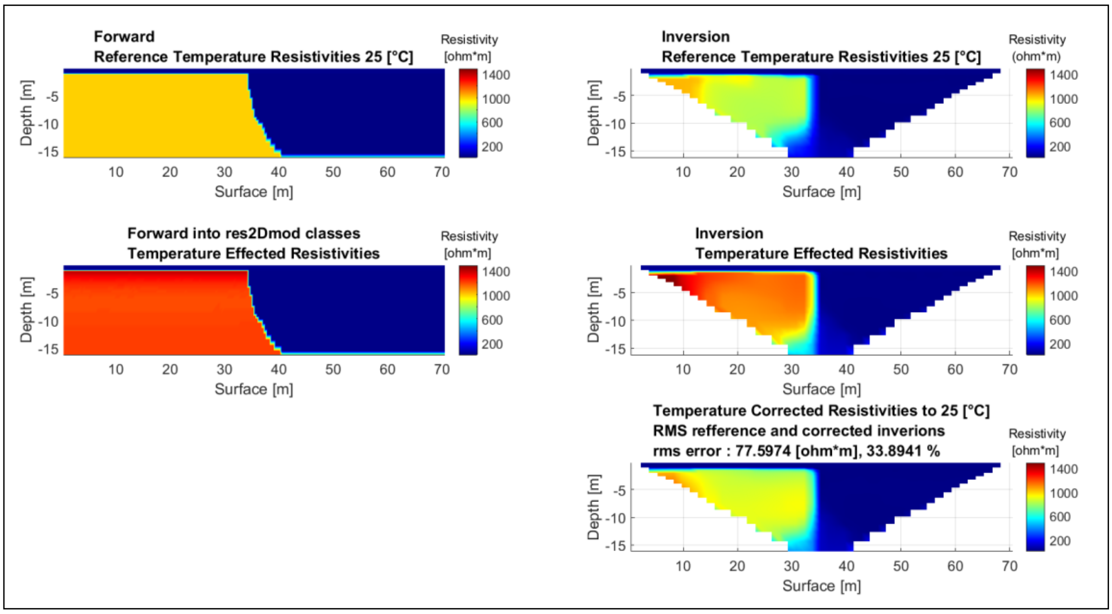

Figure 5-40 Left panel: reference and the temperature effected models. Right panel: inverted models of the synthetic data for the model with and without the temperature effect and bottom right is the inversion model after "temperature correction".

Figure 5-41 presents the validation panel for the case of high resistivity contrast, were the correction made with the use of the thermal diffusivity of the top layer "sand fine". The RMS of the corrected tomography with the inversion of the reference model is 33.9%. If the inversion had been conducted with standard constraints, the RMS error would be reduced to 26.2%.

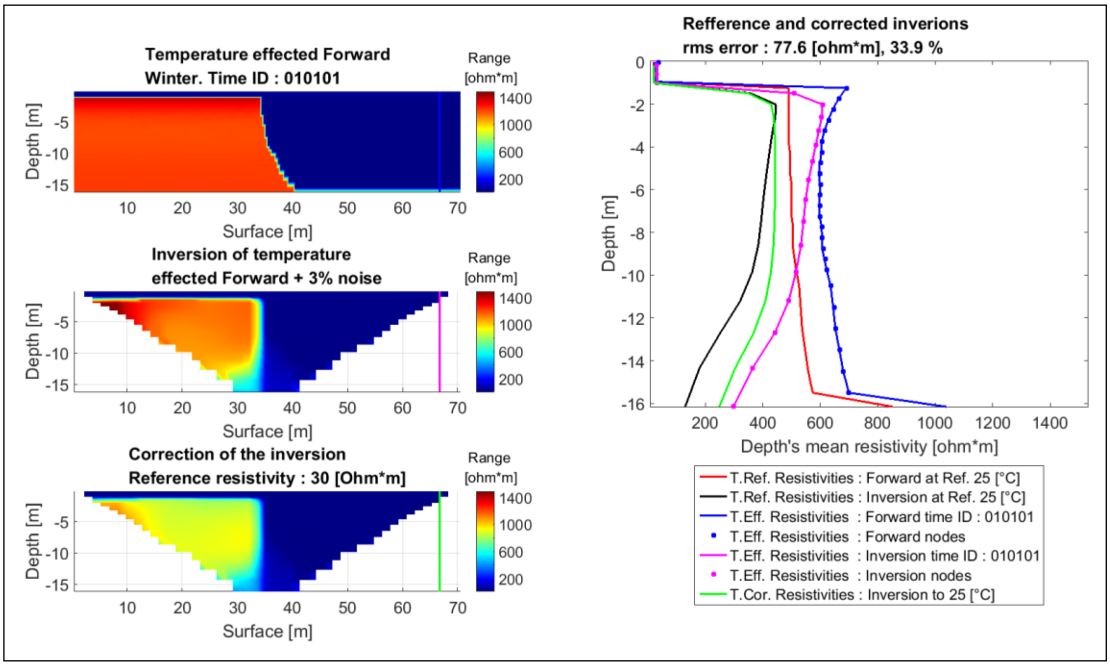

Figure 5-41 Correction of vertical discontinuity model.

When the "china clay" thermal diffusivity was used for the correction, the rms error became 35.3%, and for the correction with the limestone's thermal diffusivity the rms error became 36.5%. As a result the temperature correction of the high electrical resistivity contrast formations need to be further investigated.

6. Conclusions

For a homogeneous earth and traveling from the centre to the surface, we can assume epicentral electrical resistivity horizons that are formed due to the temperature gradient created by the deference of the surface and the earth's interior temperatures. The close to surface electrical resistivity horizons that are effected from the surface temperature oscillation, can be divided into diurnal and seasonal oscillating resistivity horizons and can be grouped into the surface temperature effected layer. High resolution electrical resistivity tomographies (ERT) will detect the temperature changes inside the surface temperature effected layer and as a result, they can be corrected (converted) to a selected reference temperature.

The temperature correction approach for the surface temperature effected ERTs, is based on the calculation of the subsurface temperature profile with the use of the bulk heat properties of the surveyed formation, the history of three annual surface temperature oscillation events (1^{st} the mean seasonal temperature oscillation, 2^{nd} the mean diurnal temperature oscillation and 3^{rd} the seasonal variation of the mean diurnal temperature amplitude) as well as the actual diurnal temperature amplitude of the ERT survey day. The inversion results were corrected with the use of the calculated subsurface temperature profile (based on the inversion result's depths) and a "temperature - electrical resistivity" conversion model.

The conclusions are based on the literature review as well as on forward and inverse, homogenous and inhomogeneous models that focus on the seasonal and the diurnal oscillating resistivity horizons of the subsurface. The surface temperature oscillation was determined by a Mediterranean climate. At the depth where the electrical resistivity horizons are surface-temperature-uneffected, the temperature is equal to the mean annual surface temperature. The conclusions have been presented in every individual chapter in this work and are summarized below.

- "Temperature - electrical resistivity" conversion models: From literature review, it seems that we need to use conversion models, depending on the different degree of saturation. Typically, in the case of close to water saturated porous formations, we should use either the exponential model (Sheets & Hendrickx

1995; Corwin & Lesch 2005) or the ratio model (Keller and Frischknecht, 1966) with temperature coefficient of resistance δ=0.00191 °C^{-1} as it is suggested by Ma et al. (2011). For non saturated porous formations (dry and vadose zone) the ratio model with δ=0.0025 °C^{-1} seems to work fine in the range of 5-20 °C and should be tested for the rest annual surface temperature range, in comparison to the power function conversion model of Besson et al. (2008).

- Perturbation depth of the diurnal surface temperature oscillation: In view of the diurnal perturbation depth, the maximum depths of indicative diurnal oscillating electrical resistivity horizons, with oscillation amplitudes equal to 1%, 3 % and 5 % of the mean diurnal electrical resistivity of each depth, are presented in Table 6-1. Even in the case of high diffusivity materials, the diurnal oscillating electrical resistivity horizon that oscillates with 3 % amplitude, cannot be found deeper than 0.33 m.

Oscillation amplitudes Ohm-m	Low diffusivity medium $0.12 * 10^{-6}$ m^2/s (e.g. fine sand dry)		High diffusivity medium $2.12 * 10^{-6}$ m^2/s (e.g. slightly silty sandy GRAVEL)	
	Winter day	Summer day	Winter day	Summer day
5 %	0.04 m	0.04 m	0.16 m	0.20 m
3 %	0.07 m	0.08 m	0.28 m	0.33 m
1 %	0.13 m	0.14 m	0.55 m	0.60 m

Table 6-1 Maximum depths of indicative diurnal oscillating resistivity horizons

- Correction of diurnal oscillating resistivity horizons: In cases interested in the diurnal temperature oscillation and the corresponding depths, with extremely small ERT inter electrode spacings (e.g. <0.1m), and when there is no direct measured temperature data, the proposed correction method could be tested/used for the approximation of the temperature profile and the correction of the ERT.

- Perturbation depth of the seasonal surface temperature oscillation: Higher values of thermal diffusivity increase the perturbation depth of the surface temperature effect. For some typical rock formations we have calculated the maximum depths of indicative seasonal oscillating resistivity horizons with oscillation amplitudes equal to 1%, 3 % and 5 % of the electrical resistivity at the mean annual temperature (Table 6-2). Even in the case of high diffusivity materials the 3% change resistivity horizon cannot be found deeper than 9.5 m.

Oscillation amplitudes Ohm-m	Low diffusivity medium $0.12 * 10^{-6}$ m^2/s (e.g. fine sand dry)	Mid diffusivity medium $0.84 * 10^{-6}$ m^2/s (e.g. clay)	High diffusivity medium $2.12 * 10^{-6}$ m^2/s (e.g. slightly silty sandy GRAVEL)
5 %	1.5 m	4.5 m	7 m
3 %	2 m	6 m	9.5 m
1 %	3.5 m	9 m	14.7 m

Table 6-2 Maximum depths of indicative seasonal oscillating resistivity horizons

- Electrode array spacing and temperature correction: The electrical resistivity tomography measurements obtained with basic inter-electrode spacing equal or larger than 10 m, are practically insensitive to the surface temperature effect so, in theory, there is no need to apply temperature correction. In practice, by applying the temperature correction in such electrode separations we will generate significant inversion artifacts on the surface layer, as the resolution of the inversion parameter is not compatible with the higher resolution of the temperature change. Therefore such a correction should be avoided.

- Electrode array spacing and temperature correction: For array inter-electrode spacing of below 10 m, the inversion results are generally influenced by the temperature effect so temperature correction needs to be considered for array inter-electrode spacing of below 5 m, the inversion results are highly influenced. As the ERT measurement spacing decreases the inversion process is becoming increasingly sensitive to the temperature effect and accurate calculation of the correction temperature profile is becoming an important issue.

- Correction of seasonal oscillating resistivity horizons: For the calculation of the subsurface temperature profile and the correction of the seasonal oscillating resistivity horizons of the ERT, we should utilize correction temperature profiles which take into account both the annual and the diurnal oscillation events (1st and

2^{nd} oscillation events). The additional consideration of a 3^{rd} oscillation event (seasonal variation of diurnal's temperature amplitude) to the calculation of subsurface temperature correction profile is also necessary to be considered as it offers an increased accuracy into the overall correction.

- Thermal diffusivity inhomogeneous formations: For the correction of layered models with relatively limited thermal diffusivity contrast (e.g. 0.54 – 1.04 m^2/s), the use of a mean thermal diffusivity value can be applied for the calculation of the temperature profile. In cases of high diffusivity contrast (e.g.. 0.22 and 1.69 * 10^{-6} m^2/s) it is preferable to consider an estimate of thermal diffusivity based on the value of the top layer thermal diffusivity, for the correction of subsurface temperature profile.

- Electrical resistivity inhomogeneous formations: For cases of surveyed subsurfaces that consist of geological formations with high electrical resistivity contrast (e.g. 30 and 1000 ohm-m reference values at reference temperature of 25 °C), the correction method has to be further investigated as the correction's rms error is large.

7. Bibliography

Abu-Hamdeh, N. H. (2003). Thermal properties of soils as affected by density and water content. Biosystems Engineering, 86(1), 97–102. https://doi.org/10.1016/S1537-5110(03)00112-0

Allison L Bernstein C A Bower J W Brown M Fireman J T Hatcher H E Hayward G A Pearson R C Reeve, L. E., & Richards Wilcox L A Richards, A. L. (1954). Diagnosis and Improvement of United States Salinity Laboratory Staff. Retrieved from https://www.ars.usda.gov/ARSUserFiles/20360500/hb60_pdf/hb60complete.pdf

Bayowa, O. G., & Olayiwola, N. S. (2015). Electrical Resistivity Investigation for Topsoil Thickness, Competence and Corrosivity Evaluation: A Case Study from Ladoke Akintola. https://doi.org/10.7763/IPCBEE

Brillante, L., Mathieu, O., Bois, B., Van Leeuwen, C., & Lévêque, J. (2015). The use of soil electrical resistivity to monitor plant and soil water relationships in vineyards. Retrieved from https://www.soil-discuss.net/1/C547/2015/soild-1-C547-2015-supplement.pdf

Brunet, P., Clément, R., & Bouvier, C. (2010). Monitoring soil water content and deficit using Electrical Resistivity Tomography (ERT) - A case study in the Cevennes area, France. Journal of Hydrology, 380(1–2), 146–153. https://doi.org/10.1016/j.jhydrol.2009.10.032

Chambers, J. E. (2009). C18 Hydrogeophysical Monitoring of Landslide Processes Using Automated Time-Lapse Electrical Resistivity Tomography (ALERT). Retrieved from http://nora.nerc.ac.uk/id/eprint/9318/1/Hydrogeophys.pdf

Chambers, J. E., Gunn, D. A., Wilkinson, P. B., Meldrum, P. I., Haslam, E., Holyoake, S., … Wragg, J. (2014). 4D electrical resistivity tomography monitoring of soil moisture dynamics in an operational railway embankment. Near Surface Geophysics, 12(1), 61–72. https://doi.org/10.3997/1873-0604.2013002

COMSOL Multiphysics®. (n.d.). COMSOL Multiphysics® v. 5.2. www.comsol.com. COMSOL AB, Stockholm, Sweden.

Comsol: Postprocessing and Visualization : Car Windshield Antenna Effect on a Cable Harness (Car geometry used for the cover page figure) https://www.comsol.com/release/5.3/postprocessing-visualization

Corwin, D. L., & Lesch, S. M. (2005). Apparent soil electrical conductivity measurements in agriculture. Computers and Electronics in Agriculture, 46, 11–43. https://doi.org/10.1016/j.compag.2004.10.005

Kim J.H. (2017). Dc2Dpro, User's manual, Geoelectric Imaging Laboratory, KIGAM, Korea.

De Vries, D. A. (1975a). "The Thermal Conductivity of Soil." Med. Landbouwhogeschool, Wageningen, Netherlands

Eindhoven University of Technology. (2009). Periodic soil temperature fluctuations.

Eindhoven University of Technology, 1–18. Retrieved from http://archbps1.campus.tue.nl/bpswiki/images/6/6a/H3.pdf

Firmbach, L., Giordano, N., Mandrone, G., Comina, C., Mandrone, G., Kolditz, O., … Dietrich, P. (2013). Experimental heat flow propagation within porous media using electrical resistivity tomography (ERT) Landslide investigation and mitigation View project EGC 2013 Experimental heat flow propagation within porous media using electrical resistivity tomograph. Retrieved from https://www.researchgate.net/publication/257840826

Fu, X., & Leventhal, B. (2011). Understanding the impact of boundary and initial condition errors on the solution to a thermal diffusivity inverse problem, 156–174.

Gance, J., Malet, J.-P., Supper, R., Sailhac, P., Ottowitz, D., & Jochum, B. (2016). Permanent electrical resistivity measurements for monitoring water circulation in clayey landslides. Journal of Applied Geophysics, 126, 98–115. https://doi.org/10.1016/j.jappgeo.2016.01.011

Genelle, F., Sirieix, C., Riss, J., & Naudet, V. (2012). Monitoring land fi ll cover by electrical resistivity tomography on an experimental site. Engineering Geology, 145–146, 18–29. https://doi.org/10.1016/j.enggeo.2012.06.002

Gunn, D. A., Chambers, J. E., Uhlemann, S., Wilkinson, P. B., Meldrum, P. I., Dijkstra, T. A., … Glendinning, S. (2015). Moisture monitoring in clay embankments using electrical resistivity tomography. Construction and Building Materials, 92, 82–94. https://doi.org/10.1016/J.CONBUILDMAT.2014.06.007

Hamdhan, I. N., & Clarke, B. G. (2010). Determination of Thermal Conductivity of Coarse and Fine Sand Soils. Proceedings World Geothermal Congress. Retrieved from https://www.geothermal-energy.org/pdf/IGAstandard/WGC/2010/2952.pdf

Hayley, K., Bentley, L. R., & Gharibi, M. (2009). Time-lapse electrical resistivity monitoring of salt-affected soil and groundwater. Water Resources Research, 45(7). https://doi.org/10.1029/2008WR007616

Hayley, K., Bentley, L. R., Gharibi, M., & Nightingale, M. (2007). Low temperature dependence of electrical resistivity: Implications for near surface geophysical monitoring. Geophysical Research Letters, 34(18), 1–5. https://doi.org/10.1029/2007GL031124

Hayley, K., Bentley, L. R., & Pidlisecky, A. (2010). Compensating for temperature variations in time-lapse electrical resistivity difference imaging. GEOPHYSICS, 75(4), WA51-WA59. https://doi.org/10.1190/1.3478208

Hermans, T., Nguyen, F., Robert, T., & Revil, A. (2014). Geophysical methods for monitoring temperature changes in shallow low enthalpy geothermal systems. Energies, 7(8), 5083–5118. https://doi.org/10.3390/en7085083

Hillel, D. (2004). Introduction to environmental soil physics. Elsevier Academic Press.

Holden, P. A., & Fierer, N. (2003). Microbial Ecology, 216–224.

Jin, M., Mullens, T., Jin, M. S., & Mullens, T. (2014). A Study of the Relations between Soil Moisture, Soil Temperatures and Surface Temperatures Using ARM Observations and Offline CLM4 Simulations. Climate, 2(4), 279–295. https://doi.org/10.3390/cli2040279

Keller GV. Frischknecht FC. Electrical methods in geophysical prospecting. Pergamon Press Inc., Oxford; 1996.

Krautblatter, M., & Hauck, C. (2007). Electrical resistivity tomography monitoring of permafrost in solid rock walls. Journal of Geophysical Research: Earth Surface, 112(2), 1–14. https://doi.org/10.1029/2006JF000546

Kummerow, J., & Raab, S. (2015a). Temperature Dependence of Electrical Resistivity - Part I: Experimental Investigations of Hydrothermal Fluids, 1876–6102. https://doi.org/10.1016/j.egypro.2015.07.854

Kummerow, J., & Raab, S. (2015b). Temperature Dependence of Electrical Resistivity - Part II: A New Experimental Set-up to Study Fluid-saturated Rocks. Energy Procedia, 76, 247–255. https://doi.org/10.1016/j.egypro.2015.07.855

Kusuda, T., & Achenbach, P. R. (1965). Summary of Research Report 8972: Earth Temperature and Thermal Diffusivity at Selected Stations in the United States. https://doi.org/10.6028/NBS.RPT.8972

Lewis, G. M., & Dethier, D. P. (2013). USING GEOPHYSICAL TECHNIQUES IN THE CRITICAL ZONE TO DETERMINE THE PRESENCE OF PERMAFROST. Retrieved from http://czo.colorado.edu/pub/2013/keck/G.Lewis_thesis_2013.pdf

Ma, R., McBratney, A., Whelan, B., Minasny, B., & Short, M. (2011). Comparing temperature correction models for soil electrical conductivity measurement. Precision Agriculture, 12(1), 55–66. https://doi.org/10.1007/s11119-009-9156-7

Martin, A. I. (2004). Hydrate Bearing Sediments - Thermal Conductivity Hydrate Bearing Sediments- Thermal Conductivity.

Matias, M., & Almeida, F. (2017). ERT and the Location of Mining Cavities in Anisotropic Media: A Field Example. In Cave Investigation. InTech. https://doi.org/10.5772/intechopen.68475

Merrill, M. W. (2018). Marriner W . Merrill journals , 1889-1906 A Register of the Collection, 107, 2017–2019.

Merritt, A. J., Chambers, J. E., Murphy, W., Wilkinson, P. B., West, L. J., Uhlemann, S., … Gunn, D. (2018). Landslide activation behaviour illuminated by electrical resistance monitoring. Earth Surface Processes and Landforms, 43(6), 1321–1334. https://doi.org/10.1002/esp.4316

Michot, D., Benderitter, Y., Dorigny, A., Nicoullaud, B., King, D., & Tabbagh, A. (2003). Spatial and temporal monitoring of soil water content with an irrigated corn crop cover using surface electrical resistivity tomography. Water Resources Research, 39(5), 1–20. https://doi.org/10.1029/2002WR001581

Muchingami, I., Hlatywayo, D. J., Nel, J. M., & Chuma, C. (2012). Electrical resistivity survey for groundwater investigations and shallow subsurface evaluation of the basaltic-greenstone formation of the urban Bulawayo aquifer. Physics and Chemistry of the Earth, 50–52, 44–51. https://doi.org/10.1016/j.pce.2012.08.014

Papazaxos Basilis (1996) Εισαγωγή στη γεωφυσική.

Rhoades, J. D., Chanduvi, F., & Lesch, S. (1999). Soil salinity assessment: Methods and interpretation of electrical conductivity measurements (pp. 1–150). FAO Irrigation and Drainage Paper No. 57. Rome, Italy: Food and Agriculture

Robertson, E. C. (1988). Thermal Properties of Rocks. US Department of the Interior: Geological Survey, 88–441.

res2Dinv , res2dmod (Loke et al., 2003) Geotomo Software

Sheets, K. R., & Hendrickx, J. M. H. (1995). Noninvasive Soil Water Content Measurement Using Electromagnetic Induction. Water Resources Research, 31(10), 2401–2409. https://doi.org/10.1029/95WR01949

Tian, Z., Lu, Y., Horton, R., & Ren, T. (2016). A simplified de Vries-based model to estimate thermal conductivity of unfrozen and frozen soil. European Journal of Soil Science, 67(5), 564–572. https://doi.org/10.1111/ejss.12366

Wang, J., Zhang, X., & Du, L. (2017a). A laboratory study of the correlation between the thermal conductivity and electrical resistivity of soil. Journal of Applied Geophysics, 145, 12–16. https://doi.org/10.1016/J.JAPPGEO.2017.07.009

Wang, J., Zhang, X., & Du, L. (2017b). A laboratory study of the correlation between the thermal conductivity and electrical resistivity of soil. Journal of Applied Geophysics, 145, 12–16. https://doi.org/10.1016/j.jappgeo.2017.07.009

You, Y., Yu, Q., Pan, X., Wang, X., & Guo, L. (2013). Application of electrical resistivity tomography in investigating depth of permafrost base and permafrost structure in Tibetan Plateau. Cold Regions Science and Technology, 87(March), 19–26. https://doi.org/10.1016/j.coldregions.2012.11.004

Appendix: Units of physical properties used in this work.

Si base units

Abbreviation	Unit name	Unit symbol	Quantity
m	meter	l	Length
Kg	kilogram	m	Mass
K	Kelvin	T	Temperature
s	second	t	Time
A =	ampere	I	Electric current
mol	mole	N	Amount of substance

Derived units

Abbreviation	Unit name	Unit symbol	Quantity
J	Joule	E	Energy
°C	Celsius	Tc	Temperature
Kg/m^3	Kilogram/($meter^3$)	ρ_d	Density (subscript "$_d$" distinguish density ρ_d from electrical resistance ρ.)
J/ (K*mol)	Joule / (Kelvin * mole)	CP	Heat capacity per unit mol, constant pressure
J/ (K*mol)	Joule / (Kelvin * mole)	CV	Heat capacity per unit mol, constant volume
J/ (K*kg)	Joule / (Kelvin * kilogram)	cP	Heat capacity per unit mass (specific heat capacity) constant pressure
J/ (K*kg)	Joule / (Kelvin * kilogram)	cV	Heat capacity per unit mass (specific heat capacity) constant volume
J/ ($K*m^3$)	Joule / (Kelvin * $meter^3$)	VHC	Heat capacity per unit volume (volumetric heat capacity)
W/(K *m)	Watt / (Kelvin * meter)	k	Thermal Conductivity
m^2/s	$Meter^2$ / second	D	Thermal diffusivity
W/m^2	Watt / $meter^2$	qh	Heat flux density
$(N*m^2)/C^2$	$8.9875517873681764 * 10^9$	k_c	Coulomb constant
C = s*A	Coulomb		Electric charge
Ω	Ohm	R	Resistance
Ω*m	Ohm-meter	ρ	Electric resistivity (specific Resistance)
S/m	Siemens / meter	σ	Electric conductivity (specific conductance)
A/m^2	Amber / $meter^2$	J	Current density
N/C	Newton / Coulomb	E_{fs}	Electric field strength
V=J/C	Volts	V	Electric potential